




# An investigation of the ‘10 keV feature’ in the spectra of accretion powered X-ray pulsars with *NuSTAR*

Hemanth Manikantan <sup>1</sup>, <sup>2</sup>★, Biswajit Paul and Vikram Rana <sup>1</sup>

*Astronomy and Astrophysics Department, Raman Research Institute, CV Raman Avenue, Sadashivanagar, Bangalore 560080, India*

Accepted 2023 August 18. Received 2023 August 18; in original form 2023 January 3

## ABSTRACT

Some of the accreting X-ray pulsars are reported to exhibit a peculiar spectral feature at  $\sim 10$  keV, known as the ‘10 keV feature’. The feature has been characterized as either an emission line or an absorption line, and its origin is unknown. It has been found in multiple observations of the same source by different observatories, but not all the observations of any particular source consistently showed the presence of it. In this work, we have carried out a systematic investigation for the presence of the ‘10 keV feature’ using data from *NuSTAR*, a low background spectroscopic observatory having uninterrupted wide band coverage on either side of 10 keV. We performed a systematic spectral analysis on 58 archival *NuSTAR* observations of 30 bright X-ray pulsars. The 3–79 keV spectral continua of these selected sources were fitted with a model chosen on the basis of its fitting quality in 3–15 keV and model simplicity, and then inspected for the presence of the ‘10 keV feature’. Our analysis indicates the presence of such a feature in 16 out of 58 the *NuSTAR* observations of 11 different sources and is fitted with a Gaussian absorption model centred around 10 keV. Our analysis also suggests that such a feature could be wrongly detected if flare data is not analysed separately from persistent emission.

**Key words:** accretion, accretion discs – methods: data analysis – pulsars: general – X-rays: binaries.

## 1 INTRODUCTION

The spectrum of accreting X-ray pulsars (XRP) generally have a smooth broad-band continuum with a high energy cut-off along with some additional features like narrow K-shell emission lines of iron, thermal soft excess, cyclotron absorption line, etc. (See White, Swank & Holt 1983 and Nagase 1989). The X-ray spectral continuum carries information related to the photon generation mechanism and physical conditions at the X-ray emission site. Generally, we parametrize the X-ray spectral continuum using a set of simplified empirical models. The spectral continuum of XRP is generally described by a power law having high energy cutoff (Nagase 1989). The lack of ‘perfect’ theoretical models for representing the observed XRP spectra is owed to the complexity involved with the consistent calculation of the coupled radiation transfer and magnetohydrodynamics equations of the accretion flow (the accretion flow dynamics and radiation transfer are interdependent) at the location of origin of emergent spectra (Isenberg, Lamb & Wang 1998; Orlandini 2006). In addition to the power-law continuum, the physical origins of most of the observed XRP spectral features are well established, viz., the narrow fluorescence emission lines especially from iron, cyclotron resonance scattering feature (CRSF) due to electron–cyclotron resonance in the superstrong magnetic field near the surface of neutron star ( $B_{\text{NS}} \sim 10^{12}$  Gauss) (Harding 2003; Staubert et al. 2019), photoelectric absorption of the soft X-rays by the interstellar medium (ISM) and(or) circumstellar/circumbinary matter, absorption edges, soft excess of thermal origin due to hard

X-rays reprocessed by the inner accretion disc (Paul et al. 2002; Hickox, Narayan & Kallman 2004), etc.

High signal-to-noise ratio (SNR) data and the broad-band spectral coverage delivered by present-day X-ray space observatories facilitate detailed examination of characteristic features in XRP spectra. In this work, we explore the mysterious feature found in XRP spectra, introduced as a distinct spectral feature by Coburn et al. (2002) called as ‘The feature at 10 keV’ or the ‘10 keV feature’ (hereafter *TKF*). *TKF* appears as a bump or depression or wiggle around 10 keV in the residuals to the best-fitting spectral model and is generally modelled as a Gaussian emission or Gaussian absorption or a combination of these two models. This spectral feature has been observed in multiple XRP sources across different observatories viz., *Ginga* (Mihara 1995), *RXTE* (Coburn et al. 2002), *BeppoSAX* (Doroshenko et al. 2017a), *Suzaku* (Rivers et al. 2010), and *NuSTAR* (Fuerst et al. 2014b). The appearance of *TKF* in spectra from multiple observatories rules out the possibility of its instrumental origin. The most suspected reason for the origin of *TKF* is the common usage of oversimplified and imperfect phenomenological spectral continuum models to describe the high statistics X-ray spectral data from the sensitive modern observatories (Coburn et al. 2002; Vasco et al. 2013; and Doroshenko 2017). Reports of detection of *TKF* are sporadic, which impacts the selection of sources in an organized manner for its study. For instance, *TKF* may be reported in the spectrum of a particular source with data from a specific instrument (observatory) but may not be reported in the spectrum from another instrument. No particular pattern has been observed in the occurrence of *TKF* until now.

The broad-band (3–79 keV) focusing X-ray telescope *Nuclear Spectroscopic Telescope Array (NuSTAR)* is an instrument well suited

\* E-mail: hemanthm@rri.res.in

to study the *TKF*, as it covers the 10 keV spectral region by a factor of a few on either side with good spectral resolution and low background levels. Additionally, there is the availability of a large archival *NuSTAR* spectral data of multiple XRP. We selected some of the bright XRP for which *NuSTAR* archival observations were available and then surveyed the available literature for spectral analysis studies of these chosen sources with different instruments. All the previous report(s) of detection of *TKF* in these sources were noted down. We then tried to model the available *NuSTAR* spectra of these XRP with a suitable continuum model and check for the presence of *TKF* in them.

Since Coburn et al. (2002) presented *TKF* as a distinct spectral feature, it has been extensively reported in spectral analysis of XRP. Generally, an extra model component with a Gaussian absorption profile or a Gaussian emission profile or a combination of the two is used to account for the residuals remaining at  $\sim 10$  keV following the spectral fits. Coburn et al. (2002) also pointed out the residuals resembling *TKF* that were visible in spectral fits to *Ginga* observations of XRP in Mihara (1995). We surveyed the literature containing spectral analysis of XRP in the following manner. First, the X-ray observatories covering the spectral band 5–20 keV and having an adequate spectral resolution to resolve *TKF* (which usually turns up as a broad feature) were screened. This confined the survey to the large area counter instrument on *Ginga* (*Ginga*–LAC) spanning 1.5–37 keV with  $\sim 18$  per cent spectral resolution (Turner et al. 1989), the proportional counter array (*RXTE*–PCA) covering 2–60 keV with  $\sim 18$  per cent spectral resolution, and high energy X-ray timing experiment (*RXTE*–HEXTE) covering 15–250 keV with  $\sim 15$  per cent spectral resolution onboard *Rossi X-ray timing explorer* (Jahoda et al. 1996), the high pressure gas scintillation proportional counter (HPGSPC) (Manzo et al. 1997), and phoswich detection system (PDS) (Frontera et al. 1997) instruments onboard *BeppoSAX* (Boella et al. 1997) covering 4–120 keV, the joint European X-ray monitor (JEM–X) instrument onboard *INTEGRAL* covering 4–35 keV with  $\sim 10$  per cent spectral resolution (Lund et al. 2003), *Suzaku*–XIS (X-ray imaging spectrometer) with 0.2–12 keV coverage and  $\sim 2$  per cent spectral resolution, and *Suzaku*–HXD (Hard X-ray Detector) with 10–70 keV coverage and spectral resolution of 3.0 keV (Koyama et al. 2007 and Takahashi et al. 2007 respectively), *NuSTAR* (Harrison et al. 2013) and *AstroSat*–LAXPC (large area X-ray proportional counters) covering 3–80 keV with  $\sim 10$  per cent spectral resolution (Antia et al. 2017). For the selected bright XRP, we searched for the reported spectral analysis results using data from the aforementioned X-ray observatories.

A summary of the published results in the context of the *TKF* is given in Table 1. Out of the 30 selected sources given in the table, *TKF* has been reported at least once in 9 sources viz., Her X–1, Vela X–1, XTE J1946+274, 4U 1907+09, 4U 1538–52, Cep X–4, SMC X–1, GX 304–1, and EXO 2030+375. A graphical depiction of the survey is shown in Fig. 1. It is most commonly observed with *RXTE*–PCA observatory and for power-law continuum having a high energy cutoff *highcut*<sup>1</sup> (see Fig. 1). However, analysis of the same data by different groups also sometimes has given contrasting results regarding *TKF* (see for example Fürst et al. 2015; Vybornov et al. 2017; and Bhargava et al. 2019).

Many of the results mentioned before include combined spectral analysis using data from more than one instrument (except *Ginga*–LAC, *NuSTAR*, and *AstroSat*–LAXPC), often with a gap around 10–

15 keV which is above the energy range of the imaging instruments and below the energy range of the scintillator detectors. We have analysed archival data of 58 *NuSTAR* observations of 30 bright XRP to probe the *TKF*. The *NuSTAR* observations cover either side of the 10 keV with a single instrument, thus reducing systematic effects of cross-normalization of different instruments.

We have organized this paper in the following way: In Section 2, a brief description of *NuSTAR* instrument, the Data reduction steps followed, and a log of the *NuSTAR* observations that we have used for spectral analysis in this work are given. Section 3 explains the details of the spectral analysis performed. The results of the analysis and its discussion are given in Section 4.

## 2 INSTRUMENT, OBSERVATIONS, AND DATA REDUCTION

*NuSTAR* is an X-ray imaging spectroscopic observatory that covers the energy band by a factor of a few on either side of 10 keV with the same telescope and detector, making it an ideal instrument to probe the *TKF*. *NuSTAR* is the first hard X-ray focusing telescope and it provides spectral coverage in the 3–79 keV bandpass. It uses a pair of co-aligned Wolter–I telescopes to focus the source X-rays separately onto a pair of CdZnTe pixel detector arrays placed at 10 m focal length, referred to as FPMA (focal plane module A) and FPMB. Each FPM detector array has four  $2 \times 2 \times 0.2$  cm detectors. The spectral resolution below 50 keV is 400 eV full width at half-maximum, which is excellent for studying the relatively broad *TKF* feature (for detailed information on the *NuSTAR* observatory, refer Harrison et al. 2013). In addition, the uninterrupted broadband coverage from the instrument aids in modelling the spectral continuum in the best possible manner.

We followed the standard data reduction steps from the *NuSTAR* Data Analysis Software Guide<sup>3</sup> to extract the calibrated and screened source and background products. The task *nupipeline* v0.4.6 of HEASOFTv6.25<sup>4</sup> was first run on the raw data to obtain the filtered and calibrated data. Calibration database CALDB v1.0.2<sup>5</sup> was used for this purpose. Using DS9<sup>6</sup>, circular source and background region files are generated. The task *nuproducts* was then run to extract the source and background energy spectra as well as the redistribution matrix file (RMF) and ancillary response file (ARF). The extracted source spectrum was checked against the background spectrum, and the background-dominated energy range was excluded from the spectral analysis. A set of two spectra from two detector modules FPMA and FPMB were obtained for each observation. The spectra were then re-binned with the tool FTGROUPPHA<sup>7</sup> using the optimal binning scheme by Kaastra & Bleeker (2016).<sup>8</sup> Both the FPMA and FPMB spectra were fitted together in XSPEC v12.10.1 (Arnaud 1996), with an instrument relative normalization constant parameter left free to vary and all other model parameters tied together across both the spectra.

A catalogue of the sources and corresponding *NuSTAR* observation IDs used in this work is given in Table 2.

<sup>3</sup>[https://heasarc.gsfc.nasa.gov/docs/nustar/analysis/nustar\\_swguide.pdf](https://heasarc.gsfc.nasa.gov/docs/nustar/analysis/nustar_swguide.pdf)

<sup>4</sup><https://heasarc.gsfc.nasa.gov/docs/software/heasoft/>

<sup>5</sup><https://heasarc.gsfc.nasa.gov/docs/heasarc/caldb/nustar/>

<sup>6</sup><https://sites.google.com/cfa.harvard.edu/saomageds9>

<sup>7</sup><https://heasarc.gsfc.nasa.gov/heasoft/help/ftgrouppha.html>

<sup>8</sup>We verified that the best-fitting spectral parameters have no significant variation when using this binning scheme, compared to grouping with a minimum of 25 counts per bin.

<sup>1</sup>The model is explained in Section 3.

**Table 1.** For each source spectrum from the particular observatory, the spectral model used to fit the continuum in the literature is given. If a *TKF* was used for the spectral fit, then the cell is given in bold fonts. Whether the *TKF* is modelled like a dip (Gaussian absorption) or a hump (Gaussian emission) is shown with letters A (absorption) and E (emission), respectively. If the authors have not reported the presence of *TKF* for any observation, but residuals resembling *TKF* are visible in their best-fitting model, it is indicated with the letter R (residuals).

Source	Ginga	RXTE	BeppoSAX	INTEGRAL	Suzaku	NuSTAR	Astrosat	NuSTAR ( <i>itis work</i> )
<b>Her X-1</b>	PL <sup>4</sup>	HEC <sup>14</sup>	BPLHEC <sup>13</sup>	HEC <sup>12</sup>	NPEX <sup>15</sup>	HEC <sup>11</sup> (A)	HEC <sup>10</sup>	NPEX, HEC
	NPEX <sup>71</sup>	HEC <sup>16</sup> (E)	...	...	...	...	...	FDC (A)
<b>Vela X-1</b>	...	HEC <sup>26</sup> (R)	...	...	...	...	...	...
	NPEX <sup>4</sup>	NPEX <sup>5</sup> (A)	NPEX <sup>1</sup> (E)	CPL <sup>6</sup>	compTT <sup>9</sup>	FDC <sup>8</sup> (A)	...	compTT (A)
<b>XTE J1946+274</b>	PL <sup>3</sup>	HEC <sup>26</sup>	NPEX <sup>2</sup>	CPL <sup>7</sup>	NPEX <sup>10</sup>	...	...	CPL, compTT, HEC
	...	FDC <sup>52</sup>	compTT <sup>51</sup>	...	...	...	...	...
	...	FDC <sup>105</sup> (A)	FDC <sup>12</sup> (E)	FDC <sup>105</sup> (A)	HEC <sup>84</sup>	...	...	HEC (A)
	...	NPEX <sup>11</sup>	...	...	...	...	...	...
	...	HEC <sup>26</sup>	...	...	...	...	...	...
KS 1947+300	...	compTT <sup>69</sup>	compTT <sup>68</sup>	HEC <sup>38</sup>	CPL <sup>113</sup>	CPL <sup>67</sup>	...	HEC, NPEX
	4U 1907+09	HEC <sup>26</sup> (A)	HEC <sup>29</sup>	CPL <sup>30</sup>	FDC, HEC, NPEX <sup>27</sup> (E)	HEC, CPL <sup>157</sup> (A)	HEC <sup>81</sup>	compTT (A)
	...	...	...	...	NPEX <sup>84</sup>	...	FDC <sup>17</sup>	...
<b>4U 1538-52</b>	NPEX <sup>4</sup> (R)	HEC <sup>46</sup>	HEC <sup>48</sup>	CPL <sup>30</sup> (E)	...	HEC <sup>19</sup>	...	NPEX
	NPEX <sup>71</sup>	CPL <sup>18</sup> (A)	...	...	...	...	...	...
<b>Cep X-4</b>	HEC <sup>47</sup>	HEC <sup>26</sup> (A)	...	...	...	...	...	...
	NPEX <sup>71</sup>	FDC <sup>97</sup> (E)	...	...	NPEX <sup>95</sup>	FDC <sup>93</sup>	...	compTT, NPEX
	HEC <sup>94</sup>	...	...	...	...	FDC <sup>96</sup>	...	...
4U 1626-67	HEC <sup>114</sup>	...	...	...	...	FDC <sup>98</sup> (E)	...	FDC
	...	HEC <sup>26</sup>	HEC <sup>51</sup>	...	NPEX <sup>66</sup>	HEC <sup>83</sup>	...	...
SMC X-2	...	...	HEC <sup>64</sup>	...	HEC <sup>82</sup>	...	...	...
	IGR J17544-2619	...	CPL <sup>65</sup>	...	NPEX <sup>80</sup>	...	...	...
IGR J16393-4643	...	...	...	...	...	...	...	...
	2S 1553-542	BPL <sup>115</sup>	...	...	HEC <sup>104</sup>	...	...	compTT, NPEX
RX J0520.5-6932	...	...	...	...	...	...	...	...
	Cen X-3	HEC <sup>26</sup> (R)	compTT <sup>51</sup>	PCH <sup>54</sup>	FDC <sup>84</sup>	NPEX <sup>36</sup>	...	compTT, NPEX
GX 301-2	...	HEC <sup>26</sup> (R)	PCH <sup>52</sup> (R)	PCH <sup>55</sup>	NHC <sup>50</sup>	nltcomp <sup>99</sup>	...	NPEX
	...	...	HEC <sup>63</sup>	...	...	CPL <sup>103</sup>	...	NPEX (A)
XTE J1829-098	NPEX <sup>4</sup>	HEC <sup>25</sup>	NHC <sup>23</sup>	FDC <sup>22</sup>	FDC <sup>21</sup>	CPL <sup>116</sup>	...	FDC
	...	HEC <sup>26</sup>	...	FDC <sup>24</sup>	...	FDC <sup>28</sup>	...	CPL, NPEX (A)
V 0332+53	...	...	...	HEC <sup>54</sup>	...	NHC <sup>50</sup>	...	HEC (A)
	...	CPL <sup>38</sup>	...	compTT <sup>37</sup>	...	...	...	...
XTE J1858+034	NPEX <sup>4</sup>	CPL <sup>41</sup>	...	CPL <sup>40</sup>	...	...	...	...
	...	...	...	HEC <sup>42</sup>	...	...	...	...
4U 1700-67	NPEX <sup>71</sup>	...	...	HEC <sup>54</sup>	...	...	...	...
	...	HEC <sup>31</sup>	...	HEC <sup>32</sup>	...	...	...	NPEX
...	HEC <sup>115</sup>	2PL <sup>117</sup>	HEC <sup>41</sup>	...	NPEX <sup>116</sup>	NHC <sup>118</sup>	...	NPEX (A)
...	...	...	...	...	NHC <sup>116</sup>	...	...	...

**Table 1** – *continued*

Source	Ginga	RXTE	BeppoSAX	INTEGRAL	Suzaku	NuSTAR	Astrosat	NuSTAR ( <i>this work</i> )
LMC X-4	HEC <sup>120</sup> NPEX <sup>4</sup> HEC <sup>121</sup>	HEC <sup>123</sup> ... ...	HEC <sup>122</sup> PL <sup>124</sup> ...	HEC <sup>125</sup> HEC <sup>126</sup> ...	HEC <sup>127</sup> ...	compTT <sup>128</sup> ...	...	NPEX (A) NPEX, FDC, compTT ...
IGR J17329-2731	HEC <sup>133</sup>	HEC <sup>129</sup>	HEC <sup>132</sup>	PL <sup>119</sup>	CPL <sup>134</sup>	HEC <sup>119</sup>	...	NPEX HEC, FDC
SMC X-1	...	...	CompTT <sup>132</sup>	...	...	FDC <sup>130</sup> (E) NPEX <sup>131</sup>	...	NPEX HEC, FDC
GRO J1008-57	...	CPL <sup>138</sup>	...	CPL <sup>136</sup> CPL <sup>138</sup> HEC <sup>145</sup> CPL <sup>147</sup>	NPEX <sup>135</sup> CPL <sup>138</sup> FDC <sup>141</sup> NPEX <sup>141</sup> NPEX <sup>142</sup> HEC <sup>143</sup>	NPEX <sup>137</sup> 2compTT <sup>140</sup> 2compTT <sup>144</sup>	...	NPEX PL ...
GX 304-1	...	HEC <sup>146</sup> FDC, NPEX <sup>141</sup> HEC, CPL <sup>148</sup> (E)	...	...	...	...	...	NPEX PL ...
1A 0535+26	...	CPL <sup>85</sup> HEC <sup>87</sup> PL <sup>88</sup>	...	CPL <sup>85</sup> HEC <sup>87</sup> HEC <sup>91</sup>	CPL <sup>85</sup> NPEX <sup>84</sup>	CPL <sup>86</sup> 2compTT <sup>89</sup> CPL <sup>90</sup>	...	FDC, PL, 2compTT ...
GRO J2058+42	...	...	...	...	...	FDC <sup>153</sup> compTT <sup>155</sup>	FDC <sup>154</sup>	compTT (A) NHC CPL CPL
1E 1145.1-6141	...	HEC <sup>74</sup>	...	CPL <sup>72</sup> HEC <sup>62</sup>	HEC <sup>69</sup> HEC <sup>53</sup>	CPL <sup>73</sup> CPL <sup>59</sup>	PL <sup>61</sup>	CPL CPL
OAO 1657-415	HEC <sup>70</sup>	...	CPL <sup>45</sup>	...	HEC <sup>53</sup> HEC <sup>78</sup> HEC <sup>101</sup>	CPL <sup>60</sup> CPL <sup>75</sup> (A) HEC <sup>79</sup> HEC <sup>100</sup>	HEC <sup>79</sup>	NPEX CPL, NPEX (A) ...
EXO 2030+375	...	HEC <sup>76</sup> (A) HEC <sup>92</sup> HEC <sup>156</sup> PL <sup>151</sup>	...	HEC <sup>77</sup> (AE) compTT <sup>106</sup> HEC <sup>107</sup> PL <sup>44</sup>	...	compTT <sup>109</sup> ...	HEC <sup>108</sup>	NPEX CPL, NPEX (A) NPEX, FDC ...
IGR J19294+1816	...	PL <sup>52</sup>	...	...	...	...	HEC <sup>108</sup>	NPEX, FDC ...

*Notes.* PL: power law, 2PL: double power law, HEC: PL with hightecut, FDC: PL with Fermi-Dirac cutoff, NHC: newhcut, CPL: cut-off.p.l, NPEX: Negative positive exponential, BPL: Broken power law, BPLHEC: Broken power law with hightecut, compTT: Comptonization model, 2compTT: double compTT

NOTE – 4U 1700-37 is not an established XRP but it is included because of the reported CRSF.

References – <sup>1</sup>La Barbera et al. (2003), <sup>2</sup>Orlandini et al. (1998a), <sup>3</sup>Choi et al. (1996), <sup>4</sup>Mihara (1995), <sup>5</sup>Kreykenbohm et al. (2002), <sup>6</sup>Wang (2014b), <sup>7</sup>Schambe et al. (2007), <sup>8</sup>Fürst et al. (2014a), <sup>9</sup>Maitra & Paul (2013a), <sup>10</sup>Odaka et al. (2013), <sup>11</sup>Fürst et al. (2013), <sup>12</sup>Klochkov et al. (2007), <sup>13</sup>Fiume et al. (1998), <sup>14</sup>Gruber et al. (2001), <sup>15</sup>Enoto et al. (2013), <sup>16</sup>Vasco et al. (2008), <sup>17</sup>Varun et al. (2019a), <sup>18</sup>Rodes-Roca et al. (2009), <sup>19</sup>Hemphill et al. (2019), <sup>20</sup>Fürst et al. (2018), <sup>21</sup>Suchy et al. (2012), <sup>22</sup>Doroshenko et al. (2010), <sup>23</sup>La Barbera et al. (2005), <sup>24</sup>Kreykenbohm et al. (2004), <sup>25</sup>Mukherjee & Paul (2004), <sup>26</sup>Coburn et al. (2002), <sup>27</sup>Rivers et al. (2010), <sup>28</sup>Tendulkar et al. (2014), <sup>29</sup>Cusumano et al. (2000), <sup>30</sup>Hemphill et al. (2013), <sup>31</sup>Mukherjee et al. (2006a), <sup>32</sup>Doroshenko et al. (2008), <sup>33</sup>Nagase et al. (1992), <sup>34</sup>Devaraj & Paul (2022), <sup>35</sup>Jaisawal & Naik (2017), <sup>36</sup>Devaraj & Naik (2016), <sup>37</sup>Baum, Cherry & Rodi (2017), <sup>38</sup>Lutovinov et al. (2015), <sup>39</sup>Makishima et al. (1990), <sup>40</sup>Kreykenbohm et al. (2006), <sup>41</sup>Tsygankov et al. (2006), <sup>42</sup>Ferrigno et al. (2016), <sup>43</sup>Sitykovsky et al. (2019), <sup>44</sup>Roy, Choudhury & Agrawal (2017), <sup>45</sup>Orlandini et al. (1999), <sup>46</sup>Mukherjee et al. (2006b), <sup>47</sup>Clark et al. (1990), <sup>48</sup>Robba et al. (2000), <sup>49</sup>Jaisawal & Naik (2014), <sup>50</sup>Tomar, Pradhan & Paul (2021), <sup>51</sup>Doroshenko (2017), <sup>52</sup>Kreykenbohm et al. (1998), <sup>53</sup>Filippova et al. (2005), <sup>54</sup>Filippova et al. (2000), <sup>55</sup>Burderi et al. (2000), <sup>56</sup>Vybornov et al. (2018), <sup>57</sup>Doroshenko et al. (2017b), <sup>58</sup>Tsygankov & Lutovinov (2005a), <sup>59</sup>Saavedra et al. (2022), <sup>60</sup>Sharma et al. (2022), <sup>61</sup>Jaisawal et al. (2021b), <sup>62</sup>Barnstedt et al. (2008), <sup>63</sup>La Barbera et al. (2004), <sup>64</sup>Orlandini et al. (1998b), <sup>65</sup>Owens, Oosterbroek & Parmar (1997), <sup>66</sup>Iwakiri et al. (2012), <sup>67</sup>Fürst et al. (2014c), <sup>68</sup>Naik et al. (2006), <sup>69</sup>Galloway, Morgan & Levine (2004), <sup>70</sup>Kamata et al. (1990), <sup>71</sup>Makishima et al. (1990), <sup>72</sup>Ferrigno et al. (2008), <sup>73</sup>Ghising et al. (2022), <sup>74</sup>Ray & Chakrabarty (2002), <sup>75</sup>Tamang et al. (2022), <sup>76</sup>Wilson, Finger & Camero-Aranz (2008), <sup>77</sup>Klochkov et al. (2008), <sup>78</sup>Naik & Jaisawal (2015), <sup>79</sup>Jaisawal et al. (2021a), <sup>80</sup>Iwakiri et al. (2019), <sup>81</sup>Varun et al. (2019b), <sup>82</sup>Camero-Aranz et al. (2012), <sup>83</sup>D’Ai et al. (2017), <sup>84</sup>Maitra & Paul (2013b), <sup>85</sup>Caballero et al. (2013), <sup>86</sup>Balhausen et al. (2012), <sup>87</sup>Müller et al. (1996), <sup>88</sup>Balhausen et al. (2012), <sup>89</sup>Martinez Núñez et al. (2012), <sup>90</sup>Camero-Aranz et al. (2012), <sup>91</sup>Sartore, Jourdain & Roques (2015), <sup>92</sup>Epili et al. (2017), <sup>93</sup>Fürst et al. (2015), <sup>94</sup>Koyama et al. (1991), <sup>95</sup>Jaisawal & Naik (2015b), <sup>96</sup>Bhargava et al. (2019), <sup>97</sup>McBride et al. (2007), <sup>98</sup>Vybornov et al. (2017), <sup>99</sup>Bhalerao et al. (2015), <sup>100</sup>Fürst et al. (2017), <sup>101</sup>Naik et al. (2013), <sup>102</sup>Bodaghee et al. (2016), <sup>103</sup>Islam et al. (2015), <sup>104</sup>Wilson, Finger & Camero-Aranz (2012), <sup>105</sup>Müller et al. (1996), <sup>106</sup>Camero-Aranz et al. (2012), <sup>107</sup>Martinez Núñez et al. (2012), <sup>108</sup>Raman et al. (2021), <sup>109</sup>Tsygankov et al. (2019c), <sup>110</sup>Bala et al. (2020b), <sup>111</sup>Heindl et al. (2001), <sup>112</sup>Doroshenko et al. (2017a), <sup>113</sup>Balhausen et al. (2016), <sup>114</sup>Mihara et al. (1991), <sup>115</sup>Pahari & Pal (2012), <sup>116</sup>Tsygankov & Naik (2015a), <sup>117</sup>Seifina, Titarchuk & Shaposhnikov (2016), <sup>118</sup>Bala, Roy & Bhattacharya (2020a), <sup>119</sup>Bozzo et al. (2018), <sup>120</sup>Levine et al. (1991), <sup>121</sup>Woo et al. (1996), <sup>122</sup>La Barbera et al. (2001), <sup>123</sup>Naik & Paul (2004b), <sup>124</sup>Naik & Paul (2004a), <sup>125</sup>Lutovinov et al. (2004), <sup>126</sup>Tsygankov & Lutovinov (2005b), <sup>127</sup>Hung et al. (2010), <sup>128</sup>Shytkovsky et al. (2017), <sup>129</sup>Inam, Baykal & Bekten (2010), <sup>130</sup>Pike et al. (2019), <sup>131</sup>Brumbaek et al. (2020), <sup>132</sup>Naik & Paul (2004a), <sup>133</sup>Woo et al. (1995), <sup>134</sup>Pradhan, Maitra & Paul (2020), <sup>135</sup>Yamamoto et al. (2014), <sup>136</sup>Wang (2014a), <sup>137</sup>Bellm et al. (2014), <sup>138</sup>Kühnel et al. (2013), <sup>139</sup>Naik et al. (2011), <sup>140</sup>Lutovinov et al. (2021), <sup>141</sup>Yamamoto et al. (2011), <sup>142</sup>Jaisawal, Naik & Epili (2016), <sup>143</sup>Pradhan et al. (2019a), <sup>144</sup>Tsygankov et al. (2019a), <sup>145</sup>Klochkov et al. (2012), <sup>146</sup>Devasia et al. (2011), <sup>147</sup>Malacaria et al. (2015), <sup>148</sup>Rothschild et al. (2017), <sup>149</sup>Haberl & Day (1992), <sup>150</sup>Reynolds et al. (1999), <sup>151</sup>Rodriguez et al. (2009), <sup>152</sup>Roy et al. (2017), <sup>153</sup>Kabiraj & Paul (2020), <sup>154</sup>Mukherjee, Antia & Katoch (2020), <sup>155</sup>Molkov et al. (2019), <sup>156</sup>Reig & Coe (1999), <sup>157</sup>Tobrej et al. (2023), <sup>158</sup>Diez et al. (2022).

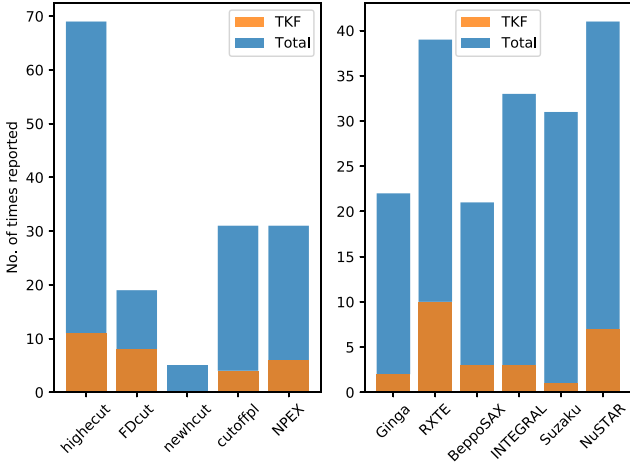


**Figure 1.** The bar chart shows the specifics of the performed survey (Table 1). The distribution of reports of *TKF* for different continuum models, and from different observatories<sup>2</sup> are shown.

### 3 TIME-AVERAGED SPECTROSCOPY

We have performed the time-averaged spectral analysis on the *NuSTAR* pointed observations of sources listed in Table 2 in the 3–79 keV spectral band unless otherwise specified. The light curves of some of the observations showed the presence of flares (see Table 2). In those cases, the flare and out-of-flare spectra were separately generated and then analysed.<sup>9</sup> The spectra were fitted with a composite model of the following form

$$\frac{dN}{dE} = e^{-\sigma_{\text{abs}}(E)} \times (f e^{-\sigma_{\text{abs,local}}(E)} + (1-f)) \times [\text{continuum}(E) \times \text{gabs}_{\text{TKF}}(E) + \text{Gaussian}_{\text{Fe}}(E) + \text{bbody}(E)] \times \text{gabs}_{\text{CRSF}}(E). \quad (1)$$

$e^{-\sigma_{\text{abs}}(E)}$  denotes absorption by the ISM and was modelled with the Tuebingen-Boulder ISM absorption model (`tbabs`) using ISM abundances from Wilms, Allen & McCray (2000) and photoelectric absorption cross-sections from Verner et al. (1996). For the observations in which the Galactic absorption column density towards the source could not get constrained by the fit, the absorption column density was frozen to the Galactic line-of-sight value obtained from the tool *w3nh*.<sup>10</sup> Local absorption was modelled by multiplying the spectrum with a partial covering absorption model of the form  $f e^{-\sigma_{\text{abs,local}}(E)} + (1-f)$ . The implication of this modified Tuebingen-Boulder ISM absorption model (`tbpcf`) is that only a fraction  $f$  of the total X-ray flux is absorbed, while the remaining fraction  $(1-f)$  of the flux travels unabsorbed (see Maitra & Paul 2013b). The redshift parameter of `tbpcf` model was fixed to 0. The soft excess was modelled with a blackbody spectrum model `bbody`. *TKF* was modelled with a Gaussian absorption model `gabs`.

The spectral continuum is modelled with a physical Comptonization model like `compTT` (Titarchuk 1994) or one of the following phenomenological power law based continuum models:

$$\text{powerlaw} = A \times E^{-\Gamma}$$

$$\text{cutoffpl} = A \times E^{-\Gamma} \exp\left(-\frac{E}{E_{\text{cut}}}\right)$$

<sup>9</sup>We consider any spike in the light curve as a flare if the ratio of the peak count rate of the spike to the average count rate outside the spike is greater than 3.

<sup>10</sup><https://heasarc.gsfc.nasa.gov/cgi-bin/Tools/w3nh/w3nh.pl>

$$\text{powerlaw} \times \text{mplcut} = \begin{cases} A \times E^{-\Gamma} \exp\left(-\frac{(E-E_{\text{cut}})^2}{(0.1E_{\text{cut}})^2}\right) & E < E_{\text{cut}} \\ A \times E^{-\Gamma} \exp\left(-\frac{E-E_{\text{cut}}}{E_{\text{fold}}}\right) \exp\left(-\frac{(E-E_{\text{cut}})^2}{(0.1E_{\text{cut}})^2}\right) & E \geq E_{\text{cut}} \end{cases}$$

$$\text{powerlaw} \times \text{FDcut} = \begin{cases} A \times E^{-\Gamma} & E < E_{\text{cut}} \\ A \times E^{-\Gamma} \times 1 / \left[1 + \exp\left(-\frac{E-E_{\text{cut}}}{E_{\text{fold}}}\right)\right] & E \geq E_{\text{cut}} \end{cases}$$

$$\text{powerlaw} \times \text{newhcut} = \begin{cases} A \times E^{-\Gamma} & E \leq E_{\text{cut}} - \Delta E \\ c_0 + c_1 E + c_2 E^2 + c_3 E^3 & E_{\text{cut}} - \Delta E < E < E_{\text{cut}} + \Delta E \\ A \times E^{-\Gamma} \exp\left(-\frac{E-E_{\text{cut}}}{E_{\text{fold}}}\right) & E \geq E_{\text{cut}} + \Delta E \end{cases}$$

$$\text{NPEx} = (A_1 \times E^2 + A_2 \times E^{-\Gamma}) \exp\left(-\frac{E}{E_{\text{cut}}}\right)$$

`highcut` (White et al. 1983) represents a power-law continuum modified by an exponential roll-off above energy  $E_{\text{cut}}$ . `mplcut` (Coburn et al. 2002) is a slightly modified version of `highcut` wherein the abrupt break in continuum at  $E_{\text{cut}}$  is smoothed out with a Gaussian absorption model (`gabs` in XSPEC). Similarly, `FDcut` (Tanaka 1986) has a Fermi-Dirac distribution-like function and `newhcut` (Burderi et al. 2000) has a third-order polynomial function to smoothen the kink at  $E_{\text{cut}}$ .<sup>11</sup> `NPEx` (Mihara 1995) is a combination of two cutoff power-law functions, with the photon-index of one of the power-law components fixed to 2. `NPEx` mimics saturated inverse Compton scattering. `CRSF` was modelled with a Gaussian absorption profile (`gabs`) and iron fluorescence line with simple Gaussian (`Gaussian`). `newhcut` and `FDcut` are local models installed into XSPEC. All other spectral models used in this work are available in XSPEC.<sup>12</sup>

### 3.1 Spectral analysis and model selection methodology

Our aim is to search for the best-fitting composite spectral model for each *NuSTAR* observation (Table 2) and check if it contains the *TKF* model component. We employed a two-step spectral fitting process invoking the Akaike information criterion (Akaike 1998) for finding the best-fitting model. The AIC score for a model fit is given by

$$\text{AIC} = 2n - 2\ln(L_{\text{max}}) = 2n + \chi_{\text{min}}^2.$$

Here,  $L_{\text{max}}$  is the maximum value of likelihood and  $-2\ln(L_{\text{max}}) = \chi_{\text{min}}^2$  is the equivalent minimum value of the fit statistic, and  $n$  is the number of model parameters. As evident from the equation, AIC score will be low for a model that fits the data well, but it increases with the complexity of the model (based on the number of model parameters). We compared the AIC scores of all the composite models derived from equation (1) after they were fitted to the spectrum of each observation, and chose the best-fitting model based on the lowest AIC score.

Since the primary interest of this work is to identify the presence/absence of a spectral feature near 10 keV, we employed a two-step spectral fitting procedure so that importance is given to the 10 keV spectral band in the selection of the best-fitting composite model.

#### 3.1.1 Training and validation

We performed an initial manual fit on the broad-band spectrum of each observation (Table 2) to identify the presence of iron fluorescence line(s) and `CRSF`(s) in the spectrum. The spectrum from each observation in 3–15 keV (the *TKF* band) and 3–79 keV

<sup>11</sup>We have consistently used  $\Delta E = 5$  keV for the `newhcut` model throughout the analysis.

<sup>12</sup><https://heasarc.gsfc.nasa.gov/xanadu/xspec/manual/Models.html>

**Table 2.** *NuSTAR* Observations catalogue with the details of the source and observation IDs used in this work. The observation IDs having flare in the light curve have the letter ‘*F*’ superscripted.

Obs. Sn.	Source	<i>NuSTAR</i> Obs. ID	start (DATE-OBS)	stop (DATE-END)	Exposure (ks)	FPMA count rate (cts s <sup>-1</sup> )
1	Her X-1	30002006002	2012-09-19 08:26:07	2012-09-20 01:06:07	27.7	34
2		30002006005	2012-09-22 04:26:07	2012-09-22 18:36:07	21.9	90
3		10202002002	2016-08-20 04:31:08	2016-08-21 06:21:08	36.6	80
4	Vela X-1	10002007001	2012-07-09 13:16:07	2012-07-09 23:06:07	10.8	135
5		30002007002	2013-04-22 12:16:07	2013-04-22 20:11:07	7.14	67
6		30002007003	2013-04-22 20:11:07	2013-04-23 19:06:07	24.5	43
7		90402339002 <sup>F</sup>	2019-01-10 04:11:09	2019-01-11 02:26:09	36.0	41
8	XTE J1946+274	90401328002	2018-06-24 11:26:09	2018-06-25 15:36:09	47.2	36
9	KS 1947+300	80002015002	2013-10-21 18:36:07	2013-10-22 05:46:07	18.36	72
10		80002015004	2013-11-22 21:26:07	2013-11-23 09:31:07	18.59	82
11		80002015006	2013-12-09 15:51:07	2013-12-10 07:41:07	27.29	65
12	4U 1907+09	30401018002	2018-08-01 12:41:09	2018-08-03 07:41:09	78.86	7
13	4U 1538-52	30201028002	2016-08-11 19:11:08	2016-08-12 19:16:08	11.1	7
14	Cep X-4	80002016002	2014-06-18 22:01:07	2014-06-19 20:11:07	40.4	44
15		80002016004	2014-07-01 10:16:07	2014-07-02 07:26:07	41.16	12
16	4U 1626-67	30101029002	2015-05-04 12:26:07	2015-05-05 20:41:07	65.0	15
17	SMC X-2	90102014002	2015-09-25 21:51:08	2015-09-26 11:21:08	24.51	19
18		90102014004	2015-10-12 21:41:08	2015-10-13 12:06:08	23.06	9
19		90101017002	2015-10-21 21:31:08	2015-10-22 11:16:08	26.72	6
20	IGR J17544-2619	30002003003	2013-06-19 09:31:07	2013-06-19 23:41:07	26.3	26
21	IGR J16393-4643	30001008002	2014-06-26 02:21:07	2014-06-27 05:31:07	50.57	0.54
22	2S 1553-542	90101002002	2015-04-03 11:36:07	2015-04-04 01:46:07	27.42	19
23	RX J0520.5-6932	80001002002	2014-01-22 20:16:07	2014-01-23 11:36:07	27.75	14
24		80001002004	2014-01-24 23:56:07	2014-01-25 18:31:07	33.2	16
25	Cen X-3	30101055002	2015-11-30 18:11:08	2015-12-01 05:01:08	21.4	65
26	GX 301-2	30001041002	2014-10-29 07:41:07	2014-10-29 22:01:07	38.2	12
27		30101042002 <sup>F</sup>	2015-10-04 08:01:08	2015-10-04 22:41:08	35.7	19
28	XTE J1829-098	90401332002	2018-08-16 02:11:09	2018-08-16 18:01:09	27.8	6
29	V0332+53	80102002008	2015-09-30 22:51:08	2015-10-01 09:46:08	18.1	37
30		80102002010	2015-10-04 23:36:08	2015-10-05 11:51:08	20.1	21
31		90202031002	2016-07-30 18:01:08	2016-07-31 06:31:08	25.2	12
32		90202031004	2016-07-31 18:06:08	2016-08-01 06:46:08	25.0	10
33	XTE J1858+034	90501348002	2019-11-03 06:56:09	2019-11-04 08:31:09	43.7	17
34	4U 1700-37	30101027002 <sup>F</sup>	2016-03-01 10:21:08	2016-03-02 07:31:08	38.0	23
35	LMC X-4	30102041002 <sup>F</sup>	2015-10-30 01:01:08	2015-10-30 12:46:08	24.5	13
36		30102041004	2015-11-04 19:46:08	2015-11-05 05:56:08	21.9	10
37		30102041006	2015-11-11 11:16:08	2015-11-11 22:36:08	22.9	3
38		30102041008 <sup>F</sup>	2015-11-27 09:16:08	2015-11-27 20:31:08	20.3	10
39	IGR J17329-2731	90301012002	2017-08-29 15:36:09	2017-08-30 02:36:09	20.8	3
40	SMC X-1	30202004002	2016-09-08 21:26:08	2016-09-09 09:06:08	22.5	21
41		30202004004	2016-09-19 07:11:08	2016-09-19 19:06:08	21.2	15
42		30202004006	2016-10-01 00:56:08	2016-10-01 12:01:08	20.4	1.52
43		30202004008	2016-10-24 19:31:08	2016-10-25 07:36:08	20.8	24
44	GRO J1008-57	80001001002	2012-11-30 08:41:07	2012-11-30 17:31:07	12.4	227
45	GX 304-1	90401326002	2018-06-03 05:56:09	2018-06-04 12:06:09	58.1	0.21
46	1A 0535+26	80001016002	2015-02-11 04:11:07	2015-02-11 16:21:07	21.4	36
47		80001016004	2015-02-14 01:36:07	2015-02-14 17:31:07	29.7	14
48		90401370001	2018-12-26 02:41:09	2018-12-27 12:11:09	54.9	68
49	GRO J2058+42	90501313002	2019-03-25 07:06:09	2019-03-25 19:26:09	20.4	38
50		90501313004	2019-04-11 00:11:09	2019-04-11 22:11:09	38.6	42
51		90501336002	2019-08-28 12:36:09	2019-08-29 09:26:09	38.5	4
52	1E 1145.1-6141	30501002002	2019-07-23 10:56:09	2019-07-24 07:26:09	44.2	7.3
53	OA0 1657-415	30401019002	2019-03-25 07:06:09	2019-06-13 08:01:09	74.7	7.6
54	EXO 2030+375	90201029002	2016-07-25 08:36:08	2016-07-26 17:11:08	56.7	2.6
55		90701336002	2021-11-08 03:31:09	2021-11-08 17:56:09	23.5	71
56		80701320002	2021-08-30 00:56:09	2021-08-31 03:56:09	32.4	194
57	IGR J19294+1816	90401306002	2018-03-02 21:56:09	2018-03-03 20:06:09	40.6	0.06
58		90401306004	2018-03-16 03:11:09	2018-03-17 01:31:09	40.4	2.1

(broad-band) was treated as two separate data sets, and we named them the ‘Training’ data set and the ‘Validation’ data set, respectively.

The 3–15 keV training data set spectra were fitted with every possible composite model combination derived from

$$\frac{dN}{dE} = e^{-\sigma_{\text{abs}}(E)} \times (f e^{-\sigma_{\text{abs,local}}(E)} + (1-f)) \times [\text{continuum}(E) \times \text{gabs}_{\text{TKF}} + \text{Gaussian}_{\text{Fe}}(E) + \text{bbody}(E)]. \quad (2)$$

The combinations were identified, ensuring that the continuum, `tbaabs`, and `Gaussian` (if iron emission line is present) were included in all of them. Since the cutoff energy of most pulsars is beyond 15 keV, continuum models without a high energy cutoff (`powerlaw`, `cutoffpl`, `NPEX`, and `compTT`) were only used for training. A total of 32 composite model candidates (without high energy cutoff continuum models) were tested on each training set.

The performance of each candidate model on the training set was evaluated based on AIC. Only those models were considered in which all the spectral parameters were within the globally accepted ranges. The accepted ranges of various spectral model parameters were chosen as follows: Galactic absorption column density as per the source, partial covering absorption column density less than  $10^{25}$  atoms  $\text{cm}^{-2}$ , power-law index between 0 and 3, high energy cutoff between 0 and 40 keV,  $T_0$ , kT, and  $\tau$  of `compTT` between 0.01–5 keV, 2–100 keV, and 0.01–100, respectively, the line centre and line width of iron fluorescence emission between 6.2–6.8 and 0–1 keV, respectively, temperature kT of `bbody` between 0.01 and 3 keV, and the centre and width of the `gabs` used to model the *TKF* between 9–12 and 0–3 keV, respectively.

The best-fitting training model so identified (having the lowest AIC), along with other models within 5 per cent AIC score (or sometimes 10 per cent AIC in case the 5 per cent does not contain multiple candidates) were selected for fitting the 3–79 keV broad-band validation data set. The validation was performed after including the extra `gabs` or `cyclabs` model component(s) to account for CRSF(s). If any of the training-screened composite models contain a simple `powerlaw` continuum, in addition to it, the same composite model after modifying with different kinds of high energy cutoff (`mplcut`, `newhcut`, `newhcut`) was also tested on the validation data set. The best-fitting composite model on the validation data set was selected based on the lowest AIC score and best-fitting spectral parameters within the accepted ranges.

However, it was observed in some spectral data sets that none of the best-fitting training models would fit the validation data set well. In those cases, the training was skipped and single-step validation was performed using all the possible 56 composite model combinations derived from equation (2) (including the high energy cutoff continuum models) and the best-fitting model was selected following the same model screening procedure.

We report the presence of *TKF* only when all the best-fitting composite model(s) on the validation data set within the top 5 per cent AIC contain *TKF* model component.

The rest of this section briefs the details of each source and explains the spectral analysis performed on their *NuSTAR* observations. In each observation, the background-dominated spectral range is excluded from the fitting process. The figure showing the best-fitting model (the unfolded spectrum and model in  $E \frac{dN}{dE}$  as solid curves, the contribution of additive model components as dotted curves) and residuals to the best-fitting model for one observation containing *TKF* and one observation not containing *TKF*, based on availability, of each source are also given. In case *TKF* is required in the fit, a third panel showing the significance of *TKF* is also included. The data points from the FPMA instrument are shown in black and

FPMB are shown in red. The fit statistic is  $\chi^2$  distributed in all the observations except Obs. Sn.45. The tables containing best-fitting spectral parameter values for each observation are given across four tables in Appendix A.

### 3.2 Her X–1

Hercules X–1 is a moderately bright, persistent, eclipsing intermediate mass X-ray binary pulsar with 1.24 s spin period (Tananbaum et al. 1972) located 6.6 kpc away, hosting a NS and a 2.3  $M_{\odot}$  optical companion (Hz Her) in a low eccentricity orbit. Nearly edge-on view of the binary manifests as periodic  $\sim 1.7$  d intensity variation in the X-ray light curve in the form of eclipses. In addition, it also exhibits a 35 d intensity modulation due to absorption by a precessing warped accretion disc (Giacconi et al. 1973). The first ever report of CRSF in an XRP spectrum was with the balloon observations of Her X–1 (Truemper et al. 1978). The broad-band spectrum of Her X–1 is usually modelled with an absorbed power-law continuum with iron fluorescence lines, modified by CRSF at  $\sim 38$  keV (See Xiao et al. 2019).

We analysed the spectra from the observations Obs. Sn.1, 2, and 3 (Table 2). Obs. Sn.1 spans the eclipse and out-of-eclipse orbital phases of the binary. Therefore, the time average spectrum and out-of-the-eclipse phase spectrum of Obs. Sn.1 were analysed. Galactic absorption towards the source could not be constrained by the fit, therefore we fixed it to the Galactic value of  $1.5 \times 10^{20}$  atoms  $\text{cm}^{-2}$ . The iron emission line region is complex, and we modelled it with the combination of a narrow and a broad `Gaussian` (adopted from Fürst et al. 2013). CRSF at  $\sim 38$  keV was fitted with a `gabs` model.

None of the best-fitting training models could fit the validation data sets of Obs. Sn.2 and 3. Therefore, single-step fitting was performed on Obs. Sn.2 and 3 skipping training. The best-fitting models on the time-averaged and out-of-eclipse spectrum of Obs. Sn.1 does not contain *TKF*. The best-fitting models on Obs. Sn.2 and 3 contain *TKF*.

The spectral parameters of the best-fitting models for all three observations of Her X–1 are given in Tables A1 and A2. The spectral fit for the time-averaged spectrum of Obs. Sn. 1 (having no *TKF*) and Obs. Sn. 2 (having *TKF*) are shown in Fig. 2.

### 3.3 Vela X–1

Vela X–1 (4U 0900–40) is a bright and persistent eclipsing high mass X-ray binary (HMXB) pulsar hosting a NS and a B-type Supergiant stellar companion, located 1.9 kpc away. The XRP has a spin period of  $\sim 283$  s, and the binary has an orbital period of  $\sim 8.9$  d. Even though the typical X-ray luminosity of the pulsar is about  $4 \times 10^{36}$  erg  $\text{s}^{-1}$ , the relatively compact orbital separation keeps the pulsar embedded in the clumpy stellar wind of the companion, and this shows up as strong variability in XRP luminosity. CRSF has been detected in the source spectrum at two energies, with the fundamental line at  $\sim 25$  keV and its harmonic at  $\sim 55$  keV (see Kreykenbohm et al. 2002 and references therein, Maitra & Paul 2013a, and Fürst et al. 2014a).

We analysed the spectra from four observations Obs. Sn.4, 5, 6, and 7 (Table 2). Because of the presence of flare in Obs. Sn.7, we analysed the flaring state spectra of Obs. Sn.7. We could not get satisfactory fits for the time-averaged and out-of-flare-state spectra of Obs. Sn.7 due to the presence of a narrow absorptive feature around 7 keV. Galactic absorption towards the source could not be constrained by the fit, therefore we fixed it to the Galactic value of  $3.7 \times 10^{21}$  atoms  $\text{cm}^{-2}$ . Iron line emission was fitted with a `Gaussian` model. The fundamental CRSF at  $\sim 25$  keV and its harmonic at  $\sim 50$  keV were fitted with two `gabs` model components. The width of CRSF was

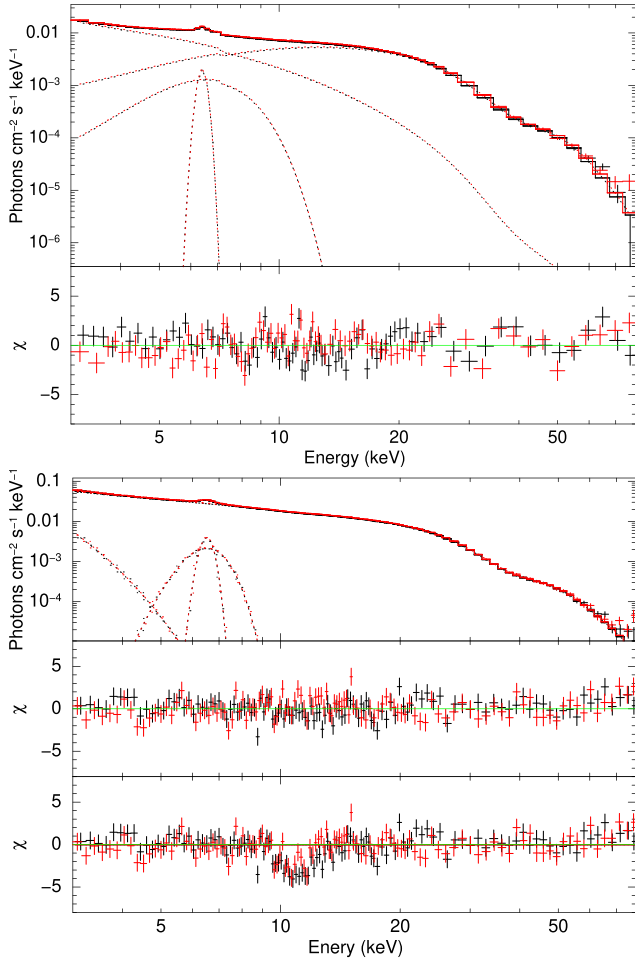


**Figure 2.** Top: Spectral fit on Her X–1 Obs. Sn.1 with `NPEX` continuum model, having no *TKF*. The top panel shows the best-fitting model and the bottom panel shows the residuals to the best-fitting model. Bottom: Spectral fit on Her X–1 Obs. Sn.2. with `FDecut` continuum model having *TKF*. The top panel shows the best-fitting model, the middle panel shows the residuals to the best-fitting model, and the bottom panel shows the residuals when the strength of the `gabs` component modelling *TKF* is set to 0.

not constrained by the fit in Obs. Sn.4, it was thus fixed to the average width obtained from other observations. The width of CRSF was also not constrained by the fit in the best-fitting model containing *TKF* in Obs. Sn.6, it was fixed to the width from the best-fitting model on Obs. Sn.6 not containing *TKF*.

The best-fitting models on Obs. Sn.5 and 7 do not contain *TKF*, while the best-fitting model on Obs. Sn.4 contains *TKF*. Even though the best-fitting model Obs. Sn.6 contains *TKF*, there also exists a similar well-fitting model in which *TKF* is absent.

The spectral parameters of the best-fitting models for all four observations of Vela X–1 are given in Tables A1 and A2. The spectral fit for the time-averaged spectrum of Obs. Sn. 4 (having *TKF*) and Obs. Sn.2 (having no *TKF*) are shown in Fig. 3.

### 3.4 XTE J1946+274

XTE J1946+274 is a transient HMXB pulsar at a distance of  $9.5 \pm 2.9$  kpc, in which the binary hosts the NS and a Be-type stellar companion. The pulsar has a spin period of about 15.8 s, and the binary has an orbital period of about 169 d (see Doroshenko et al.

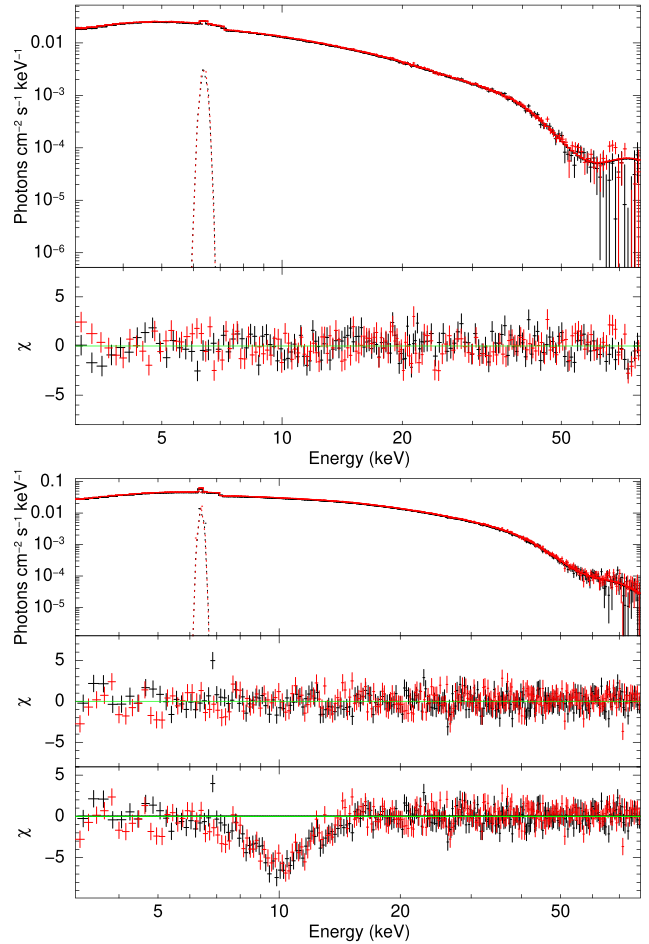


**Figure 3.** Top: Spectral fit on Vela X–1 Obs. Sn.5 with `cutoffpl` continuum model, having no *TKF*. The top panel shows the best-fitting model and the bottom panel shows the residuals to the best-fitting model. Bottom: Spectral fit on Vela X–1 Obs. Sn.4. with `compTT` continuum model, having *TKF*. The top panel shows the best-fitting model, the middle panel shows the residuals to the best-fitting model, and the bottom panel shows the residuals when the strength of the `gabs` component modelling *TKF* is set to 0.

2017a, and references therein). Interaction between the circumstellar equatorial disc of the Be companion and the pulsar at the periastron in a moderately eccentric orbit results in violent X-ray outbursts which appear as variability in the long-term X-ray light curve (Wilson et al. 2003). CRSF has been reported in the source spectrum at  $\sim 38$  keV (Heindl et al. 2001; Maitra & Paul 2013b; Doroshenko et al. 2017a; Devaraj & Paul 2022) and also at  $\sim 25$  keV (Müller et al. 2012).

We analysed the 3–60 keV spectrum from Obs. Sn.8 (Table 2). Iron fluorescence line was present, which was fitted with a Gaussian. CRSF centred around 40 keV was fitted with `gabs`.

The best-fitting model on Obs. Sn.8 contains *TKF*.

The spectral parameters of the best-fitting models for Obs. Sn.8 of XTE J1946+274 are given in Tables A1 and A2. The spectral fit for the time-averaged spectrum of Obs. Sn.8 (having *TKF*) is shown in Fig. 4

### 3.5 KS 1947+300

KS 1947+300 is a transient XRP in an HMXB hosting the NS and Be-companion star in an almost circular orbit. The binary orbital period is about 41.5 d, and the pulsar has a spin period of 18.8 s



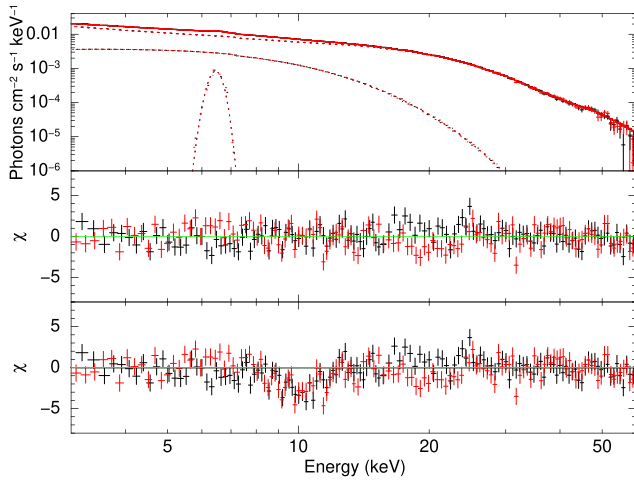


**Figure 4.** Spectral fit on XTE J1946+274 Obs. Sn.8 using `mplcut` model, having `TKF`. The top panel shows the best-fitting model, the middle panel shows the residuals to the best-fitting model, and the bottom panel shows the residuals when the strength of the `gabs` component modelling `TKF` is set to 0.

(Fürst et al. 2014c, and references therein). CRSF was first reported in the *NuSTAR* spectrum of the source by Fürst et al. (2014c), but this discovery is debated (Doroshenko et al. 2020). Fürst et al. (2014c) reported that the absorption feature detected in Obs. Sn.10 (for `highcut` model) could be CRSF. However, in a revisit of the same data and earlier *BeppoSAX* observations, Doroshenko et al. (2020) reported that a two-component `compTT` continuum model does not show such a prominent absorption feature and hence questioning the claim of CRSF.

We analysed the spectra from three observations Obs. Sn.9, 10, and 11 (Table 2), the same ones reported in Fürst et al. (2014c) and Doroshenko et al. (2020). The three observations covered the increase, peak, and decline phase of the 2013 outburst of the source. Galactic absorption column density could be constrained by the fit. Iron fluorescence line was fitted with a `Gaussian`.

None of the best-fitting training models could fit the validation data sets of Obs. Sn.9 and 10. Therefore, single-step fitting was performed on Obs. Sn.9 and 10 skipping training. The best models for validation were based on the top 10 per cent AIC on the training data set of Obs. Sn.11 because only one model was in the top 5 per cent AIC. The best-fitting models on Obs. Sn.9 and 10 does not contain `TKF`. The best-fitting model from training-validation on Obs. Sn.11 also does not contain `TKF`. We did not include the claimed `CRSF` feature around 10 keV during the fitting process and the best-fitting models on all the three observations does not contain an absorptive feature around 10 keV. Thus, our analysis indicates towards the result of Doroshenko et al. (2020) that the `CRSF` feature is not present.

The spectral parameters of the best-fitting models for all three observations of KS 1947+300 are given in Tables A1 and A2. The spectral fit for the time-averaged spectrum of Obs. Sn. 9 (having no `TKF/CRSF`) is shown in Fig. 5.

### 3.6 4U 1907+09

4U 1907+09 (X 1908+075) is a persistent HMXB pulsar with the NS accreting matter from the wind of an O-type Supergiant (Marshall & Ricketts 1980; Cox, Kaper & Mokiem 2005). The HMXB has a relatively short orbital period of about 8 d, and the pulsar has a spin period of about 437.5 s (Makishima et al. 1984). The fundamental

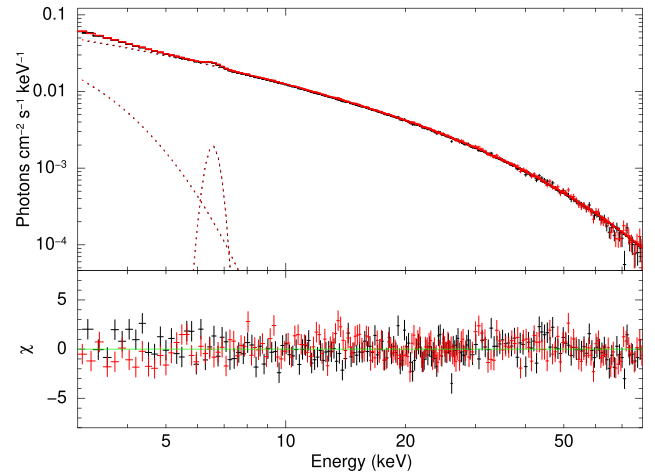


**Figure 5.** Spectral fit on KS 1947+300 Obs. Sn.9 using `mplcut` model having no `TKF/CRSF`. The top panel shows the best-fitting model and the bottom panel shows the residuals to the best-fitting model.

`CRSF` at 18 keV and its harmonic at 36 keV have been reported in the source (Cusumano et al. 2000).

We analysed the 3–45 keV spectrum from one *NuSTAR* observation Obs. Sn.12 (Table 2). Iron fluorescence line was present, which was fitted with a `Gaussian`. We used two `gabs` components centred at 18 and 36 keV respectively, to model the fundamental and harmonic `CRSF`, respectively.

All the training fits left absorption-like residuals between 5 and 10 keV. An absorptive feature around 8 keV has been reported by Tobrej et al. (2023). We, therefore, lowered the allowed range of `TKF` model centre between 6 and 9 keV. None of the best-fitting training models could fit the validation data set of Obs. Sn.12. Therefore, single-step fitting was performed skipping training. The best-fitting model on Obs. Sn.12 contain `TKF`, centred around 8 keV at a lower centre value than other cases.

The spectral parameters of the best-fitting models for Obs. Sn.12 of 4U 1907+09 are given in Tables A1 and A2. The spectral fit for the time-averaged spectrum of Obs. Sn.12 (having `TKF`) is shown in Fig. 6.

### 3.7 4U 1538–52

4U 1538–52 (4U 1538–522) is a bright, persistent eclipsing HMXB pulsar 6.6 kpc away, in which the NS accretes matter from the stellar wind of B-type Supergiant companion. The pulsar has a spin period of 526 s, and the binary has a relatively short orbital period of 3.73 d (see Hemphill et al. 2019; Malacaria et al. 2020; and references therein.). `CRSF` has been reported in the source spectrum at  $\sim 22$  keV and  $\sim 49$  keV (Hemphill et al. 2019).

We analysed the spectrum from one observation of the source Obs. Sn.13 (Table 2). The light curve indicated that this *NuSTAR* observation spans the ingress, eclipse, and egress phases of the binary. Therefore, we extracted two sets of spectra: (i) the time-averaged spectrum of the entire observation, and (ii) the spectrum of the out-of-eclipse phase ( $\sim 11$  ks of data covering ingress and egress phases).

Galactic absorption towards the source could not be constrained by the fit, therefore we fixed it to the Galactic value of  $7 \times 10^{21}$  atoms  $\text{cm}^{-2}$ . Iron line emission was fitted with a `Gaussian` model. `CRSF` at  $\sim 22$  keV was fitted a `gabs` model.

The best-fitting models on both the time-averaged and out-of-eclipse spectra do not contain `TKF`.

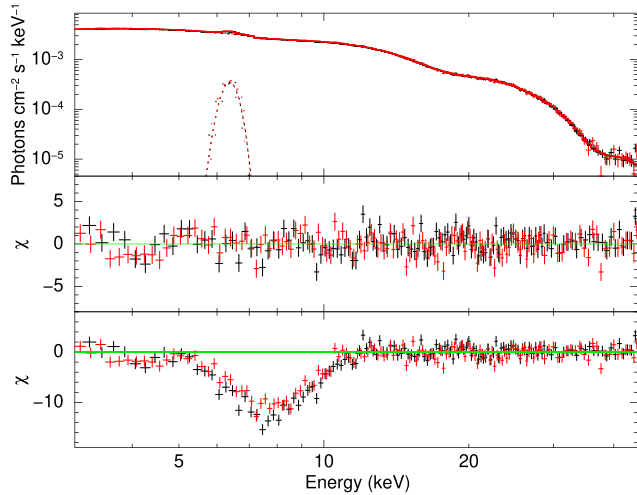


**Figure 6.** Spectral fit on 4U 1907+09 Obs. Sn.12 with `compTT` continuum model having *TKF*. The top panel shows the best-fitting model, the middle panel shows the residuals to the best-fitting model, and the bottom panel shows the residuals when the strength of the `gabs` component modelling *TKF* is set to 0.

The spectral parameters of the best-fitting models for Obs. Sn.13 of 4U 1538–52 are given in Tables A1 and A2. The spectral fit for the time-averaged spectrum of Obs. Sn. 13 (having no *TKF*) is shown in Fig. 7.

### 3.8 Cepheus X–4

Cep X–4 (GS 2138+56) is a transient HMXB pulsar with  $P_{\text{spin}} \sim 66.2$  s located 3.8 kpc away, in which the NS accretes from a B-type stellar companion in a 20 d binary orbit (see Bonnet-Bidaud & Mouchet 1998; Vybornov et al. 2017; and references therein.). CRSF has been found in the source at 30 keV (Mihara et al. 1991), and the asymmetric line profile of CRSF in the *NuSTAR* spectra was described with a combination of two Gaussian absorption model components centred at  $\sim 30$  and  $\sim 19$  keV, respectively (Fürst et al. 2015).

We analysed the 3–60 keV spectra from two observations Obs. Sn.14 and 15 (Table 2). Obs. Sn.14 probed the peak luminosity phase of the outburst of the source in 2014, while Obs. Sn.15 covered the luminosity decline phase of the same outburst. Iron line emission was fitted with a `Gaussian` model. The CRSF at  $\sim 22$  keV having an asymmetric profile was fitted with the combination of two `gabs` models (Bhargava et al. 2019).

The best-fitting models on both observations do not contain *TKF*.

The spectral parameters of the best-fitting models for both the observations of Cep X–4 are given in Tables A1 and A2. The spectral fit for the time-averaged spectrum of Obs. Sn. 14 (having no *TKF*) is shown in Fig. 8.

### 3.9 4U 1626–67

4U 1626–67 is a low mass ultracompact XRB pulsar hosting the NS having a spin period of 7 s (McClintock et al. 1977) and  $0.04 M_{\odot}$  companion star, with a short binary orbital period of about 42 min (Middleitch et al. 1981). CRSF has been reported in the spectrum at 37 keV (Orlandini et al. 1998b). Another peculiarity of the spectrum is the presence of low energy soft excess, which is usually modelled with a black-body component of  $kT \sim 0.6$  keV (see Kii et al. 1986).

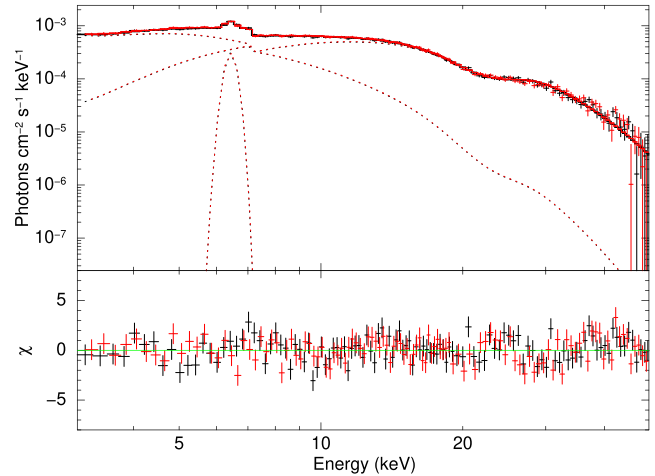


**Figure 7.** Spectral fit on time average spectrum of 4U 1538–52 Obs. Sn.13 covering the eclipse and out-of-eclipse phases, with `NPEX` continuum model, having no *TKF*. The top panel shows the best-fitting model and the bottom panel shows the residuals to the best-fitting model.

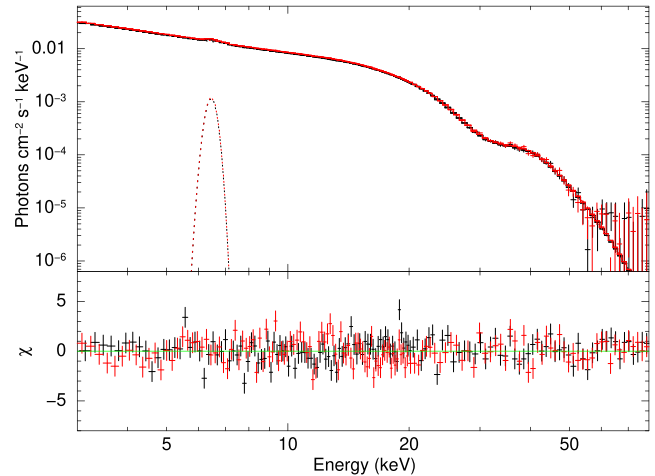


**Figure 8.** Spectral fit on Cep X–4 Obs. Sn.14 with `compTT` continuum model, having no *TKF*. The top panel shows the best-fitting model and the bottom panel shows the residuals to the best-fitting model.

We have analysed the spectrum from the observation Obs. Sn.16 (Table 2). The iron emission line was fitted with a `Gaussian` model. CRSF at around 37 keV was fitted with a `gabs` model.

None of the best-fitting training models could fit the validation data set of Obs. Sn.16. Therefore, single-step fitting was performed on Obs. Sn.16 skipping training. The best-fitting model on Obs. Sn.16 does not contain *TKF*.

The spectral parameters of the best-fitting models for Obs. Sn.16 of 4U 1626–67 are given in Tables A1 and A2. The spectral fit for the time-averaged spectrum of Obs. Sn.16 (having no *TKF*) is shown in Fig. 9.

### 3.10 SMC X–2

SMC X–2 (2S 0052–739) is a bright transient HMXB XRP in the Small Magellanic Cloud (SMC) dwarf galaxy, located 65 kpc away (Li, Jernigan & Clark 1977). The binary hosts the pulsar having spin period  $\sim 2.37$  s (Corbet et al. 2001) and an O-type stellar companion (Crampton, Hutchings & Cowley 1978) in a 28.6 d orbit (Schurch,

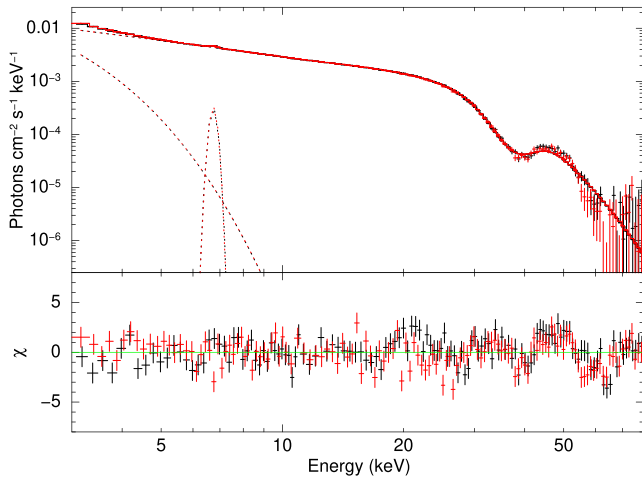


**Figure 9.** Spectral fit with `FDcut` model on 4U 1626–67 Obs. Sn.16, having no *TKF*. The top panel shows the best-fitting model and the bottom panel shows the residuals to the best-fitting model.

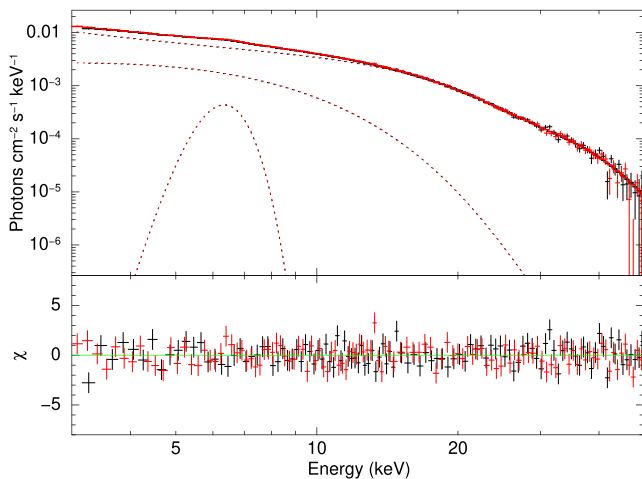


**Figure 10.** Spectral fit on SMC X–2 Obs Sn.17 with `compTT` continuum model, having no *TKF*. The top panel shows the best-fitting model and the bottom panel shows the residuals to the best-fitting model.

Udalski & Coe 2008). The X-ray spectrum is generally modelled with an absorbed power-law continuum modified by CRSF centred at  $\sim 27$  keV (Jaisawal & Naik 2016).

We analysed the spectrum from three observations Obs. Sn. 17, 18, and 19 (Table 2) that probed the outburst of the source in 2015. Iron fluorescence line was present, which was fitted with a `Gaussian`. CRSF at  $\sim 27$  keV was fitted with a `gabs`. The width of CRSF was not constrained by the fit in Obs. Sn.19, it was thus fixed to the average width obtained from other observations.

The best-fitting models of all three observations did not require *TKF*.

The spectral parameters of the best-fitting models for Obs. Sn.17, 18, and 19 of SMC X–2 are given in Tables A1 and A2. The spectral fit for Obs. Sn.17 (having no *TKF*) is shown in Fig. 10.

### 3.11 IGR J17544–2619

IGR J17544–2619 is a supergiant fast X-ray transient located 4 kpc away (See Rampy, Smith & Negueruela 2009, and references therein) in which, the NS in an HMXB accretes from the wind of an O-type

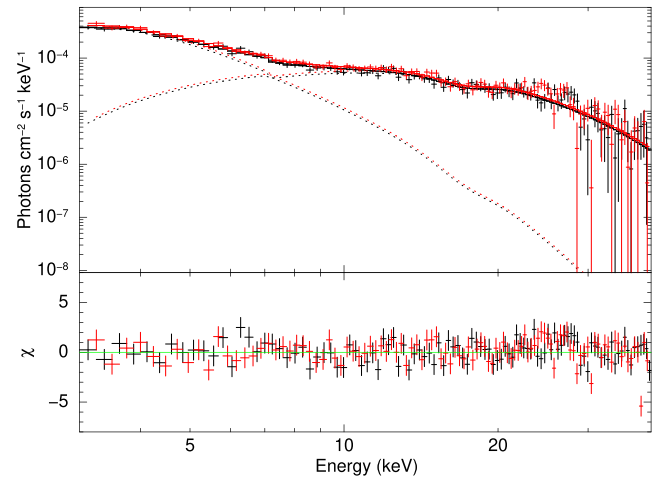


**Figure 11.** Spectral fit on IGR J17544–2619 Obs Sn.20 with `NPEX` continuum model having no *TKF*. The top panel shows the best-fitting model and the bottom panel shows the residuals to the best-fitting model.

supergiant companion. The binary has an orbital period of 5 d (Clark et al. 2009), and the NS has an (unconfirmed) spin period of 71.5 s (Drave et al. 2012 and Drave et al. 2014). The spectrum is usually modelled with a combination of low energy thermal black-body component and a high-energy non-thermal Comptonization component, modified by fundamental CRSF at 17 keV and its harmonic at 30 keV (Bhalerao et al. 2015).

We analysed the 3–40 keV spectrum from Obs. Sn.20 (Table 2). The spectrum was dominated by background photons above 40 keV. CRSF present at  $\sim 18$  keV was modelled with a `gabs`.

The best-fitting model on Obs. Sn.20 does not contain *TKF*.

The spectral parameters of the best-fitting models for Obs. Sn.20 of IGR J17544–2619 are given in Tables A1 and A2. The spectral fit for Obs. Sn.20 (having no *TKF*) is shown in Fig. 11.

### 3.12 IGR J16393–4643

IGR J16393–4643 is an HMXB pulsar in which the NS accretes from the wind of a stellar companion of an unknown spectral class. The pulsar has a spin period of 911 s, and the binary has an orbital period of  $\sim 3.7$  d (see Thompson et al. 2006, and references therein). It shows an unusual partial eclipse (Islam et al. 2015) which has also been interpreted to be the absorption of X-rays in the stellar corona with a grazing line of sight to the source (Kabiraj, Islam & Paul 2019). Galactic ISM heavily obscures photons from the source and the broad-band spectrum is usually modelled with a heavily absorbed power-law continuum modified by CRSF at 30 keV (Bodaghee et al. 2016).

We analysed the 3–50 keV spectrum from Obs. Sn.21 (Table 2). The pointed observation is contaminated by stray light from a nearby source GX 340+0, but we have taken care of this during the selection of the source region. Galactic absorption towards the source could not be constrained by the fit, therefore we fixed it to the Galactic value of  $2.15 \times 10^{21}$  atoms  $\text{cm}^{-2}$ . CRSF present at  $\sim 30$  keV was modelled with a `gabs`.

The best-fitting model on Obs. Sn.21 contain *TKF*.

The spectral parameters of the best-fitting models for Obs. Sn.21 of IGR J16393–4643 are given in Tables A1 and A2. The spectral fit for Obs. Sn.21 (having *TKF*) is shown in Fig. 12.

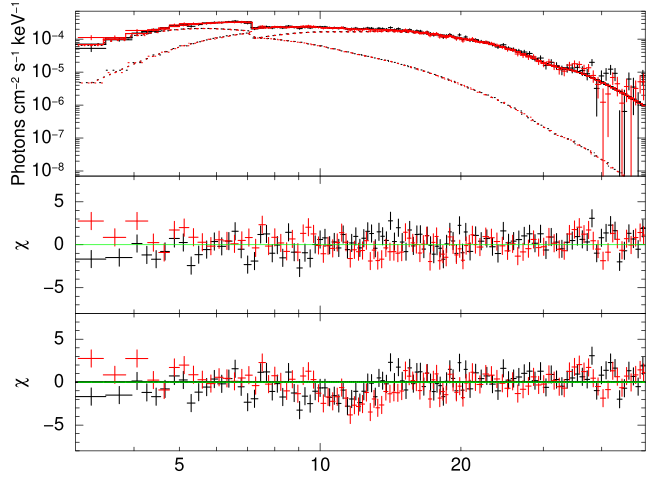


**Figure 12.** Spectral fit on IGR J16393–4643 Obs. Sn.21 with *NPEX* continuum model having *TKF*. The top panel shows the best-fitting model, the middle panel shows the residuals to the best-fitting model, and the bottom panel shows the residuals when the strength of the *gabs* component modelling *TKF* is set to 0.

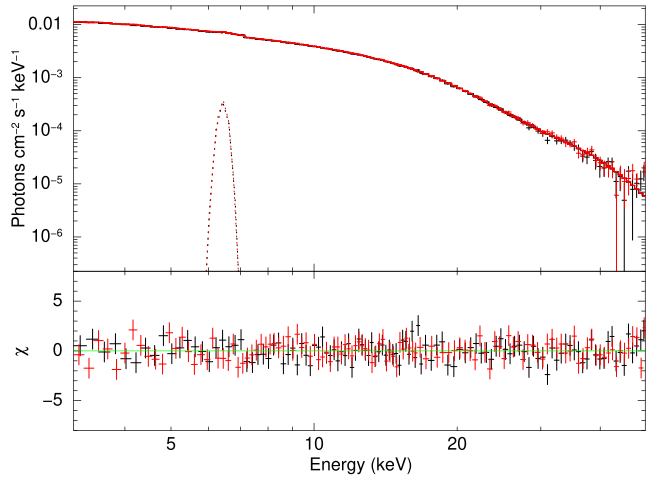


**Figure 13.** Spectral fit on 2S 1553–542 Obs. Sn.22 with *FDcut* continuum model having no *TKF*. The top panel shows the best-fitting model and the bottom panel shows the residuals to the best-fitting model.

### 3.13 2S 1553–542

2S 1553–542 is a transient HMXB pulsar located at a distance of  $20 \pm 4$  kpc on the far-side arms of Milky way (Tsygankov et al. 2016 and Lutovinov et al. 2016). It consists of a NS with a spin period of 9.3 s accreting from a Be-type companion star in a 31 d binary orbit (see Kelley, Rappaport & Ayasli 1983, and references therein). CRSF has been reported in the source at  $\sim 24$  keV (Tsygankov et al. 2016).

We analysed the 3–50 keV spectrum from Obs. Sn. 22 (Table 2). Iron line emission was fitted with a *Gaussian* model. CRSF at  $\sim 28$  keV was fitted with *gabs*.

Since a high energy cutoff was present below 15 keV, the models containing a high energy cutoff were also included while fitting the training data set. The best-fitting model on Obs. Sn. 22 does not require *TKF*.

The spectral parameters of the best-fitting models for Obs. Sn.22 of 2S 1553–542 are given in Tables A1 and A2. The spectral fit for Obs. Sn.22 (having no *TKF*) is shown in Fig. 13.

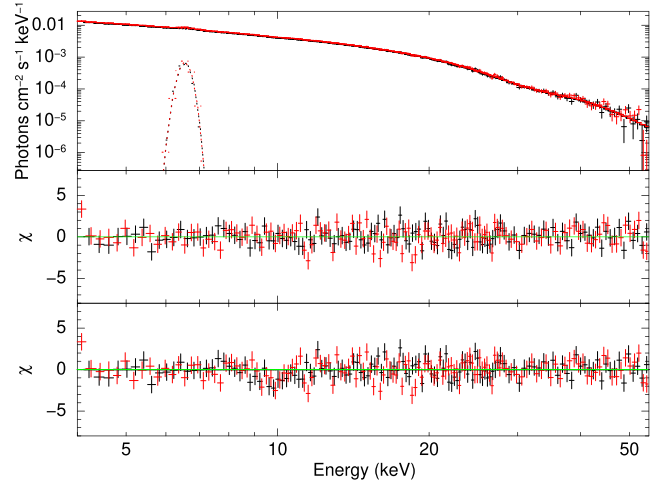


**Figure 14.** Spectral fit on RX J0520.5–6932 Obs. Sn.23 with *cutoffpl* continuum model having *TKF*. The top panel shows the best-fitting model, the middle panel shows the residuals to the best-fitting model, and the bottom panel shows the residuals when the strength of the *gabs* component modelling *TKF* is set to 0.

### 3.14 RX J0520.5–6932

RX J0520.5–6932 is a transient XRP in the Large Magellanic Cloud (LMC) (Schmidtke et al. 1996). The HMXB hosts the NS with spin period of  $\sim 8$  s (Vasilopoulos et al. 2014) in a 24.4 d orbit around a Be-type companion star (see Coe et al. 2001; Kuehnel et al. 2014; and references therein). CRSF has been reported in the spectrum at 31 keV (Tendulkar et al. 2014).

We analysed the spectrum from two observations Obs. Sn.23 and 24 (Table 2). The spectra are background-dominated above 55 keV in both observations. Also, FPMA and FPMB spectra showed cross-calibration anomalies in 3–4 keV for Obs. Sn.23. Hence we analysed the 3–55 keV spectrum of Obs. Sn.23 and 4–55 keV spectrum of Obs. Sn.24. Galactic absorption towards the source could not be constrained by the fit, therefore we fixed it to the Galactic value of  $2 \times 10^{21}$  atoms  $\text{cm}^{-2}$ . Iron emission line was fitted with a *Gaussian*. CRSF at  $\sim 30$  keV was fitted with a *gabs*.

The best-fitting models on both observations contain *TKF*.

The spectral parameters of the best-fitting models for Obs. Sn.23 and 24 of RX J0520.5–6932 are given in Tables A1 and A2. The spectral fit for Obs. Sn.23 (having *TKF*) is shown in Fig. 14.

### 3.15 Cen X–3

Cen X–3 is a bright and persistent HMXB pulsar that hosts a NS that accretes from the wind of an O-type companion star. The binary has an orbital period of about 2.1 d (Schreier et al. 1972), and the NS has a spin period of 4.8 s (Giacconi et al. 1971). CRSF is present in the source at 30 keV (see Tomar et al. 2021, and references therein).

We analysed the 3–60 keV *NuSTAR* spectrum from Obs. Sn.25 (Table 2). Iron emission line was fitted with a *Gaussian*. CRSF present at  $\sim 30$  keV was fitted with a *gabs*.

Since a high energy cutoff was present below 15 keV, the models containing a high energy cutoff were also included while fitting the training data set. None of the best-fitting training models could fit the validation data set of Obs. Sn.25. Therefore, single-step fitting was performed skipping training. The best-fitting model on Obs. Sn.25 contain *TKF*.

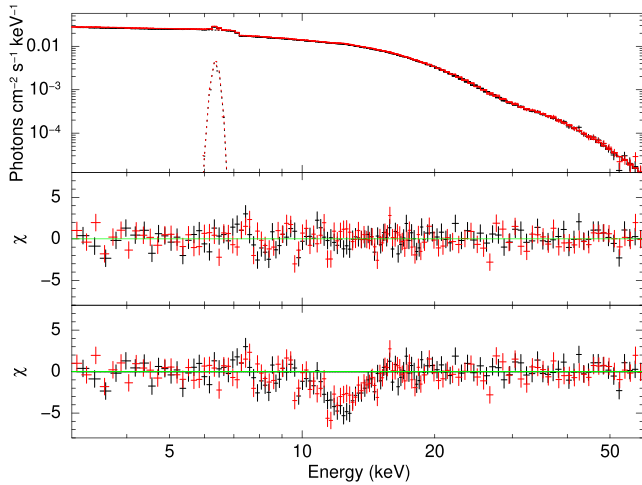


**Figure 15.** Spectral fit with `mplcut` model on Cen X-3 Obs. Sn.25, having *TKF*. The top panel shows the best-fitting model, the middle panel shows the residuals to the best-fitting model, and the bottom panel shows the residuals when the strength of the `gabs` component modelling *TKF* is set to 0.

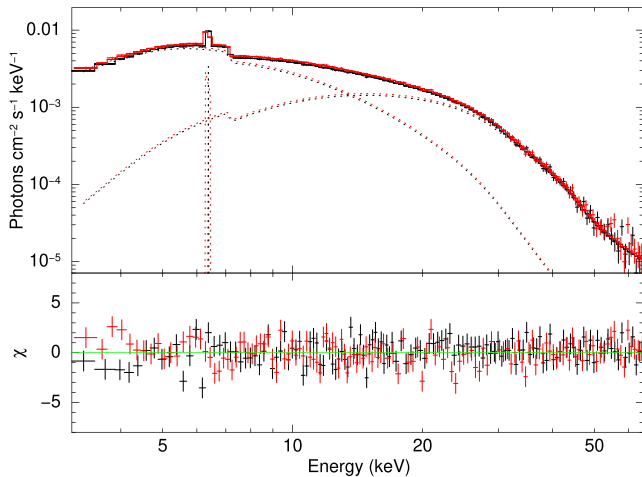


**Figure 16.** Spectral fit using `mplcut` model on GX 301-2 Obs. Sn.26, having no *TKF*. The top panel shows the best-fitting model and the bottom panel shows the residuals to the best-fitting model.

The spectral parameters of the best-fitting models for Obs. Sn.25 of Cen X-3 are given in Tables A1 and A2. The spectral fit for Obs. Sn.25 (having *TKF*) is shown in Fig. 15.

### 3.16 GX 301-2

GX 301-2 is a bright HMXB pulsar located  $\sim 4$  kpc away, hosting a NS accreting from the wind of a hypergiant  $35 M_{\odot}$  donor star. The pulsar has a relatively long spin period of  $\sim 680$  s, and the binary has an eccentric orbit with an orbital period of 41 d which is manifested as periodic flares during the periastron passage of the NS (see Doroshenko et al. 2010, and references therein). Its broad-band spectrum is usually modelled by a power-law continuum modified by two distinct CRSFs at 35 and 55 keV (see Nabizadeh et al. 2019, and references therein).

We analysed the 3–65 keV spectra from two observations Obs. Sn.26 and 27, respectively, in Table 2. Obs. Sn.27 contains a flare, and therefore we analysed time-averaged, flare and out-of-flare spectra

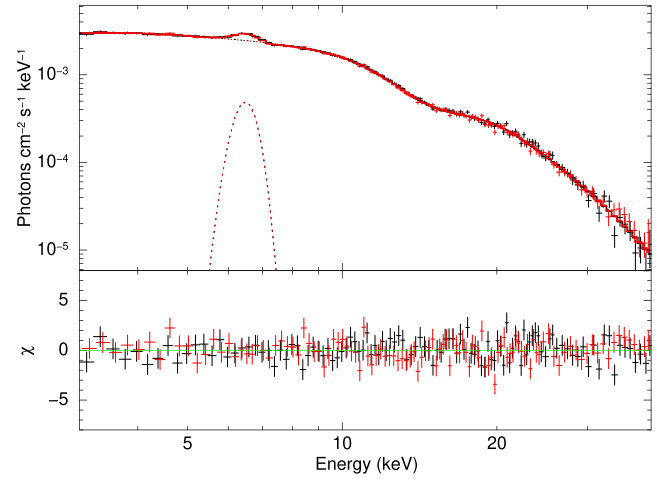


**Figure 17.** Spectral fit using `newhcut` model on XTE J1829-098 Obs. Sn. 28 having no *TKF*. The top panel shows the best-fitting model and the bottom panel shows the residuals to the best-fitting model.

separately. Iron fluorescence line was present in all the spectra, which were fitted with a `Gaussian`. The width of the iron emission line was not constrained by the fit in the out-of-flare-state spectrum of Obs. Sn.38 and we fixed it to 10 eV. Two CRSFs were present at  $\sim 30$  and  $\sim 50$  keV, and those were fitted with two `gabs`. The width of CRSF at 50 keV could be constrained in Obs. Sn.27 out-of-flare state and the flaring state spectrum of Obs. Sn.27. Therefore, it was frozen to the CRSF width obtained from time-averaged spectrum of Obs. Sn.27.

The best-fitting models on none of the spectra contain *TKF*.

The spectral parameters of the best-fitting models for Obs. Sn.26 and 27 of GX 301-2 are given in Tables A1 and A2. The spectral fit for Obs. Sn.26 (having no *TKF*) is shown in Fig. 16.

### 3.17 XTE J1829-098

XTE J1829-098 is a transient XRP having a spin period of 7.8 s. Even though the nature of the binary is considered an HMXB based on the observed hard spectrum, the classification of the companion is still uncertain. Assuming an O- or B-type nature to the companion, Halpern & Gotthelf (2007) estimated the distance to the binary as 10 kpc. The binary orbital period is considered to be the outburst recurrence interval of  $\sim 246$  d. Its broad-band spectrum is usually modelled with a power-law continuum, and a CRSF was reported at  $\sim 15$  keV (see Shtykovsky et al. 2019, and references therein).

We analysed the 3–40 keV *NuSTAR* spectrum of the source (Obs. Sn.28 in Table 2) that probed an outburst of the source in 2018. The ISM absorption column density could be constrained by the fit, and the iron fluorescence line was fitted with a `Gaussian`. CRSF present at  $\sim 15$  keV was fitted with a `gabs` model. The cutoff energy of the best-fitting power law with high energy cutoff models is close to  $\sim 10$  keV. Moreover, the CRSF present at  $\sim 15$  keV would impact the *TKF* estimation. Therefore we performed direct validation to find the best-fitting model without *TKF*.

The spectral parameters of the best-fitting models for Obs. Sn.28 of XTE J1829-098 are given in Tables A1 and A2. The spectral fit for Obs. Sn.28 (having no *TKF*) is shown in Fig. 17.

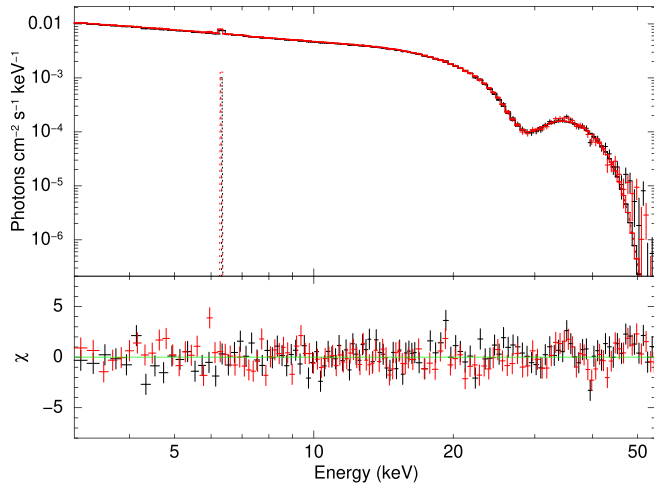


**Figure 18.** Spectral fit on V 0332+53 Obs. Sn.30 with `newhcut` continuum model having no *TKF*. The top panel shows the best-fitting model and the bottom panel shows the residuals to the best-fitting model.

### 3.18 V 0332+63

V 0332+53 is a bright transient HMXB pulsar located 7 kpc away hosting an O-type stellar companion and the NS having a spin period of 4.4 s. The binary has an eccentric orbit with an orbital period of 34 d. This is one of the few pulsars that exhibit multiple harmonics of the CRSF in the spectrum. The spectrum is usually modelled by a power-law continuum modified by a CRSF at 28 keV and its two harmonics at 49 and 72 keV, respectively (see Tsygankov et al. 2006, and references therein).

We analysed the 3–55 keV spectrum from the four observations Obs. Sn.29, 30, 31, and 32 (Table 2). Iron fluorescence line was present in all the spectra, which were fitted with a `Gaussian`. The width of the iron emission line was not constrained by the fits and we fixed it to 10 eV. CRSF at  $\sim 28$  keV and its first harmonic at  $\sim 56$  keV was fitted with `cyclabs`. We also tried using `gabs` to fit the CRSF, but it left residuals at high energies. The width of harmonic CRSF could not be constrained in the best-fitting models on Obs. Sn.29 and 30 containing *TKF*. Therefore, it was fixed to the CRSF width obtained from the best-fitting models on Obs. Sn.29 and 30 that does not contain *TKF*.

The best-fitting models on Obs. Sn.29 and 32 do not contain *TKF*. Even though the best-fitting model Obs. Sn.30 and 31 contain *TKF*, there also exist similar well-fitting models in which *TKF* is absent.

The spectral parameters of the best-fitting models for all four observations of V 0332+63 are given in Tables A1 and A2. The spectral fit for Obs. Sn.30 (having no *TKF*) is shown in Fig. 18.

### 3.19 XTE J1858+034

XTE J1858+034 is a transient Be-XRP with spin period  $\sim 221$  s located  $\sim 10$  kpc away. The regular outburst period of  $\sim 380$  s is considered as the orbital period of the binary. The broad-band spectrum is generally modelled by a power-law continuum with a cutoff at high energy, modified by iron fluorescence line at 6.5 keV and CRSF at  $\sim 48$  keV (see Malacaria et al. 2021, and references therein).

We analysed the 5–55 keV spectrum of the source. The spectrum is background-dominated above 55 keV, and the FPMA/FPMB spectra below 5 keV showed cross-calibration anomalies. Iron fluorescence

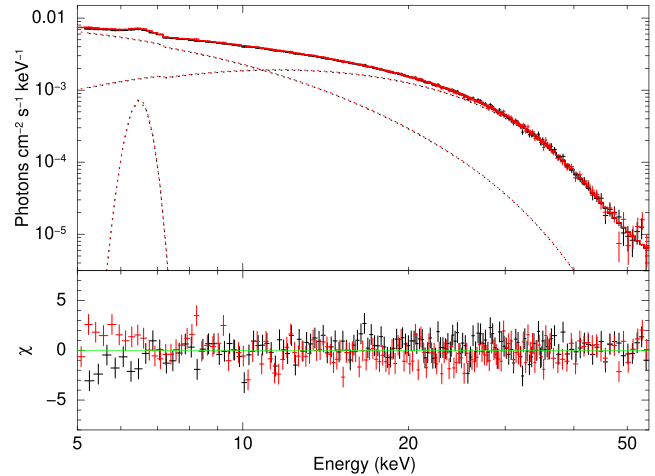


**Figure 19.** Spectral fit using `NPEX` continuum model on XTE J1858+034 Obs. Sn.33 having no *TKF*. The top panel shows the best-fitting model and the bottom panel shows the residuals to the best-fitting model.

line was present, which was fitted with a `Gaussian`. CRSF centred around 50 keV was fitted with `gabs`.

The best-fitting models on Obs. Sn.33 does not contain *TKF*.

The spectral parameters of the best-fitting models for Obs. Sn.33 of XTE J1858+034 are given in Tables A1 and A2. The spectral fit for Obs. Sn.33 (having no *TKF*) is shown in Fig. 19.

### 3.20 4U 1700–37

4U 1700–37 is a transient HMXB in which a NS accretes from the wind of a supergiant O-type star in a 3.5 d binary orbit. Even though coherent pulsations were reported at 67 s from Tenma observation during a flare, none of the other observatories has detected pulsations in the subsequent observations. The spectrum of 4U 1700–37 is usually modelled with power-law continuum models, and CRSF has been reported at two different energies of 16 keV (Bala et al. 2020a) and 37 keV (Reynolds et al. 1999).

Obs. Sn.34 (Table 2) contains a flare as evident from the light curve. We, therefore, analysed the 3–79 keV *NuSTAR* time-averaged, flare and out-of-flare spectra from Obs. Sn.34. Galactic absorption towards the source could not be constrained by the fit, therefore we fixed it to the Galactic value of  $5 \times 10^{21}$  atoms  $\text{cm}^{-2}$ . Iron fluorescence line was present, which is fitted with a `Gaussian`. The width of the iron emission line was not constrained by the fit and we fixed it to 10 eV. CRSF at  $\sim 16$  keV was fitted with a `gabs` model. The width of CRSF was not constrained by the fit in the flaring state spectrum, it was thus fixed to the width obtained from the time-averaged spectrum.

The best-fitting models on the time-averaged, flaring state, and out-of-flare state spectrum of Obs. Sn.34 contains *TKF*.

The spectral parameters of the best-fitting models for Obs. Sn.34 of 4U 1700–37 are given in Tables A1 and A2. The spectral fit for Obs. Sn.34 (having *TKF*) is shown in Fig. 20.

### 3.21 LMC X–4

LMC X–4 is a persistent flaring HMXB pulsar ( $P_{\text{spin}} \sim 13.5$  s) located  $\sim 50$  kpc away in the LMC satellite galaxy, hosting a NS pulsar that accretes from the disc-fed matter of an O-type companion star in a 1.4 d orbit. The spectrum of LMC X–4 is usually fitted with power-law continuum models with fluorescence lines of iron (Levine et al. 1991).

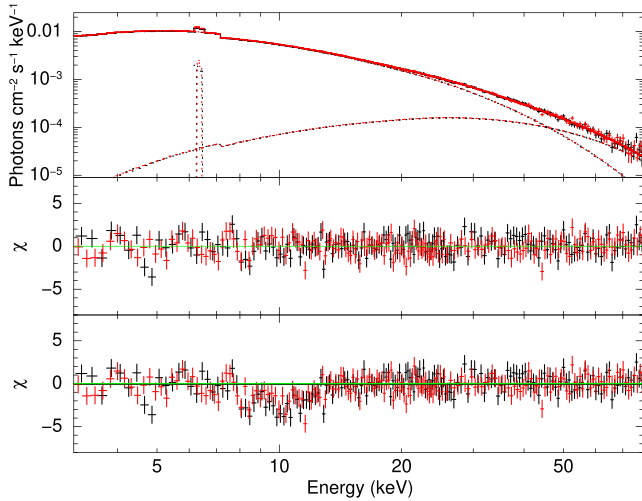


**Figure 20.** Spectral fit using NPEX continuum model on 4U 1700–37 Obs. Sn.34 time-averaged spectrum having *TKF*. The top panel shows the best-fitting model, the middle panel shows the residuals to the best-fitting model, and the bottom panel shows the residuals when the strength of the *gabs* component modelling *TKF* is set to 0.

We analysed spectra from four *NuSTAR* observations Obs. Sn.35, 36, 37, and 38 (Table 2). Obs. Sn.35 and 38 have flares in the light curves, and therefore the time-averaged, and the separated flare and the separated flare and out-of-flare spectra were independently analysed. Galactic absorption towards the source could not be constrained by the fit, therefore we fixed it to the Galactic value of  $8 \times 10^{20}$  atoms  $\text{cm}^{-2}$ . Iron fluorescence line was present in all the spectra, which were fitted with a *Gaussian*. The width of the iron emission line was not constrained by the fit in the out-of-flare-state spectrum of Obs. Sn.38 and we fixed it to 10 eV.

The best-fitting models on the time-averaged and flaring-state spectrum of Obs. Sn.35, and time-averaged spectrum of Obs. Sn.38 contain *TKF*. The best-fitting model on the out-of-flare-state spectrum of Obs. Sn.38 does not contain *TKF*. Even though the best-fitting models on the out-of-flare-state spectrum of Obs. Sn.35, the flaring-state spectrum of Obs. Sn.38 and time-averaged spectra of Obs. Sn.36 and 37 contain *TKF*, there also exist similar well-fitting models in which *TKF* is absent.

The spectral parameters of the best-fitting models for all four observations of LMC X–4 are given in Tables A1 and A2. The spectral fit for the time-averaged spectrum of Obs. Sn.35 (having *TKF*) and out-of-flare-state spectrum of Obs. Sn.35 (having no *TKF*) are shown in Fig. 21.

### 3.22 IGR J17329-2731

IGR J17329-2731 is a transient XRP in a symbiotic X-ray binary hosting the slow spinning  $\sim 6680$  s pulsar accreting from the wind of a late M-type giant stellar companion. The source is estimated to be at a distance of 2.7 kpc. The broad-band spectrum is modelled with a power-law continuum modified by CRSF at  $\sim 21$  keV and iron fluorescence lines (Bozzo et al. 2018).

We analysed the 3–55 keV spectrum from the observation Obs. Sn.39 (Table 2). Galactic absorption towards the source could not be constrained by the fit, therefore we fixed it to the Galactic value of  $3 \times 10^{21}$  atoms  $\text{cm}^{-2}$ . Iron fluorescence line was present, which is fitted with a *Gaussian*. The width of the iron emission line was

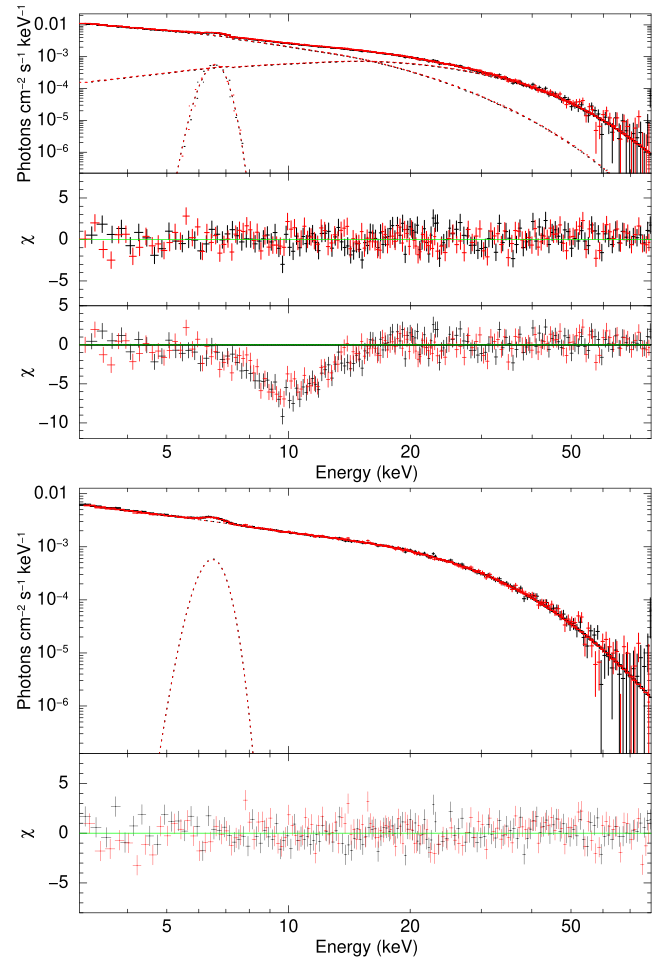


**Figure 21.** Top: Spectral fit on LMC X–4 Obs. Sn.35 time-averaged spectrum, with NPEX continuum model, having *TKF*. The top panel shows the best-fitting model, the middle panel shows the residuals to the best-fitting model, and the bottom panel shows the residuals when the strength of the *gabs* component modelling *TKF* is set to 0. Bottom: Spectral fit on LMC X–4 Obs. Sn.35 out-of-flare state spectrum with *FDCut* continuum model, having no *TKF*. The top panel shows the best-fitting model and the bottom panel shows the residuals to the best-fitting model.

not constrained by the fit and we fixed it to 10 eV. CRSF at  $\sim 22$  keV was fitted with a *gabs* model.

The best-fitting models on Obs. Sn.39 does not contain *TKF*.

The spectral parameters of the best-fitting models for Obs. Sn.39 of IGR J17329-2731 are given in Tables A1 and A2. The spectral fit for Obs. Sn.39 (having no *TKF*) is shown in Fig. 22.

### 3.23 SMC X–1

SMC X–1 is an HMXB pulsar in the SMC located  $\sim 61$  kpc away. This eclipsing binary consists of a  $\sim 0.7$  s NS pulsar in  $\sim 3.89$  d orbit around a B-type supergiant companion star and is one of the few HMXBs that accrete via Roche lobe overflow. The broad-band spectrum is usually modelled by absorbed power-law models and iron fluorescence line (see Pike et al. 2019, and references therein).

We analysed the spectra of SMC X–1 from four *NuSTAR* observations Obs. Sn.40, 41, 42, and 43 (Table 2). Galactic absorption towards the source could not be constrained by the fit, therefore we fixed it to the Galactic value of  $5 \times 10^{21}$  atoms  $\text{cm}^{-2}$ . Iron fluorescence line was present, which is fitted with a *Gaussian*.

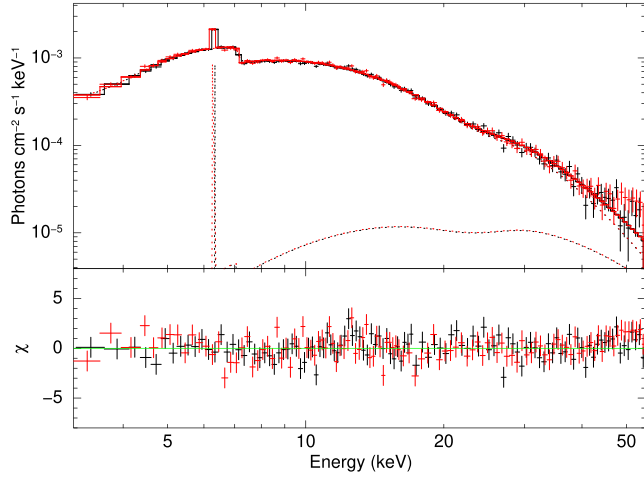


**Figure 22.** Spectral fit on IGR J17329-2731 Obs. Sn.39 using NPEX continuum model, having no *TKF*. The top panel shows the best-fitting model and the bottom panel shows the residuals to the best-fitting model.

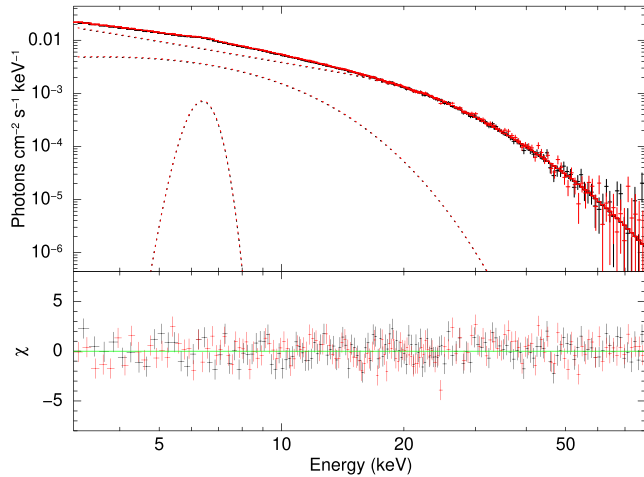


**Figure 23.** Spectral fit performed on SMC X-1 Obs. Sn.40 using `mplcut` continuum model, having no *TKF*. The top panel shows the best-fitting model and the bottom panel shows the residuals to the best-fitting model.

The best-fitting models on Obs. Sn.40, 41, and 42 do not contain *TKF*. Even though the best-fitting models on Obs. Sn.43 contain *TKF* there also exists a similar well-fitting model in which *TKF* is absent.

The spectral parameters of the best-fitting models for all four observations of SMC X-1 are given in Tables A1 and A2. The spectral fit for the time-averaged spectrum of Obs. Sn.40 (having no *TKF*) is shown in Fig. 23.

### 3.24 GRO J1008-57

GRO J1008-57 is a transient HMXB pulsar located  $\sim 5$  kpc away, hosting a  $\sim 94$  s pulsar and a Be-type stellar companion. The source shows regular outbursts at a period of  $\sim 249$  d, interpreted as the binary orbital period. The spectrum is usually modelled with power-law continuum modified by CRSF at  $\sim 78$  keV (see Kühnel et al. 2013; Bellm et al. 2014 and references therein).

We analysed the 3–79 keV *NuSTAR* spectrum from Obs. Sn.44. Galactic absorption towards the source could be constrained by the fit. Iron fluorescence line was present, but fitting it with a `Gaussian` line left residuals in the iron region. This could be attributed to im-

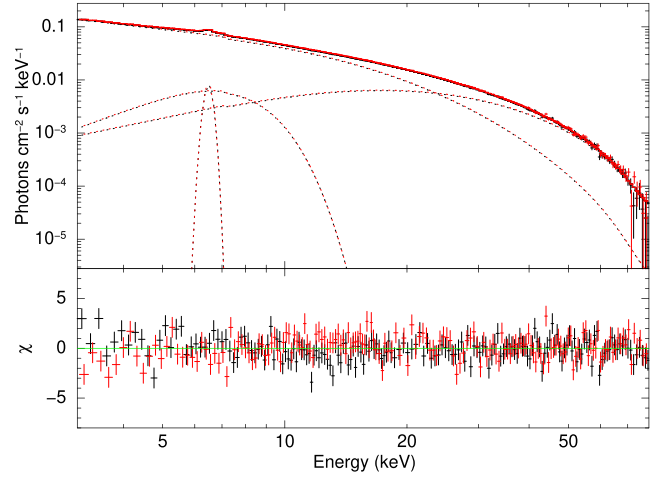


**Figure 24.** Figure showing spectral fit using NPEX continuum model on GRO J1008-57 Obs. Sn.44, having no *TKF*. The top panel shows the best-fitting model and the bottom panel shows the residuals to the best-fitting model.

proper modelling of the complex iron fluorescence emission region, as the presence of lines at 6.4, 6.6, and 7 keV have been reported in the *Suzaku* observations in Yamamoto et al. (2014). Therefore, we used a combination of two `Gaussian` models to fit the complex iron region (similar to Section 3.2). The cyclotron line parameters could not be constrained by the fit, therefore we froze the CRSF line energy to the best-fitting value obtained by Bellm et al. (2014) from simultaneous *Suzaku*-HXD (20–100 keV) and *NuSTAR* (3–79 keV) spectra.

None of the best-fitting training models could fit the validation data sets in Obs. Sn.44. Therefore, single-step fitting was performed on Obs. Sn.44, skipping training. The best-fitting model on Obs. Sn.44 does not contain *TKF*.

The spectral parameters of the best-fitting models for Obs. Sn.44 of GRO J1008-57 are given in Tables A1 and A2. The spectral fit for Obs. Sn.44 (having no *TKF*) is shown in Fig. 24.

### 3.25 GX 304-1

GX 304-1 is a transient Be-XRP located  $\sim 2$  kpc away that hosts the  $\sim 272$  s pulsar and Be-type companion star in a long  $\sim 133$  d orbit. It exhibits regular Type-I outbursts during its periastron passage. The luminosity of the source varies over a wide range spanning several orders of magnitude like other Be-XRPs. CRSF has been detected in the high luminosity outburst-state spectrum at  $\sim 54$  keV, which was modelled with a power-law continuum model (Yamamoto et al. 2011). The low luminosity spectrum is modelled by a two-component Comptonization model (Tsygankov et al. 2019a).

We analysed the 3–25 keV *NuSTAR* spectrum from Obs. Sn.45, during which the source was in a low-luminosity state. The spectrum is dominated by background photons above 25 keV. This observation has poor photon statistics, with an average count rate of  $\sim 0.21$  counts  $s^{-1}$  and a total exposure of  $\sim 58$  ks (see Table 2). Therefore we rebinned the spectrum such that it has a minimum of 1 count per energy bin and have used Cash-statistic (`cstat` in `XSPEC`) as the fit statistic for analysing this *NuSTAR* observation.

We found that some of the model combinations given in Section 3.1 could fit the training and validation sets. However, as discussed in Tsygankov et al. (2019a), the spectrum of GX 304-1 shows a transition from single power law to double power law, when the source luminosity drops by  $\sim 2$  orders of magnitude. We found that



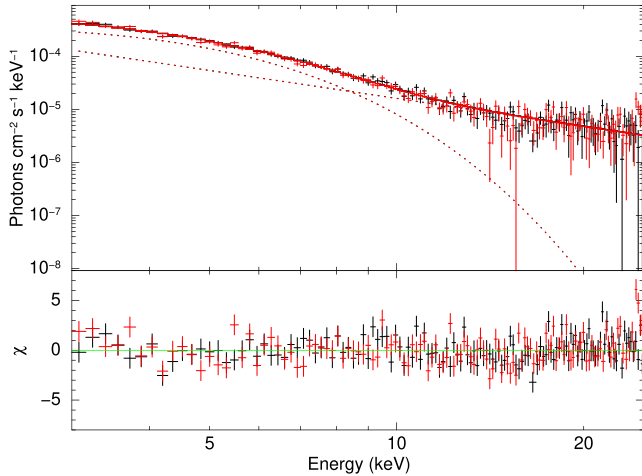


**Figure 25.** Spectral fit using `NPEX` continuum model performed on GX 304–1 Obs. Sn.45, having no *TKF*. The top panel shows the best-fitting model and the bottom panel shows the residuals to the best-fitting model.

double power-law models could also fit the spectrum. The best-fitting model on Obs. Sn.45 does not contain *TKF*.

The spectral parameters of the best-fitting models for Obs. Sn.45 of GX 304–1 are given in Tables A1 and A2. The spectral fit for Obs. Sn.45 (having no *TKF*) is shown in Fig. 25.

### 3.26 1A 0535+26

1A 0535+26 is a transient HMXB pulsar located 2 kpc away that hosts the pulsar spinning with a period of 104 s in an eccentric and long 110 d orbit around the Be-type stellar companion. It exhibits regular Type-I outbursts during the periastron passages and Type-II outbursts due to companion stellar activity. It is known to exhibit long quiescent states as well (see Ballhausen et al. 2017, and references therein), and the source flux, therefore, spans several orders of magnitude. The source spectrum shows fundamental CRSF at about 45 keV and first harmonic at about 100 keV (see Sartore et al. 2015, and references therein). The high luminosity level spectra are usually modelled with power-law continuum models (Mandal & Pal 2022) while the low luminosity spectra are modelled with a two-component Comptonization model (Tsygankov et al. 2019b).

We analysed spectra from three *NuSTAR* observations of the source, Obs. Sn.46, 47, and 48 (Table 2). Obs. Sn. 47 and 48 were dominated by background photons above 50 keV. Galactic absorption towards the source could not be constrained by the fit in Obs. Sn.48, therefore we fixed it to the Galactic value of  $4 \times 10^{21}$  atoms  $\text{cm}^{-2}$ . Iron fluorescence line was present in Obs. Sn.46 and 47, which were fitted with a `Gaussian`. CRSF at  $\sim 45$  keV was fitted with a `gabs` model in Obs. 46 and 48, and it was not required in Obs. Sn.47. The width of CRSF could not be constrained by the fit in Obs. Sn.48, therefore it was fixed to the best-fitting value obtained from Obs. Sn.46.

The best-fitting models on Obs. Sn.49 and 50 contain *TKF*. All the models that could fit Obs. Sn.48 by training/validation gave systematic wavy residuals in 3–20 keV, regardless of the best-fitting models having no *TKF*. Therefore, Obs. Sn.48 was fitted manually with a two-component `CompTT` model (see Tsygankov et al. 2019b), and it does not contain *TKF*.

The spectral parameters of the best-fitting models for all three observations of 1A 0535+26 are given in Tables A1 and A2. The

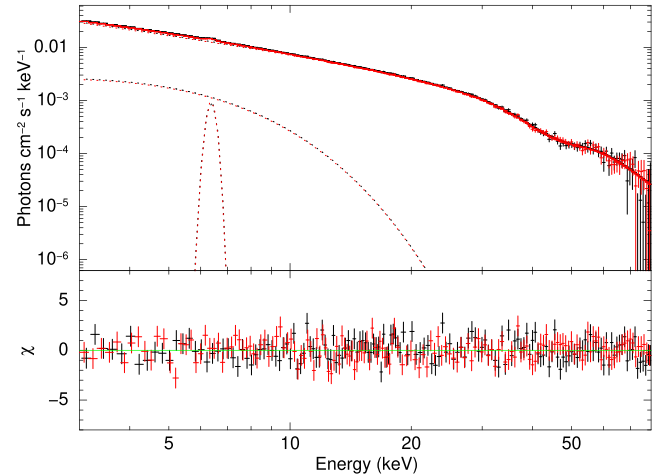


**Figure 26.** Spectral fit using `FDCUT` continuum model performed on 1A 0535+26 Obs. Sn.46, having no *TKF*. The top panel shows the best-fitting model and the bottom panel shows the residuals to the best-fitting model.

spectral fit for the time-averaged spectrum of Obs. Sn.46 (having no *TKF*) is shown in Fig. 26.

### 3.27 GRO J2058+42

GRO J2058+42 is a bright transient HMXB pulsar with  $P_{\text{spin}} \sim 198$  s located 9 kpc away, hosting the pulsar and a Be-type companion star (Wilson et al. 2005). The binary orbital period of this system is ambiguous due to the ambiguity in the perceived intensity levels of successive outbursts. An outburst interval of 55 d is interpreted as the orbital period when each outburst is assumed to be occurring due to the periastron passage, or 110 d if the successive outbursts are distinguishable, with one from the apastron and the next from the periastron. Molkov et al. (2019) reported the presence of CRSF at  $\sim 10$  keV and two of its harmonics at  $\sim 20$  and  $\sim 30$  keV in the *NuSTAR* spectrum in a narrow spin phase interval. The presence of spin phase-dependent CRSF and two of its harmonics were later reported by Mukerjee et al. (2020) in the *Astrosat* spectrum as well. However, analysis of the spin-phase averaged *NuSTAR* spectrum by Kabiraj & Paul (2020) did not require these CRSF lines. The presence of the possible CRSF near 10 keV makes it almost impossible to distinguish *TKF* even if it exists.

We analysed the spectra from three *NuSTAR* observations of the source Obs. Sn.49 (3–79 keV), 50 (3–79 keV), and 51 (3–50 keV) (Table 2). Galactic absorption towards the source could not be constrained by the fit, therefore we fixed it to the Galactic value of  $6 \times 10^{21}$  atoms  $\text{cm}^{-2}$ . Iron fluorescence line was present, which is fitted with a `Gaussian`. No significant residuals resembling the reported CRSF line(s) were visible during the fitting, probably because it becomes evident only if one performs spin-phase resolved spectroscopy (see Molkov et al. 2019).

The best-fitting models on Obs. Sn.49 and 50 contain *TKF*, while the best-fitting model on Obs. Sn.51 does not contain *TKF*.

The spectral parameters of the best-fitting models for all three observations of GRO J2058+42 are given in Tables A1 and A2. The spectral fits for Obs. Sn.49 (having *TKF*) and Obs. Sn.51 (having no *TKF*) are shown in Fig. 27.

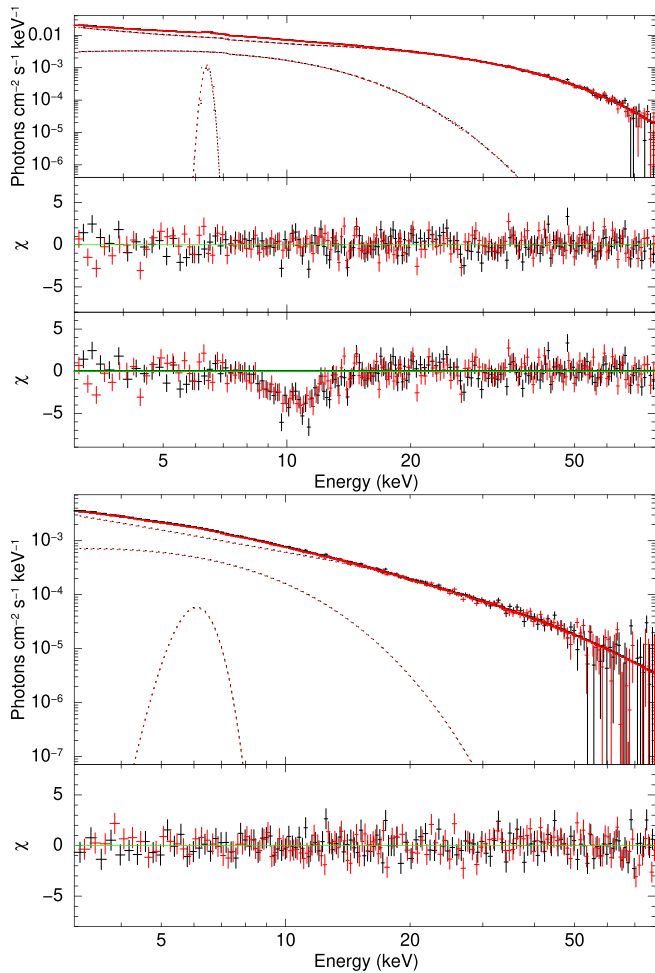


**Figure 27.** Top: Spectral fit on GRO J2058+42 Obs. Sn.49 with `compTT` continuum model, having *TKF*. The top panel shows the best-fitting model, the middle panel shows the residuals to the best-fitting model, and the bottom panel shows the residuals when the strength of the `gabs` component modelling *TKF* is set to 0. Bottom: Spectral fit on GRO J2058+42 Obs. Sn.51 with `newcut` continuum model, having no *TKF*. The top panel shows the best-fitting model and the bottom panel shows the residuals to the best-fitting model.

### 3.28 1E 1145.1–6141

1E 1145.1–6141 is a persistent HMXB pulsar located  $\sim 8.5$  kpc away, hosting the 297 s pulsar that accretes from the wind of B-type supergiant companion star in an eccentric ( $e \sim 0.2$ ), 14.4 d orbit (see Ray & Chakrabarty 2002; Ghising et al. 2022), and references therein.

We analysed the 3–60 keV spectrum from one *NuSTAR* observation of the source, Obs. Sn.52 in Table 2. Iron fluorescence line was present, which is fitted with a `Gaussian`.

The best-fitting model on Obs. Sn.52 does not contain *TKF*.

The spectral parameters of the best-fitting models for Obs. Sn.52 of 1E 1145.1–6141 are given in Tables A1 and A2. The spectral fit for the time-averaged spectrum of Obs. Sn.52 (having no *TKF*) is shown in Fig. 28.

### 3.29 OAO 1657–415

OAO 1657–415 is an HMXB pulsar located  $\sim 2.2$  kpc away, hosting the 38 s pulsar in an eccentric orbit ( $e \sim 0.1$ ) around the early-type Ofpe/WN9 supergiant. The binary has an orbital period of about 10.4 d (see Saavedra et al. 2022, and references therein). The spectrum

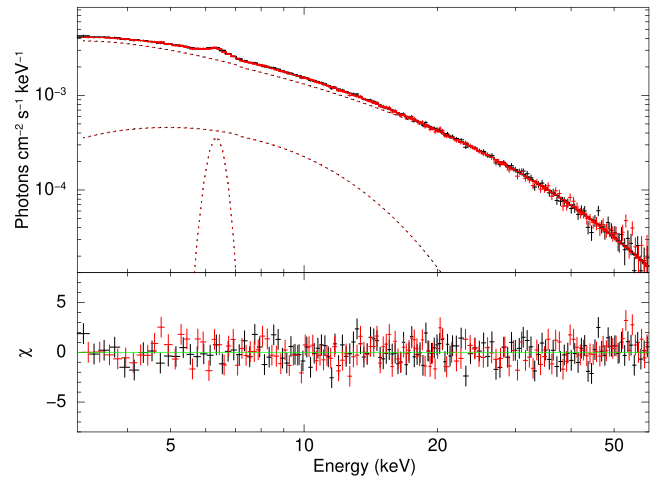


**Figure 28.** Spectral fit using `newcut` continuum model on 1E 1145.1–6141 Obs. Sn.52, having no *TKF*. The top panel shows the best-fitting model and the bottom panel shows the residuals to the best-fitting model.

of OAO 1657–415 is generally characterized by heavily absorbed power-law models modified by CRSF at  $\sim 36$  keV (Orlandini et al. 1999; Pradhan et al. 2014a).

We analysed the 5–70 keV spectrum from one *NuSTAR* observation of the source, Obs. Sn.53 in Table 2. The FPMA module was contaminated by stray light from a nearby source, because of which there was a significant deviation in spectra from FPMA and FPMB below  $\sim 5$  keV. We tried selecting an annular background region around the source region in FPMA so that the background will include any streak of stray light contaminating the source region. Even though the residuals improved, residuals still deviated in FPMA and FPMB below 5 keV. Galactic absorption towards the source could not be constrained by the fit, therefore we fixed it to the Galactic value of  $1.81 \times 10^{22}$  atoms  $\text{cm}^{-2}$ . Iron fluorescence line was present, which is fitted with a `Gaussian`. The width of the iron emission line was not constrained by the fit and we fixed it to 10 eV. CRSF was not present in the spectrum.

The best-fitting model on Obs. Sn.53 does not contain *TKF*.

The spectral parameters of the best-fitting models for Obs. Sn.53 of OAO 1657–415 are given in Tables A1 and A2. The spectral fit for the time-averaged spectrum of Obs. Sn.53 (having no *TKF*) is shown in Fig. 29.

### 3.30 EXO 2030+375

EXO 2030+375 is a transient HMXB pulsar with  $P_{\text{spin}} \sim 42$  s located about 7 kpc away, that hosts the NS and a Be-companion star in an eccentric ( $e \sim 0.36$ ) 46 d orbit (see Parmar et al. 1989 and Wilson et al. 2002). EXO 2030+375 is a well-studied source, and it exhibits regular Type-I outbursts during every periastron passage. Its outburst spectrum is generally modelled with an absorbed power-law model having an exponential cutoff at high energy, with emission lines of iron (see Reig & Coe 1999 and Naik et al. 2013).

We analysed the spectra from three *NuSTAR* observations, Obs. Sn.54 (3–55 keV), Obs. Sn.55 (3–79 keV), and Obs. Sn.56 (3–79 keV) (Table 2). Galactic absorption towards the source could not be constrained by the fit, therefore we fixed it to the Galactic value of  $8 \times 10^{21}$  atoms  $\text{cm}^{-2}$ . Iron fluorescence line was present in all the observations, which were fitted with a `Gaussian`. The width of the iron emission line was not constrained by the fit in Obs. Sn.55 and we fixed it to 10 eV.

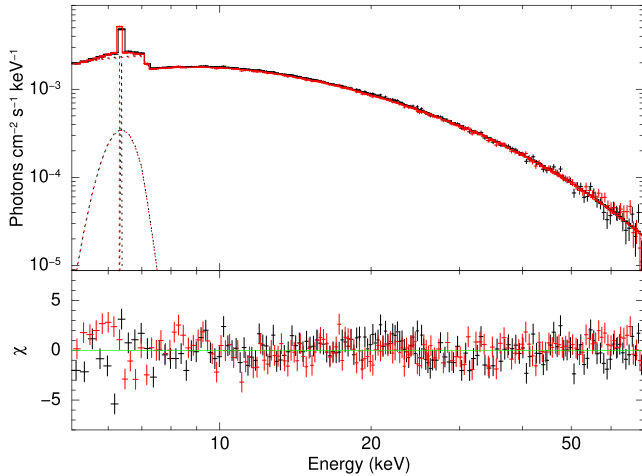


**Figure 29.** Spectral fit using `cutoffpl` continuum model on OAO 1657–415 Obs. Sn.53. Top panel shows the best-fitting model and the bottom panel shows the residuals to the best-fitting model.

The best-fitting models on Obs. Sn.54 and 56 contain *TKF*, while the best-fitting model on Obs. Sn.55 does not contain *TKF*.

The spectral parameters of the best-fitting models for all three observations of EXO 2030+375 are given in Tables A1 and A2. The spectral fit for the time-averaged spectrum of Obs. Sn.54 (having *TKF*) and Obs. Sn.55 (having no *TKF*) are shown in Fig. 30.

### 3.31 IGR J19294+1816

IGR J19294+1816 is a transient HMXB pulsar located  $\sim 11$  kpc away in the Perseus spiral arm of Milky way, hosting the NS and a Be-type companion. The NS has a spin period of 12.4 s, and the binary has an orbital period of about 117 d (see Rodriguez et al. 2009, and references therein). The source spectrum is characterized by an absorbed power law. Discovery of CRSF was claimed in the RXTE spectrum at  $\sim 35$  keV by Roy et al. (2017). However, a reanalysis of the same data by Tsygankov et al. (2019c) could not detect this CRSF. They detected the CRSF at  $\sim 42$  keV in the *NuSTAR* data, and the same line was detected by Raman et al. (2021) in the *Astrosat* data.

We analysed the spectra from two *NuSTAR* observations, Obs. Sn.57 and Obs. Sn.58 (Table 2). Obs. Sn.57 and 58 were dominated by background photons above 20 and 50 keV, respectively. Therefore 3–20 keV spectrum of Obs. Sn.57 and 3–50 keV spectrum of Obs. Sn.58 were analysed. Iron fluorescence line was present only in Obs. Sn.57, which was fitted with a `Gaussian`. The spectrum of Obs. Sn.58 could be fitted without the requirement of the CRSF reported in Tsygankov et al. (2019c).

The best models for validation were based on the top 10 per cent AIC on the training data set of Obs. Sn.57 because only one model was in the top 5 per cent AIC. The best-fitting models on Obs. Sn.56 and 57 do not contain *TKF*.

The spectral parameters of the best-fitting models for both observations of IGR J19294+1816 are given in Tables A1 and A2. The spectral fit for Obs. Sn.57 (having no *TKF*) is shown in Fig. 31.

## 4 DISCUSSION

We (re)analysed the *NuSTAR* broad-band spectra of 30 XRP (Table 2), and 9 of them viz., Vela X–1, Her X–1, XTE J1946+274, 4U 1907+09, 4U 1538–52, Cep X–4, SMC X–1, GX 304–1, and EXO 2030+375 (see Table 1) have previous report(s) of *TKF*.

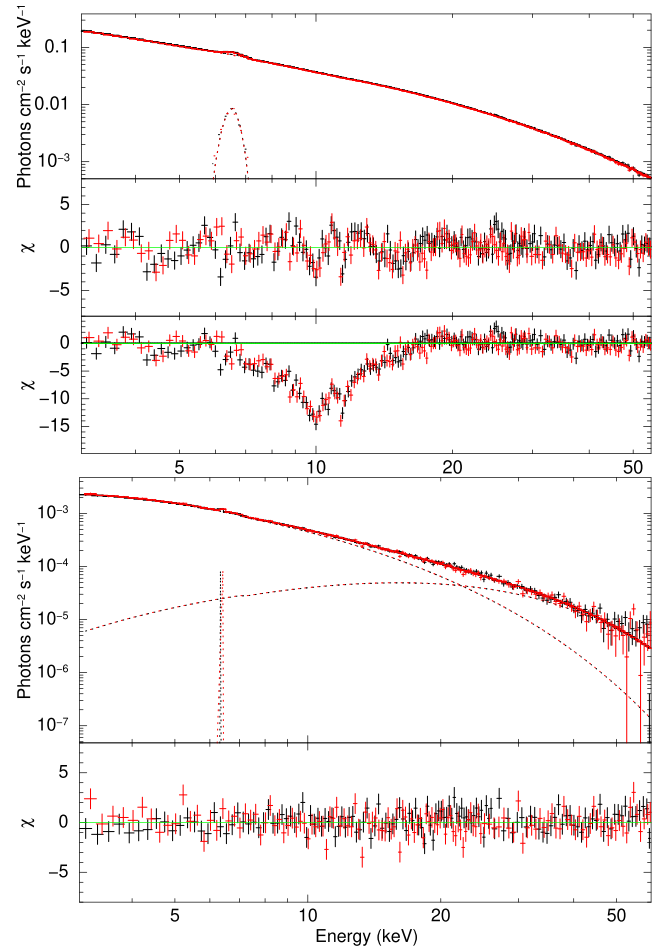


**Figure 30.** Top: Spectral fit on EXO 2030+375 Obs. Sn.54 with `cutoffpl` continuum model, having *TKF*. The top panel shows the best-fitting model, the middle panel shows the residuals to the best-fitting model, and the bottom panel shows the residuals when the strength of the `gabs` component modelling *TKF* is set to 0. Bottom: Spectral fit on EXO 2030+375 Obs. Sn.55 with `npeX` continuum model, having no *TKF*. The top panel shows the best-fitting model and the bottom panel shows the residuals to the best-fitting model.

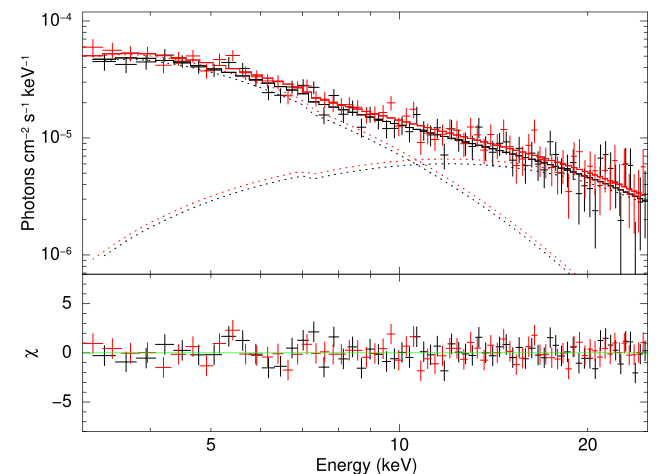


**Figure 31.** Spectral fit using `npeX` continuum model on IGR J19294+1816 Obs. Sn.57, having no *TKF*. The top panel shows the best-fitting model and the bottom panel shows the residuals to the best-fitting model.

After separating the flare and out-of-flare spectra in observations containing flares, separating the eclipse and out-of-eclipse spectra in observations containing eclipses, and by performing a systematic two-step spectral analysis of each observation given in Table 2 that gives importance to data in the 3–15 keV (where *TKF* is present) in the model selection, we detected *TKF* in 11 sources viz., Her X–1, Vela X–1, XTE J1946+274, 4U 1907+09, IGR J16393–4643, RX J0520.5–6932, Cen X–3, 4U 1700–37, LMC X–4, GRO J2058+42, and EXO 2030+375. This is contrary to previous reports of *TKF* in 4U 1538–52, Cep X–4, SMC X–1, and GX 304–1, and no previous reports of *TKF* in IGR J16393–4643, RX J0520.5–6932, Cen X–3, 4U 1700–37, LMC X–4, and GRO J2058+42. The centre of the  $\text{gabs}$  used to model the *TKF* varies from 9 to 11 keV, while the width varies between 1 and 2 keV. The significance of this feature varies, which is very low in some observations (see Figs 12 and 14), moderately significant in some (see Figs 2, 4, 15) and prominent in others (see Figs 3, 21, and 30).

The best-fitting composite model(s) on the broad-band (3–79 keV) data were identified from a set of composite models screened based on how well they fit the 3–15 keV narrower passband (10 keV range) data. The best-fitting model was selected based on AIC score that considers the fit statistic but also penalizes for the model’s complexity (refer Section 3.1). The presence of *TKF* was assessed from the presence of  $\text{gabs}$  component modelling *TKF* in the composite model. As a consequence of this model selection methodology, different observations of the same source were sometimes fitted with different continuum models. This is however justified as the literature shows that the observations acquired at different times from the same source have often been fitted with different continuum models (see Table 1). Also, there are instances where the best-fitting models from this work have *TKF* but individual spectral analysis of some of these observations reported by other authors do not report this feature (see for e.g. Tomar et al. 2021; Bhalerao et al. 2015, and Bodaghee et al. 2016). However, this is inevitable when the selection of best-fitting model on a large set of observations happens in a systematic fashion.

Of the 58 different observations, 14 observations from 11 sources have shown the presence of this feature. Due to the presence of a CRSF at  $\sim 15$  keV, this feature could not be checked on one observation of XTE J1829–098 (Obs. Sn.28). Because none of the mentioned models could give good fits to the spectrum, Obs. Sn.48 of 1A 0535+26 could not be checked for this feature. Therefore, the presence of *TKF* could be checked in 56 observations out of 58. Single-step validation fitting process had to be performed on 8 observations as the best-fitting training models does not fit the validation data set. The two step fitting process as outline before could be performed on 48 observations out of 58.

We screened the best-fitting models on the validation set within the top 5 per cent AIC score and have reported the best two models of two different kinds amongst them, in which one contains *TKF* and the other does not. In some cases, the best-fitting models on the validation set within the top 5 per cent AIC score only contain one kind of model, in which case only one is reported. 36 out of 58 observations only had the best-fitting models that do not contain *TKF*. Out of the rest, 6 out of 22 could be well fitted with two different kinds of composite models in which one contains *TKF* while the other does not contain *TKF*. Of the rest, 14 out of 16 include only the composite model containing *TKF* in the top 5 per cent AIC. The two left out observations (Obs. Sn.35 and 38) showed something peculiar; these are the two observations of LMC X–4 and have a flare in each of them. The best-fitting models on the time-averaged spectra of Obs. Sn.38 contain *TKF*, while the best-fitting models on

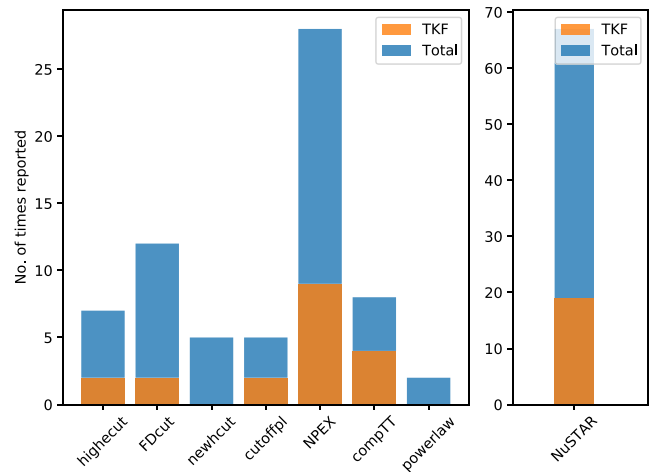


**Figure 32.** The bar chart shows the results of our analysis of the *NuSTAR* spectral data. The distributions of *TKF* found for different continuum models are shown.

the separated flaring state and out-of-flare state spectra of Obs. Sn.38 do not contain *TKF*. This is not, however, entirely true for Obs. Sn. 35. While the time-averaged spectra of 35 could only be fitted with models containing *TKF* and the out-of-flare state spectrum does not need the feature, the flaring state spectrum shows the presence of it. This indicates that a combination of the flare and out-of-flare state spectrum could also mimic *TKF* like residuals. However, this was not observed in 4U 1700–37 (Obs. Sn.34), where the best-fitting models to time-averaged as well as separated flare and out-of-flare state spectrum contains *TKF*. A bar chart representation of the *TKF* detected with different continuum models in this work is shown in Fig. 32. Of the 67 spectra analysed in this work from 58 observations, NPEX was the continuum model that fitted the majority of the spectra (28 out of 67), and *TKF* was detected in 19 spectra. However, the 19 *TKF* detections also include the 6 spectral sets of LMC X–4, where the presence of flare is possibly causing the presence of *TKF*. Excluding those 6, there are 13 spectral sets with a *TKF* detection.

In 4U 1907+09 (Obs. Sn.12), there were systematic absorption residuals left by almost every fit near 8 keV, and hence we re-performed the fitting by allowing the centre of the  $\text{gabs}$  accounting *TKF* to vary down to a lower limit of 7 keV. This is an exception to other cases of detection where the centre of *TKF* stayed within 9–11 keV. We also found that the best-fitting models on none of the *NuSTAR* observations of KS 1947+300 have an absorption feature near 12 keV (Section 3.5, Fig. 5), whose identification as CRSF (Fürst et al. 2014c) or an artefact due to two-component Comptonization model in low luminosity XRP (Doroshenko et al. 2017a) is debated.

The accretion-powered X-ray pulsars show flares and dips in their light curves, and sometimes there are spectral changes associated with the change in intensity (Pradhan et al. 2014b). Analysis of time-averaged spectrum, including persistent intensity, dips, flares, eclipses etc., is equivalent to fitting spectra of the sum of different power-law components with a single power law. We have taken care of this in the current analysis. XRP also show a significant variation in absorption column density with time (Pradhan et al. 2014b). We have used a partial covering absorption model to account for the column density variations at short intervals which may happen due to the clumpiness of the stellar wind of the companion. In particular, *TKF* was not observed in broad-band X-ray spectra of XRP when a partial covering absorption component was used in Maitra & Paul (2013b) and Maitra, Paul & Naik (2012). As mentioned in Section

1, analysis of the same data by different groups also have obtained different results regarding the *TKF*. In a systematic spectral study of the CRSF in XRPCs using *BeppoSAX* by Doroshenko (2017), *TKF* was not required to model the spectrum in any of the sources as well. This feature being consistently at or near 10 keV, is unlikely to be related to the magnetic field of the neutron star. It was noted earlier that instead of some physical reason, the *TKF* appears from modelling the continuum below the cutoff energy with a simple model, and the NPX model was moderately successful in removing this feature from the residuals in some cases (Coburn et al. 2002).

It is also worth noting that features that perfectly resemble *TKF* have been reported in other classes of sources like non-pulsating neutron star X-ray binaries as well, for instance, the *Ginga* observation of GX 5–1 reported in Asai et al. (1994). However, this additional feature is neither reported nor has any mention in the subsequent observations of the same source by *INTEGRAL* (Paizis et al. 2005) and *NuSTAR* (Homan et al. 2018). In the recent *NuSTAR* observations, the authors have used multicomponent continuum models that have transition near 10 keV (see fig. 2 of Homan et al. 2018). *TKF* seen in XRPCs could also be similar in nature.

## 5 CONCLUSION

‘10 keV feature’ has been frequently reported in the spectrum of XRPCs since the *RXTE* era. *NuSTAR* is the most ideal X-ray observatory as of now which can study ‘10 keV feature’, and we performed a systematic search for the ‘10 keV feature’ in archival *NuSTAR* observations of XRPCs. We found the ‘10 keV feature’ in 16 out of 58 *NuSTAR* observations of XRPCs. It could be fitted with a Gaussian absorption model centred around 10 keV in 15 out of 16 cases (exception 4U 1907+09). Of these 16 reports, two of the observations could have an appearance of this feature due to flare in the observation. We however also report that individual analyses of some of these observations in the literature have reported models without the ‘10 keV feature’.

## ACKNOWLEDGEMENTS

The authors thank the anonymous referee for the constructive comments, especially for pointing out the bias in the model selection in the original manuscript. This research has made use of data and/or software provided by the High Energy Astrophysics Science Archive Research Center (HEASARC), which is a service of the Astrophysics Science Division at NASA/GSFC. This research has made use of the *NuSTAR* Data Analysis Software (*NuSTARDAS*) jointly developed by the ASI Science Data Center (Italy) and the California Institute of Technology (USA).

## DATA AVAILABILITY

All the data underlying this research work is publicly available in the High Energy Astrophysics Science Archive Research Center (HEASARC Data Archive).

## REFERENCES

Akaike H., 1998, in Parzen E., Tanabe K., Kitagawa G., eds, *Selected Papers of Hirotugu Akaike*. Springer, New York, p. 199  
 Antia H. M. et al., 2017, *ApJS*, 231, 10  
 Arnaud K. A., 1996, in Jacoby G. H., Barnes J. eds, *ASP Conf. Ser. Vol. 101, Astronomical Data Analysis Software and Systems V*. Astron. Soc. Pac., San Francisco, p. 17  
 Asai K., Dotani T., Mitsuda K., Nagase F., Kamado Y., Kuulkers E., Breedon L. M., 1994, *PASJ*, 46, 479  
 Bala S., Roy J., Bhattacharya D., 2020a, *MNRAS*, 493, 3045

Bala S., Bhattacharya D., Staubert R., Maitra C., 2020b, *MNRAS*, 497, 1029  
 Ballhausen R. et al., 2016, *A&A*, 591, A65  
 Ballhausen R. et al., 2017, *A&A*, 608, A105  
 Barnstedt J. et al., 2008, *A&A*, 486, 293  
 Baum Z. A., Cherry M. L., Rodi J., 2017, *MNRAS*, 467, 4424  
 Bellm E. C. et al., 2014, *ApJ*, 792, 108  
 Bhalerao V. et al., 2015, *MNRAS*, 447, 2274  
 Bhargava Y., Bhalerao V., Ballhausen R., Fürst F., Pottschmidt K., Tomsick J. A., Wilms J., 2019, *MNRAS*, 482, 2902  
 Bodaghee A. et al., 2016, *ApJ*, 823, 146  
 Boella G., Butler R. C., Perola G. C., Piro L., Scarsi L., Bleeker J. A. M., 1997, *A&AS*, 122, 299  
 Bonnet-Bidaud J. M., Mouchet M., 1998, *A&A*, 332, L9  
 Bozzo E. et al., 2018, *A&A*, 613, A22  
 Brumback M. C., Hickox R. C., Fürst F. S., Pottschmidt K., Tomsick J. A., Wilms J., 2020, *ApJ*, 888, 125  
 Burderi L., Di Salvo T., Robba N. R., La Barbera A., Guainazzi M., 2000, *ApJ*, 530, 429  
 Caballero I. et al., 2007, *A&A*, 465, L21  
 Caballero I. et al., 2013, *ApJ*, 764, L23  
 Camero Arranz A., Wilson C. A., Connell P., Martínez Núñez S., Blay P., Beckmann V., Reglero V., 2005, *A&A*, 441, 261  
 Camero-Arranz A., Pottschmidt K., Finger M., Ikhsanov N., Wilson-Hodge C., Marcu D., 2012, *A&A*, 546, A40  
 Choi C. S., Dotani T., Day C. S. R., Nagase F., 1996, *ApJ*, 471, 447  
 Clark G. W., Woo J. W., Nagase F., Makishima K., Sakao T., 1990, *ApJ*, 353, 274  
 Clark D. J., Hill A. B., Bird A. J., McBride V. A., Scaringi S., Dean A. J., 2009, *MNRAS*, 399, L113  
 Coburn W., Heindl W. A., Rothschild R. E., Gruber D. E., Kreykenbohm I., Wilms J., Kretschmar P., Staubert R., 2002, *ApJ*, 580, 394  
 Coe M. J., Negueruela I., Buckley D. A. H., Haigh N. J., Laycock S. G. T., 2001, *MNRAS*, 324, 623  
 Corbet R. H. D., Marshall F. E., Coe M. J., Laycock S., Handler G., 2001, *ApJ*, 548, L41  
 Cox N. L. J., Kaper L., Mokiem M. R., 2005, *A&A*, 436, 661  
 Crampton D., Hutchings J. B., Cowley A. P., 1978, *ApJ*, 223, L79  
 Cusumano G., di Salvo T., Burderi L., Orlandini M., Piraino S., Robba N., Santangelo A., 2000, *Adv. Space Res.*, 25, 409  
 D’Ai A., Cusumano G., Del Santo M., La Parola V., Segreto A., 2017, *MNRAS*, 470, 2457  
 Devaraj A., Paul B., 2022, *MNRAS*, 517, 2599  
 Devasia J., James M., Paul B., Indulekha K., 2011, *MNRAS*, 417, 348  
 Diez C. M., et al. 2022, *A&A*, 660, A19  
 Doroshenko R., 2017, PhD thesis, Universitätsbibliothek Tübingen  
 Doroshenko R., Santangelo A., Doroshenko V., Piraino S., 2017a, *A&A*, 600, A52  
 Doroshenko V. A., Doroshenko R. F., Postnov K. A., Cherepashchuk A. M., Tsygankov S. S., 2008, *Astron. Rep.*, 52, 138  
 Doroshenko V., Santangelo A., Suleimanov V., Kreykenbohm I., Staubert R., Ferrigno C., Klochkov D., 2010, *A&A*, 515, A10  
 Doroshenko V., Tsygankov S. S., Mushtukov A. A., Lutovinov A. A., Santangelo A., Suleimanov V. F., Poutanen J., 2017b, *MNRAS*, 466, 2143  
 Doroshenko R., Piraino S., Doroshenko V., Santangelo A., 2020, *MNRAS*, 493, 3442  
 Drave S. P., Bird A. J., Townsend L. J., Hill A. B., McBride V. A., Sguera V., Bazzano A., Clark D. J., 2012, *A&A*, 539, A21  
 Drave S. P., Bird A. J., Sidoli L., Sguera V., Bazzano A., Hill A. B., Goossens M. E., 2014, *MNRAS*, 439, 2175  
 Enoto T. et al., 2008, *PASJ*, 60, S57  
 Epili P., Naik S., Jaisawal G. K., Gupta S., 2017, *MNRAS*, 472, 3455  
 Ferrigno C., Segreto A., Mineo T., Santangelo A., Staubert R., 2008, *A&A*, 479, 533  
 Ferrigno C. et al., 2016, *A&A*, 595, A17  
 Filippova E. V., Tsygankov S. S., Lutovinov A. A., Sunyaev R. A., 2005, *Astron. Lett.*, 31, 729  
 Fiume D. D. et al., 1998, *A&A*, 329, L41

- Frontera F., Costa E., Dal Fiume D., Feroci M., Nicastro L., Orlandini M., Palazzi E., Zavattini G., 1997, *Astron. Astrophys. Suppl. Ser.*, 122, 357
- Fürst F. et al., 2013, *ApJ*, 779, 69
- Fürst F. et al., 2014a, *ApJ*, 780, 133
- Fürst F. et al., 2014b, American Astronomical Society Meeting Abstracts #223, 438.20
- Fürst F. et al., 2014c, *ApJ*, 784, L40
- Fürst F. et al., 2015, *ApJ*, 806, L24
- Fürst F. et al., 2017, *A&A*, 606, A89
- Fürst F. et al., 2018, *A&A*, 620, A153
- Galloway D. K., Morgan E. H., Levine A. M., 2004, *ApJ*, 613, 1164
- Ghising M., Tobrej M., Rai B., Tamang R., Paul B. C., 2022, *MNRAS*, 517, 4132
- Giacconi R., Gursky H., Kellogg E., Schreier E., Tananbaum H., 1971, *ApJ*, 167, L67
- Giacconi R., Gursky H., Kellogg E., Levinson R., Schreier E., Tananbaum H., 1973, *ApJ*, 184, 227
- Gruber D. E., Heindl W. A., Rothschild R. E., Coburn W., Staubert R., Kreykenbohm I., Wilms J., 2001, *ApJ*, 562, 499
- Haberl F., Day C., 1992, *A&A*, 263, 241
- Halpern J., Gotthelf E., 2007, *ApJ*, 669, 579
- Harding A. K., 2003, in Cusumano G., Massaro E., Mineo T., eds, Pulsars, AXPs and SGRs Observed with BeppoSAX and Other Observatories. Aracne Editrice, Roma, Italy, p. 127
- Harrison F. A. et al., 2013, *ApJ*, 770, 103
- Heindl W. A., Coburn W., Gruber D. E., Rothschild R. E., Kreykenbohm I., Wilms J., Staubert R., 2001, *ApJ*, 563, L35
- Hemphill P. B., Rothschild R. E., Caballero I., Pottschmidt K., Kühnel M., Fürst F., Wilms J., 2013, *ApJ*, 777, 61
- Hemphill P. B. et al., 2019, *ApJ*, 873, 62
- Hickox R. C., Narayan R., Kallman T. R., 2004, *ApJ*, 614, 881
- Homan J., Steiner J. F., Lin D., Fridriksson J. K., Remillard R. A., Miller J. M., Ludlam R. M., 2018, *ApJ*, 853, 157
- Hung L.-W., Hickox R. C., Boroson B. S., Vrtilsek S. D., 2010, *ApJ*, 720, 1202
- Inam S., Baykal A., Beklen E., 2010, *MNRAS*, 403, 378
- Isenberg M., Lamb D. Q., Wang J. C. L., 1998, *ApJ*, 505, 688
- Islam N., Maitra C., Pradhan P., Paul B., 2015, *MNRAS*, 446, 4148
- Iwakiri W. et al., 2012, *ApJ*, 751, 35
- Iwakiri W. B. et al., 2019, *ApJ*, 878, 121
- Jahoda K., Swank J. H., Giles A. B., Stark M. J., Strohmayer T., Zhang W., Morgan E. H., 1996, in Siegmund O. H., Gummin M. A. eds, Proc. SPIE Conf. Ser. Vol. 2808, EUV, X-Ray, and Gamma-Ray Instrumentation for Astronomy VII. SPIE, Bellingham, p. 59
- Jaisawal G. K., Naik S., 2014, *Bull. Astron. Soc. India*, 42, 147
- Jaisawal G. K., Naik S., 2015a, *MNRAS*, 448, 620
- Jaisawal G. K., Naik S., 2015b, *MNRAS: Lett.*, 453, L21
- Jaisawal G. K., Naik S., 2016, *MNRAS*, 461, L97
- Jaisawal G. K., Naik S., Epili P., 2016, *MNRAS*, 457, 2749
- Jaisawal G. K., Naik S., Gupta S., Agrawal P. C., Jana A., Chhotaray B., Epili P. R., 2021a, *J. Astrophys. Astron.*, 42, 33
- Jaisawal G. K., Naik S., Epili P. R., Chhotaray B., Jana A., Agrawal P. C., 2021b, *J. Astrophys. Astron.*, 42, 72
- Kaastra J. S., Bleeker J. A. M., 2016, *A&A*, 587, A151
- Kabiraj S., Paul B., 2020, *MNRAS*, 497, 1059
- Kabiraj S., Islam N., Paul B., 2019, *MNRAS*, 491, 1491
- Kamata Y., Koyama K., Tawara Y., Makishima K., Ohashi T., Kawai N., Hatsukade I., 1990, *PASJ*, 42, 785
- Kelley R. L., Rappaport S., Ayasli S., 1983, *ApJ*, 274, 765
- Kii T., Hayakawa S., Nagase F., Ikegami T., Kawai N., 1986, *PASJ*, 38, 751
- Klochkov D., Santangelo A., Staubert R., Ferrigno C., 2008, *A&A*, 491, 833
- Klochkov D. et al., 2007, in Proc. VI INTEGRAL Workshop: The Obscured Universe. ESA, Moscow, p. 461
- Klochkov D. et al., 2012, *A&A*, 542, L28
- Koyama K. et al., 1991, *ApJ*, 366, L19
- Koyama K. et al., 2007, *PASJ*, 59, 23
- Kreykenbohm I., Kretschmar P., Wilms J., Staubert R., Kendziorra E., Gruber D., Heindl W., Rothschild R., 1999, *A&A*, 341, 141
- Kreykenbohm I., Coburn W., Wilms J., Kretschmar P., Staubert R., Heindl W. A., Rothschild R. E., 2002, *A&A*, 395, 129
- Kreykenbohm I. et al., 2004, in Schoenfelder V., Lichti G., Winkler C., eds, ESA Special Publication, Vol. 552, 5th INTEGRAL Workshop on the INTEGRAL Universe. ESA, Munich, p. 333
- Kreykenbohm I. et al., 2006, in Wilson A., ed., ESA Special Publication, Vol. 604, The X-ray Universe 2005. ESA, Madrid, p. 275
- Kuehnel M., Finger M. H., Fuerst F., Pottschmidt K., Haberl F., Wilms J., 2014, *Astron. Telegram*, 5856, 1
- Kühnel M. et al., 2013, *A&A*, 555, A95
- La Barbera A., Burderi L., Di Salvo T., Iaria R., Robba N., 2001, *ApJ*, 553, 375
- La Barbera A., Santangelo A., Orlandini M., Segreto A., 2003, *A&A*, 400, 993
- La Barbera A. et al., 2004, in Schoenfelder V., Lichti G., Winkler C. eds, ESA Special Publication, Vol. 552, 5th INTEGRAL Workshop on the INTEGRAL Universe. ESA, Munich, p. 337
- La Barbera A., Segreto A., Santangelo A., Kreykenbohm I., Orlandini M., 2005, *A&A*, 438, 617
- Levine A., Rappaport S., Putney A., Corbet R., Nagase F., 1991, *ApJ*, 381, 101
- Li F., Jernigan G., Clark G., 1977, *IAU Circ.*, 3125, 1
- Lund N. et al., 2003, *A&A*, 411, L231
- Lutovinov A., Tsygankov S., Revnivtsev M., Chernyakova M., Bikmaev I., Molkov S., Burenin R., Sakhbullin N., 2004, 5th INTEGRAL Workshop on the INTEGRAL Universe, 552, 253
- Lutovinov A. A., Tsygankov S. S., Suleimanov V. F., Mushtukov A. A., Doroshenko V., Nagirner D. I., Poutanen J., 2015, *MNRAS*, 448, 2175
- Lutovinov A. A., Buckley D. A. H., Townsend L. J., Tsygankov S. S., Kennea J., 2016, *MNRAS*, 462, 3823
- Lutovinov A. et al., 2021, *ApJ*, 912, 17
- Maitra C., Paul B., 2013a, *ApJ*, 763, 79
- Maitra C., Paul B., 2013b, *ApJ*, 771, 96
- Maitra C., Paul B., Naik S., 2012, *MNRAS*, 420, 2307
- Makishima K. et al., 1990, *ApJ*, 365, L59
- Makishima K., Kawai N., Koyama K., Shibazaki N., Nagase F., Nakagawa M., 1984, *PASJ*, 36, 679
- Makishima K., Mihara T., Nagase F., Tanaka Y., 1999, *ApJ*, 525, 978
- Malacaria C., Klochkov D., Santangelo A., Staubert R., 2015, *A&A*, 581, A121
- Malacaria C., Jenke P., Roberts O. J., Wilson-Hodge C. A., Cleveland W. H., and B. M., 2020, *ApJ*, 896, 90
- Malacaria C. et al., 2021, *ApJ*, 909, 153
- Mandal M., Pal S., 2022, *MNRAS*, 511, 1121
- Manzo G., Giarrusso S., Santangelo A., Ciralli F., Fazio G., Piraino S., Segreto A., 1997, *Astron. Astrophys. Suppl. Ser.*, 122, 341
- Marshall N., Ricketts M. J., 1980, *MNRAS*, 193, 7P
- Martínez Núñez S., Reig P., Blay P., Kretschmar P., Lund N., Reglero V., 2003, *A&A*, 411, L411
- McBride V. et al., 2007, *A&A*, 470, 1065
- McClintock J. E., Bradt H. V., Doxsey R. E., Jernigan J. G., Canizares C. R., Hiltner W. A., 1977, *Nature*, 270, 320
- Middleditch J., Mason K. O., Nelson J. E., White N. E., 1981, *ApJ*, 244, 1001
- Mihara T., 1995, PhD thesis, Dept. of Physics, Univ. of Tokyo (M95)
- Mihara T., Makishima K., Kamijo S., Ohashi T., Nagase F., Tanaka Y., Koyama K., 1991, *ApJ*, 379, L61
- Molkov S., Lutovinov A., Tsygankov S., Mereminskiy I., Mushtukov A., 2019, *ApJ*, 883, L11
- Mukerjee K., Antia H. M., Katoch T., 2020, *ApJ*, 897, 73
- Mukherjee U., Paul B., 2004, *A&A*, 427, 567
- Mukherjee U., Bapna S., Raichur H., Paul B., Jaaffrey S. N. A., 2006a, *J. Astrophys. Astron.*, 27, 25
- Mukherjee U., Raichur H., Paul B., Naik S., Bhatt N., 2006b, *J. Astrophys. Astron.*, 27, 411
- Müller S. et al., 2012, *A&A*, 546, A125
- Nabizadeh A., Mönkkönen J., Tsygankov S. S., Doroshenko V., Molkov S. V., Poutanen J., 2019, *A&A*, 629, A101
- Nagase F., 1989, *PASJ*, 41, 1

- Nagase F., Corbet R. H. D., Day C. S. R., Inoue H., Takeshima T., Yoshida K., Mihara T., 1992, *ApJ*, 396, 147
- Naik S., Jaisawal G. K., 2015, *Res. Astron. Astrophys.*, 15, 537
- Naik S., Paul B., 2003, *A&A*, 401, 265
- Naik S., Paul B., 2004a, *A&A*, 418, 655
- Naik S., Paul B., 2004b, *ApJ*, 600, 351
- Naik S., Callanan P. J., Paul B., Dotani T., 2006, *ApJ*, 647, 1293
- Naik S., Paul B., Kachhara C., Vadawale S. V., 2011, *MNRAS*, 413, 241
- Naik S., Maitra C., Jaisawal G. K., Paul B., 2013, *ApJ*, 764, 158
- Odaka H., Khangulyan D., Tanaka Y. T., Watanabe S., Takahashi T., Makishima K., 2013, *ApJ*, 767, 70
- Orlandini M., 2006, *Adv. Space Res.*, 38, 2742
- Orlandini M. et al., 1998a, *A&A*, 332, 121
- Orlandini M. et al., 1998b, *ApJ*, 500, L163
- Orlandini M., dal Fiume D., del Sordo S., Frontera F., Parmar A. N., Santangelo A., Segreto A., 1999, *A&A*, 349, L9
- Owens A., Oosterbroek T., Parmar A., 1997, *A&A*, 324, L9
- Pahari M., Pal S., 2012, *MNRAS*, 423, 3352
- Paizis A., Ebisawa K., Tikkanen T., Rodriguez J., Chenevez J., Kuulkers E., Vilhu O., Courvoisier T. J. L., 2005, *A&A*, 443, 599
- Parmar A. N., White N. E., Stella L., Izzo C., Ferri P., 1989, *ApJ*, 338, 359
- Paul B., Nagase F., Endo T., Dotani T., Yokogawa J., Nishiuchi M., 2002, *ApJ*, 579, 411
- Pike S. N. et al., 2019, *ApJ*, 875, 144
- Pradhan P., Maitra C., Paul B., Islam N., Paul B., 2014b, *MNRAS*, 442, 2691
- Pradhan P., Maitra C., Paul B., Islam N., Paul B. C., 2014a, *MNRAS*, 442, 2691
- Pradhan P., Maitra C., Paul B., 2020, *ApJ*, 895, 10
- Pradhan P., Paul B., Bozzo E., Maitra C., Paul B., 2021, *MNRAS*, 502, 1163
- Raman G., Varun B., Paul B., Bhattacharya D., 2021, *MNRAS*, 508, 5578
- Rampy R. A., Smith D. M., Nequeroela I., 2009, *ApJ*, 707, 243
- Ray P. S., Chakrabarty D., 2002, *ApJ*, 581, 1293
- Reig P., Coe M. J., 1999, *MNRAS*, 302, 700
- Reynolds A., Owens A., Kaper L., Parmar A., Segreto A., 1999, *A&A*, 349, 873
- Rivers E. et al., 2010, *ApJ*, 709, 179
- Robba N. R., di Salvo T., Burderi L., La Barbera A., Cusumano G., 2000, in McConnell M. L., Ryan J. M., eds, *AIP Conf. Proc. Vol. 510, The Fifth Compton Symposium. Am. Inst. Phys., New York*, p. 213
- Rodes-Roca J. J., Torrejón J. M., Kreykenbohm I., Martínez Núñez S., Camero-Arranz A., Bernabéu G., 2009, *A&A*, 508, 395
- Rodriguez J., Tomsick J. A., Bodaghee A., Zurita Heras J. A., Chaty S., Paizis A., Corbel S., 2009, *A&A*, 508, 889
- Rothschild R. et al., 2013, *ApJ*, 770, 19
- Rothschild R. E. et al., 2017, *MNRAS*, 466, 2752
- Roy J., Choudhury M., Agrawal P. C., 2017, *ApJ*, 848, 124
- Saavedra E. A., Fogantini F. A., Combi J. A., García F., Chaty S., 2022, *A&A*, 659, A48
- Sartore N., Jourdain E., Roques J. P., 2015, *ApJ*, 806, 193
- Schanne S., Götz D., Gérard L., Sizun P., Falanga M., Hamadache C., Cordier B., von Kienlin A., 2007, in *Proc. VI INTEGRAL Workshop: The Obscured Universe. ESA SP-622, Moscow*, p. 479
- Schmidtke P. C., Cowley A. P., Hauschildt P. H., Ponder A. L., McGrath T. K., Frattare L. M., Franklin B. E., 1996, *PASP*, 108, 668
- Schreier E., Levinson R., Gursky H., Kellogg E., Tananbaum H., Giacconi R., 1972, *ApJ*, 172, L79
- Schurch M., Udalski A., Coe M., 2008, *Astron. Telegram*, 1670, 1
- Seifina E., Titarchuk L., Shaposhnikov N., 2016, *ApJ*, 821, 23
- Sharma P., Sharma R., Jain C., Dutta A., 2022, *MNRAS*, 509, 5747
- Shtykovsky A., Lutovinov A., Arefiev V., Molkov S., Tsygankov S., Revnivtsev M., 2017, *Astron. Lett.*, 43, 175
- Shtykovsky A. E., Lutovinov A. A., Tsygankov S. S., Molkov S. V., 2019, *MNRAS*, 482, L14
- Staubert R. et al., 2019, *A&A*, 622, A61
- Suchy S., Fürst F., Pottschmidt K., Caballero I., Kreykenbohm I., Wilms J., Markowitz A., Rothschild R. E., 2012, *ApJ*, 745, 124
- Takahashi T. et al., 2007, *PASJ*, 59, 35
- Tamang R., Ghising M., Tobrej M., Rai B., Paul B. C., 2022, *MNRAS*, 515, 5407
- Tanaka Y., 1986, in Mihalas D., Winkler K.-H. A., eds, *Radiation Hydrodynamics in Stars and Compact Objects*. Springer, Berlin, Heidelberg, p. 198
- Tananbaum H., Gursky H., Kellogg E. M., Levinson R., Schreier E., Giacconi R., 1972, *ApJ*, 174, L143
- Tendulkar S. P. et al., 2014, *ApJ*, 795, 154
- Thompson T. W. J., Tomsick J. A., Rothschild R. E., in't Zand J. J. M., Walter R., 2006, *ApJ*, 649, 373
- Titarchuk L., 1994, *ApJ*, 434, 570
- Tobrej M., Rai B., Ghising M., Tamang R., Paul B. C., 2023, *MNRAS*, 518, 4861
- Tomar G., Pradhan P., Paul B., 2021, *MNRAS*, 500, 3454
- Truemper J., Pietsch W., Reppin C., Voges W., Staubert R., Kendziorra E., 1978, *ApJ*, 219, L105
- Tsygankov S. S., Lutovinov A. A., 2005a, *Astron. Lett.*, 31, 88
- Tsygankov S., Lutovinov A., 2005b, *Astron. Lett.*, 31, 380
- Tsygankov S. S., Lutovinov A. A., Churazov E. M., Sunyaev R. A., 2006, *MNRAS*, 371, 19
- Tsygankov S. S., Lutovinov A. A., Krivonos R. A., Molkov S. V., Jenke P. J., Finger M. H., Poutanen J., 2016, *MNRAS*, 457, 258
- Tsygankov S. S., Rouco Escorial A., Suleimanov V. F., Mushtukov A. A., Doroshenko V., Lutovinov A. A., Wijnands R., Poutanen J., 2019a, *MNRAS*, 483, L144
- Tsygankov S. S., Doroshenko V., Mushtukov A. A., Suleimanov V. F., Lutovinov A. A., Poutanen J., 2019b, *MNRAS*, 487, L30
- Tsygankov S. S., Doroshenko V., Mushtukov A. A., Lutovinov A. A., Poutanen J., 2019c, *A&A*, 621, A134
- Turner M. J. L. et al., 1989, *PASJ*, 41, 345
- Varun B., Maitra C., Pradhan P., Raichur H., Paul B., 2019a, *MNRAS*, 484, L1
- Varun B., Pradhan P., Maitra C., Raichur H., Paul B., 2019b, *ApJ*, 880, 61
- Vasco D., Staubert R., Klochkov D., Santangelo A., Shakura N., Postnov K., 2013, *A&A*, 550, A111
- Vasilopoulos G., Haberl F., Sturm R., Maggi P., Udalski A., 2014, *A&A*, 567, A129
- Verner D. A., Ferland G. J., Korista K. T., Yakovlev D. G., 1996, *ApJ*, 465, 487
- Vybornov V., Klochkov D., Gornostaev M., Postnov K., Sokolova-Lapa E., Staubert R., Pottschmidt K., Santangelo A., 2017, *A&A*, 601, A126
- Vybornov V., Doroshenko V., Staubert R., Santangelo A., 2018, *A&A*, 610, A88
- Wang W., 2014a, *Res. Astron. Astrophys.*, 14, 565
- Wang W., 2014b, *MNRAS*, 440, 1114
- White N. E., Swank J. H., Holt S. S., 1983, *ApJ*, 270, 711
- Wilms J., Allen A., McCray R., 2000, *ApJ*, 542, 914
- Wilson C. A., Finger M. H., Coe M. J., Laycock S., Fabregat J., 2002, *ApJ*, 570, 287
- Wilson C. A., Finger M. H., Coe M. J., Nequeroela I., 2003, *ApJ*, 584, 996
- Wilson C. A., Weisskopf M. C., Finger M. H., Coe M. J., Greiner J., Reig P., Papamastorakis G., 2005, *ApJ*, 622, 1024
- Wilson C. A., Finger M. H., Camero-Arranz A., 2008, *ApJ*, 678, 1263
- Woo J. W., Clark G. W., Blondin J. M., Kallman T. R., Nagase F., 1995, *ApJ*, 445, 896
- Woo J. W., Clark G. W., Levine A. M., Corbet R. H., Nagase F., 1996, *ApJ*, 467, 811
- Xiao G. et al., 2019, *J. High Energy Astrophys.*, 23, 29
- Yamamoto T., Sugizaki M., Mihara T., Nakajima M., Yamaoka K., Matsuoka M., Morii M., Makishima K., 2011, *PASJ*, 63, S751
- Yamamoto T., Mihara T., Sugizaki M., Nakajima M., Makishima K., Sasano M., 2014, *PASJ*, 66, 59

## APPENDIX A: TABLE: BEST-FITTING SPECTRAL PARAMETERS

The best-fitting spectral parameters for all the observations analysed in this work are given in two tables.

**Table A1.** The best-fitting continuum model and CRSF model parameters from spectral fitting for Obs. Sn.1 to 58.

Source	Observation details		Continuum parameters				CRSF		Strength <sup>§</sup>
	Obs. Sn.	Energy range	norm. <sub>1</sub>	norm. <sub>2</sub> /T <sub>0</sub> <sup>†</sup> (keV)	E <sub>cut</sub> (keV)/K <sub>T</sub> <sup>‡</sup> (keV)	E <sub>fold</sub> (keV)/Γ <sup>†</sup>	E <sub>cy</sub> (keV)	σ <sub>cy</sub> (keV)	
Her X-1	1 (ta)	3-79	1.11 <sup>+0.08</sup> <sub>-0.07</sub>	0.18 <sup>+0.03</sup> <sub>-0.02</sub>	(3.2 ± 0.1) × 10 <sup>-4</sup>	5.75 <sup>+0.06</sup> <sub>-0.06</sub>	38.20 <sup>+0.34</sup> <sub>-0.33</sub>	7.12 <sup>+0.30</sup> <sub>-0.29</sub>	15.76 <sup>+1.32</sup> <sub>-1.22</sub>
	1 (oe)	3-79	0.95 <sup>+0.01</sup> <sub>-0.01</sub>	0.108 <sup>+0.001</sup> <sub>-0.001</sub>	-	20.51 <sup>+0.40</sup> <sub>-0.34</sub>	38.19 <sup>+0.56</sup> <sub>-0.53</sub>	6.18 <sup>+0.59</sup> <sub>-0.53</sub>	8.86 <sup>+1.45</sup> <sub>-1.23</sub>
Vela X-1	2	3-79	0.82 <sup>+0.05</sup> <sub>-0.05</sub>	0.20 <sup>+0.02</sup> <sub>-0.02</sub>	-	21.07 <sup>+4.37</sup> <sub>-3.34</sub>	37.31 <sup>+0.23</sup> <sub>-0.22</sub>	6.67 <sup>+0.46</sup> <sub>-0.34</sub>	13.91 <sup>+2.71</sup> <sub>-1.58</sub>
	3	3-79	0.77 <sup>+0.04</sup> <sub>-0.05</sub>	0.24 <sup>+0.01</sup> <sub>-0.01</sub>	-	15.75 <sup>+2.27</sup> <sub>-2.68</sub>	37.16 <sup>+0.20</sup> <sub>-0.20</sub>	6.75 <sup>+0.25</sup> <sub>-0.28</sub>	13.13 <sup>+1.14</sup> <sub>-1.03</sub>
	4	3-79	-	0.26 <sup>+0.12</sup> <sub>-0.05</sub>	0.47 <sup>+0.12</sup> <sub>-0.47</sub>	6.56 <sup>+0.09</sup> <sub>-0.08</sub>	24.79 <sup>+0.97</sup> <sub>-1.13</sub>	4.60 <sup>*</sup>	0.54 <sup>+0.15</sup> <sub>-0.12</sub>
	5	3-79	1.05 <sup>+0.05</sup> <sub>-0.06</sub>	0.27 <sup>+0.03</sup> <sub>-0.03</sub>	-	20.91 <sup>+1.03</sup> <sub>-2.02</sub>	54.48 <sup>+0.77</sup> <sub>-0.67</sub>	7.50 <sup>+0.79</sup> <sub>-0.65</sub>	15.93 <sup>+2.73</sup> <sub>-2.09</sub>
	6	3-79	-	(4.2 ± 0.2) × 10 <sup>-3</sup>	1.01 <sup>+0.02</sup> <sub>-0.02</sub>	8.41 <sup>+0.51</sup> <sub>-0.43</sub>	27.05 <sup>+0.38</sup> <sub>-0.38</sub>	3.83 <sup>+1.15</sup> <sub>-1.32</sub>	0.82 <sup>+0.49</sup> <sub>-0.42</sub>
	"	3-79	-	0.10 <sup>+0.40</sup> <sub>-0.01</sub>	0.29 <sup>+0.11</sup> <sub>-0.29</sub>	7.29 <sup>+0.19</sup> <sub>-0.22</sub>	57.18 <sup>+0.83</sup> <sub>-1.24</sub>	9.59 <sup>+1.35</sup> <sub>-1.23</sub>	34.56 <sup>+7.80</sup> <sub>-7.16</sub>
	7 (f)	3-79	1.16 <sup>+0.04</sup> <sub>-0.06</sub>	0.27 <sup>+0.03</sup> <sub>-0.04</sub>	-	21.80 <sup>+0.68</sup> <sub>-0.70</sub>	27.71 <sup>+1.26</sup> <sub>-2.51</sub>	5.83 <sup>+0.33</sup> <sub>-0.33</sub>	3.31 <sup>+0.59</sup> <sub>-0.59</sub>
XTE J1946+274	8	3-60	0.99 <sup>+0.04</sup> <sub>-0.04</sub>	0.07 <sup>+0.01</sup> <sub>-0.01</sub>	-	18.10 <sup>+0.19</sup> <sub>-0.19</sub>	52.59 <sup>+0.97</sup> <sub>-0.97</sub>	8.95 <sup>+1.16</sup> <sub>-1.16</sub>	25.67 <sup>+2.66</sup> <sub>-2.66</sub>
KS 1947+300	9	3-79	1.17 <sup>+0.07</sup> <sub>-0.07</sub>	0.23 <sup>+0.05</sup> <sub>-0.04</sub>	-	7.99 <sup>+0.27</sup> <sub>-0.31</sub>	24.85 <sup>+0.78</sup> <sub>-0.74</sub>	5.83 <sup>*</sup>	2.34 <sup>+0.42</sup> <sub>-0.29</sub>
	10	3-79	0.80 <sup>+0.03</sup> <sub>-0.04</sub>	0.32 <sup>+0.03</sup> <sub>-0.04</sub>	(2.1 ± 0.3) × 10 <sup>-5</sup>	10.70 <sup>+0.25</sup> <sub>-0.22</sub>	50.79 <sup>+0.75</sup> <sub>-0.66</sub>	6.07 <sup>+1.24</sup> <sub>-0.84</sub>	10.45 <sup>+4.19</sup> <sub>-2.26</sub>
	11	3-79	0.69 <sup>+0.03</sup> <sub>-0.04</sub>	0.15 <sup>+0.02</sup> <sub>-0.02</sub>	(1.0 ± 0.2) × 10 <sup>-5</sup>	11.31 <sup>+0.38</sup> <sub>-0.31</sub>	27.71 <sup>+1.26</sup> <sub>-2.51</sub>	3.40 <sup>+2.12</sup> <sub>-1.49</sub>	1.10 <sup>+1.29</sup> <sub>-0.59</sub>
4U 1907+09	12	3-45	-	0.021 <sup>+0.013</sup> <sub>-0.002</sub>	0.36 <sup>+0.11</sup> <sub>-0.36</sub>	4.20 <sup>+0.03</sup> <sub>-0.03</sub>	56.72 <sup>+1.93</sup> <sub>-2.34</sub>	9.16 <sup>+2.69</sup> <sub>-2.27</sub>	34.91 <sup>+10.50</sup> <sub>-14.07</sub>
4U 1538-52	13 (ta)	3-50	1.45 <sup>+0.11</sup> <sub>-0.11</sub>	0.05 <sup>+0.01</sup> <sub>-0.01</sub>	(5.0 ± 0.3) × 10 <sup>-5</sup>	4.77 <sup>+0.05</sup> <sub>-0.05</sub>	17.98 <sup>+0.08</sup> <sub>-0.08</sub>	2.69 <sup>+0.12</sup> <sub>-0.11</sub>	3.02 <sup>+0.21</sup> <sub>-0.17</sub>
	13 (oe)	3-50	1.11 <sup>+0.11</sup> <sub>-0.11</sub>	0.07 <sup>+0.01</sup> <sub>-0.01</sub>	(1.01 ± 0.07) × 10 <sup>-4</sup>	4.81 <sup>+0.06</sup> <sub>-0.06</sub>	36.70 <sup>+0.42</sup> <sub>-0.37</sub>	3.28 <sup>+0.35</sup> <sub>-0.31</sub>	7.09 <sup>+0.93</sup> <sub>-0.83</sub>
Cep X-4	14	3-79	-	0.13 <sup>+0.05</sup> <sub>-0.01</sub>	0.36 <sup>+0.08</sup> <sub>-0.36</sub>	4.75 <sup>+0.05</sup> <sub>-0.06</sub>	22.25 <sup>+0.17</sup> <sub>-0.17</sub>	3.49 <sup>+0.18</sup> <sub>-0.17</sub>	6.37 <sup>+0.47</sup> <sub>-0.44</sub>
	15	3-79	-	1.96 <sup>+1.70</sup> <sub>-0.92</sub>	0.06 <sup>+0.13</sup> <sub>-0.03</sub>	(1.53 ± 0.09) × 10 <sup>-4</sup>	30.47 <sup>+0.14</sup> <sub>-0.14</sub>	5.17 <sup>+0.19</sup> <sub>-0.20</sub>	14.08 <sup>+0.80</sup> <sub>-0.71</sub>
4U 1626-67	16	3-79	0.93 <sup>+0.04</sup> <sub>-0.05</sub>	0.042 <sup>+0.003</sup> <sub>-0.003</sub>	-	23.99 <sup>+2.25</sup> <sub>-2.29</sub>	18.06 <sup>+0.79</sup> <sub>-0.67</sub>	2.36 <sup>+0.72</sup> <sub>-0.56</sub>	0.40 <sup>+0.26</sup> <sub>-0.17</sub>
SMC X-2	17	3-50	-	0.03 <sup>+0.38</sup> <sub>-0.01</sub>	0.31 <sup>+1.18</sup> <sub>-0.31</sub>	4.73 <sup>+0.29</sup> <sub>-0.14</sub>	29.35 <sup>+0.22</sup> <sub>-0.22</sub>	4.60 <sup>+0.26</sup> <sub>-0.26</sub>	12.95 <sup>+1.13</sup> <sub>-1.05</sub>
	18	3-50	0.67 <sup>+0.13</sup> <sub>-0.11</sub>	0.023 <sup>+0.006</sup> <sub>-0.004</sub>	(1.2 ± 0.1) × 10 <sup>-4</sup>	4.52 <sup>+0.26</sup> <sub>-0.17</sub>	37.30 <sup>+0.13</sup> <sub>-0.13</sub>	4.76 <sup>+0.19</sup> <sub>-0.17</sub>	17.28 <sup>+1.17</sup> <sub>-0.97</sub>
	19	3-50	0.96 <sup>+0.17</sup> <sub>-0.16</sub>	0.02 <sup>+0.01</sup> <sub>-0.01</sub>	(9.3 ± 0.8) × 10 <sup>-5</sup>	4.51 <sup>+0.10</sup> <sub>-0.10</sub>	26.94 <sup>+0.86</sup> <sub>-0.71</sub>	6.96 <sup>+1.32</sup> <sub>-1.39</sub>	5.39 <sup>+0.70</sup> <sub>-1.97</sub>
IGR J17544-2619	20	3-40	2.97 <sup>+0.37</sup> <sub>-0.34</sub>	0.09 <sup>+0.09</sup> <sub>-0.04</sub>	4.75 <sup>+0.73</sup> <sub>-0.61</sub>	4.77 <sup>+0.15</sup> <sub>-0.14</sub>	28.92 <sup>+2.43</sup> <sub>-1.68</sub>	7.20 <sup>+2.37</sup> <sub>-1.51</sub>	9.23 <sup>+0.22</sup> <sub>-0.45</sub>
IGR J16393-4643	21	3-50	1.19 <sup>+0.28</sup> <sub>-0.31</sub>	0.014 <sup>+0.010</sup> <sub>-0.007</sub>	(2.4 ± 0.4) × 10 <sup>-5</sup>	4.48 <sup>+0.13</sup> <sub>-0.14</sub>	30.75 <sup>+1.04</sup> <sub>-1.21</sub>	2.44 <sup>+0.98</sup> <sub>-1.00</sub>	1.87 <sup>+0.98</sup> <sub>-1.00</sub>
2S 1553-542	22	3-50	1.07 <sup>+0.07</sup> <sub>-0.14</sub>	0.07 <sup>+0.01</sup> <sub>-0.01</sub>	-	17.02 <sup>+6.62</sup> <sub>-5.85</sub>	27.13 <sup>+0.80</sup> <sub>-0.70</sub>	7.75 <sup>+1.28</sup> <sub>-1.16</sub>	14.92 <sup>+14.61</sup> <sub>-6.80</sub>
RX J0520.5-6932	23	4-55	0.42 <sup>+0.04</sup> <sub>-0.04</sub>	0.054 ± 0.003	-	7.35 <sup>+0.28</sup> <sub>-0.26</sub>	31.32 <sup>+0.79</sup> <sub>-0.70</sub>	5.53 <sup>+0.82</sup> <sub>-0.67</sub>	6.78 <sup>+1.84</sup> <sub>-1.38</sub>
	24	4-55	0.23 <sup>+0.03</sup> <sub>-0.03</sub>	0.036 ± 0.002	-	4.93 <sup>+0.10</sup> <sub>-0.10</sub>	31.92 <sup>+0.68</sup> <sub>-0.61</sub>	7.43 <sup>+0.76</sup> <sub>-0.63</sub>	13.45 <sup>+3.02</sup> <sub>-2.30</sub>
Cent X-3	25	3-60	1.27 <sup>+0.04</sup> <sub>-0.04</sub>	0.38 <sup>+0.03</sup> <sub>-0.03</sub>	-	12.48 <sup>+0.15</sup> <sub>-0.15</sub>	29.02 <sup>+0.68</sup> <sub>-0.39</sub>	4.93 <sup>+0.35</sup> <sub>-0.35</sub>	5.22 <sup>+0.66</sup> <sub>-0.66</sub>
GX 301-2	26	3-65	0.78 <sup>+0.21</sup> <sub>-0.03</sub>	0.09 <sup>+0.01</sup> <sub>-0.01</sub>	(6.7 ± 1.5) × 10 <sup>-5</sup>	6.59 <sup>+5.30</sup> <sub>-0.31</sub>	34.31 <sup>+1.04</sup> <sub>-1.04</sub>	4.51 <sup>+1.24</sup> <sub>-1.24</sub>	2.63 <sup>+2.68</sup> <sub>-1.43</sub>
	27 (ta)	3-65	0.85 <sup>+0.14</sup> <sub>-0.04</sub>	0.15 <sup>+0.01</sup> <sub>-0.01</sub>	1.05 <sup>+0.33</sup> <sub>-0.31</sub> × 10 <sup>-4</sup>	6.84 <sup>+4.09</sup> <sub>-0.63</sub>	51.22 <sup>+8.63</sup> <sub>-1.87</sub>	10.30 <sup>+9.07</sup> <sub>-2.54</sub>	25.95 <sup>+107.26</sup> <sub>-9.60</sub>
							33.88 <sup>+1.68</sup> <sub>-0.84</sub>	4.83 <sup>+1.52</sup> <sub>-1.31</sub>	2.77 <sup>+4.78</sup> <sub>-1.31</sub>
							53.21 <sup>+6.38</sup> <sub>-2.37</sub>	13.26 <sup>+143.92</sup> <sub>-27.02</sub>	54.60 <sup>+143.92</sup> <sub>-27.02</sub>



Table A1 – continued

Source	Observation details		Continuum parameters				$E_{\text{cut}}$ (keV)/ $KT_e^\dagger$ (keV)	$E_{\text{fold}}$ (keV)/ $\tau^\ddagger$	$E_{\text{cyc}}$ (keV)	CRSF $\sigma_{\text{cyc}}$ (keV)	Strength $^\S$
	Obs. Sn.	Energy range	$\Gamma_1$	norm. <sub>1</sub>	norm. <sub>2</sub> $\Gamma_0^\ddagger$ (keV)	$E_{\text{cut}}$ (keV)/ $KT_e^\dagger$ (keV)					
XTE J1829-098	27 (f)	3–65	$0.84^{+0.04}_{-0.05}$	$0.25^{+0.03}_{-0.02}$	$3.45^{+0.26}_{-0.33} \times 10^{-4}$	$5.66^{+0.15}_{-0.09}$	–	$32.64^{+1.26}_{-1.32}$	$4.04^{+0.81}_{-0.90}$	$1.82^{+1.00}_{-0.74}$	
	27 (q)	3–65	$0.89^{+0.04}_{-0.04}$	$0.13^{+0.01}_{-0.01}$	$(6.96 \pm 1.15) \times 10^{-5}$	$6.85^{+0.42}_{-0.31}$	–	$53.2^*$	$9.88^{+0.79}_{-0.84}$	$42.89^{+6.07}_{-4.54}$	
V 0332+53	28	3–40	$0.64^{+0.05}_{-0.05}$	$0.008^{+0.001}_{-0.001}$	–	$10.31^{+0.40}_{-0.47}$	$6.53^{+0.25}_{-0.28}$	$14.61^{+0.10}_{-0.09}$	$2.66^{+0.19}_{-0.20}$	$3.53^{+0.64}_{-0.57}$	
	29	3–55	$0.67^{+0.03}_{-0.03}$	$0.054 \pm 0.004$	–	$13.85^{+0.41}_{-0.45}$	$19.23^{+7.20}_{-3.73}$	$27.82^{+0.06}_{-0.07}$	$4.98^{+0.27}_{-0.24}$	$2.21^{+0.09}_{-0.08}$	
4U 1700–37	30	3–55	$0.75^{+0.03}_{-0.03}$	$0.030^{+0.003}_{-0.002}$	$15.50^{+0.38}_{-0.60}$	$16.22^{+2.87}_{-2.00}$	–	$27.89^{+0.07}_{-0.07}$	$7.49^{+1.85}_{-1.87}$	$10.47^{+1.94}_{-1.94}$	
	"	3–55	–	$0.031^{+0.080}_{-0.003}$	$0.45^{+0.19}_{-0.45}$	$5.87^{+0.35}_{-0.31}$	$18.68^{+0.78}_{-0.67}$	$27.67^{+0.08}_{-0.07}$	$7.2^*$	$12.56^{+1.88}_{-1.77}$	
LMC X-4	31	3–55	$0.71^{+0.04}_{-0.05}$	$0.015^{+0.002}_{-0.002}$	–	$16.49^{+0.35}_{-0.38}$	$17.85^{+3.92}_{-2.63}$	$29.43^{+0.09}_{-0.09}$	$4.04^{+0.28}_{-0.26}$	$2.32^{+0.09}_{-0.09}$	
	"	3–55	$0.37^{+0.23}_{-0.07}$	$0.020^{+0.006}_{-0.001}$	$(8.4 \pm 1.9) \times 10^{-5}$	$6.14^{+0.29}_{-0.33}$	–	$29.19^{+0.08}_{-0.08}$	$8.95^{+2.99}_{-2.69}$	$9.88^{+1.20}_{-2.09}$	
XTE J1858+034	32	3–55	$0.66^{+0.07}_{-0.14}$	$0.011^{+0.003}_{-0.003}$	–	$16.56^{+0.57}_{-1.30}$	$19.75^{+9.31}_{-4.10}$	$29.21^{+0.10}_{-0.11}$	$8.95^*$	$5.66^{+1.06}_{-1.06}$	
	33	5–55	$0.39^{+0.04}_{-0.05}$	$0.036^{+0.005}_{-0.004}$	$(1.2 \pm 0.2) \times 10^{-4}$	$5.48^{+0.27}_{-0.15}$	–	–	–	–	
4U 1700–37	34 (ta)	3–79	$0.82^{+0.06}_{-0.04}$	$0.10^{+0.01}_{-0.01}$	$(2.01 \pm 1.34) \times 10^{-6}$	$12.20^{+1.34}_{-0.96}$	–	–	–	–	
	34 (f)	3–79	$0.75^{+0.06}_{-0.06}$	$0.13^{+0.01}_{-0.01}$	$(3.79 \pm 2.05) \times 10^{-6}$	$11.68^{+1.22}_{-0.76}$	–	–	–	–	
LMC X-4	34 (q)	3–79	$1.23^{+0.08}_{-0.08}$	$0.07^{+0.01}_{-0.01}$	$6.93^{+4.07}_{-3.64} \times 10^{-7}$	$11.48^{+1.16}_{-1.06}$	–	–	–	–	
	35 (ta)	3–79	$0.60^{+0.08}_{-0.08}$	$0.05^{+0.01}_{-0.01}$	$(3.7 \pm 0.6) \times 10^{-5}$	$6.29^{+0.16}_{-0.14}$	–	–	–	–	
4U 1700–37	35 (f)	3–65	$0.78^{+0.14}_{-0.13}$	$0.18^{+0.08}_{-0.05}$	$(1.30 \pm 0.21) \times 10^{-4}$	$5.12^{+0.13}_{-0.12}$	–	–	–	–	
	35 (q)	3–79	$0.54^{+0.10}_{-0.11}$	$0.03^{+0.01}_{-0.01}$	$(3.6 \pm 0.6) \times 10^{-5}$	$6.33^{+0.17}_{-0.12}$	–	–	–	–	
XTE J1829-098	36	3–60	$0.89^{+0.06}_{-0.06}$	$0.030^{+0.004}_{-0.003}$	–	$17.70^{+3.38}_{-4.57}$	$10.10^{+0.42}_{-0.43}$	–	–	–	
	36	3–60	$0.72^{+0.09}_{-0.08}$	$0.020^{+0.004}_{-0.003}$	–	$20.18^{+2.08}_{-3.16}$	$9.96^{+0.33}_{-0.31}$	–	–	–	
4U 1700–37	37	3–68	$0.62^{+0.04}_{-0.05}$	$0.021^{+0.002}_{-0.002}$	–	$15.10^{+2.93}_{-3.73}$	$10.21^{+0.30}_{-0.32}$	–	–	–	
	37	3–68	$0.81^{+0.14}_{-0.18}$	$0.007^{+0.003}_{-0.003}$	–	$23.02^{+2.24}_{-2.66}$	$8.31^{+0.40}_{-0.38}$	–	–	–	
XTE J1829-098	38 (ta)	3–65	–	$0.004^{+0.006}_{-0.004}$	$0.37^{+0.86}_{-0.37}$	$5.77^{+0.09}_{-0.09}$	$24.78^{+3.58}_{-2.43}$	–	–	–	
	38 (f)	3–65	$0.77^{+0.08}_{-0.09}$	$0.05^{+0.01}_{-0.01}$	$(2.8 \pm 0.3) \times 10^{-5}$	$6.47^{+0.13}_{-0.12}$	–	–	–	–	
LMC X-4	38 (q)	3–65	$0.68^{+0.07}_{-0.07}$	$0.18^{+0.02}_{-0.02}$	$1.35^{+0.37}_{-0.33} \times 10^{-4}$	$4.92^{+0.20}_{-0.17}$	–	–	–	–	
	38 (q)	3–65	$1.34^{+0.20}_{-0.18}$	$0.18^{+0.08}_{-0.04}$	–	$17.01^{+3.45}_{-3.58}$	$7.76^{+0.48}_{-0.52}$	–	–	–	
XTE J1829-098	39	3–55	$0.51^{+0.10}_{-0.10}$	$0.017^{+0.003}_{-0.003}$	$(2.7 \pm 0.4) \times 10^{-5}$	$6.52^{+0.15}_{-0.13}$	–	–	–	–	
	39	3–55	$0.48^{+0.13}_{-0.12}$	$0.011^{+0.003}_{-0.003}$	$3.02^{+0.84}_{-3.00}$	$9.49^{+1.17}_{-1.29}$	–	$22.43^{+0.64}_{-0.58}$	$4.35^{+0.63}_{-0.53}$	$3.49^{+0.95}_{-0.69}$	
SMC X-1	40	3–79	$1.32^{+0.03}_{-0.03}$	$0.08^{+0.01}_{-0.01}$	–	$19.50^{+0.70}_{-0.60}$	$11.16^{+0.29}_{-0.28}$	–	–	–	
	41	3–79	$1.02^{+0.08}_{-0.08}$	$0.054^{+0.004}_{-0.005}$	–	$16.18^{+2.54}_{-2.50}$	$8.52^{+0.25}_{-0.26}$	–	–	–	
4U 1700–37	42	3–50	$1.22^{+0.23}_{-0.27}$	$0.01^{+0.01}_{-0.01}$	–	$19.79^{+1.98}_{-2.22}$	$5.80^{+0.42}_{-0.40}$	–	–	–	
	43	3–65	$0.35^{+0.01}_{-0.01}$	$0.064^{+0.001}_{-0.002}$	$(6.7 \pm 0.7) \times 10^{-5}$	$5.70^{+0.09}_{-0.08}$	–	–	–	–	
"	3–65	$1.01^{+0.07}_{-0.07}$	$0.09^{+0.01}_{-0.01}$	–	$13.88^{+2.39}_{-2.53}$	$8.90^{+0.21}_{-0.21}$	–	–	–		

**Table A1** – *continued*

Source	Observation details		Continuum parameters					CRSF $\sigma_{\text{cyc}}$ (keV)	Strength <sup>§</sup>	
	Obs. Sn.	Energy range	$\Gamma_1$	norm. <sub>1</sub>	norm. <sub>2</sub> $\Gamma_0^{\ddagger}$ (keV)	$E_{\text{cut}}$ (keV)/ $\Gamma_0^{\ddagger}$ (keV)	$E_{\text{fold}}$ (keV)/ $\tau^{\ddagger}$			$E_{\text{cyc}}$ (keV)
GRO J1008–57	44	3–79	NPEX	$0.46^{+0.03}_{-0.01}$	$(1.78 \pm 0.12) \times 10^{-4}$	$8.23^{+0.11}_{-0.09}$	–	78*	$9.10^{+1.68}_{-1.46}$	$12.61^{+3.02}_{-2.78}$
GX 304–1	45	3–25	PL	$1.75^{+0.20}_{-0.23}$	$(9.04 \pm 0.63) \times 10^{-4}$	–	–	–	–	–
1A 0535+26	46	3–79	FDC	$1.05^{+0.13}_{-0.01}$	$0.137^{+0.016}_{-0.004}$	–	$15.73^{+0.85}_{-0.91}$	$44.88^{+0.82}_{-0.75}$	$7.64^{+0.92}_{-0.67}$	$10.68^{+2.99}_{-1.65}$
	47	3–50	PL	$1.39^{+0.03}_{-0.04}$	$0.05^{+0.01}_{-0.01}$	–	–	–	–	–
	48	3–50	compTT + compTT	–	$(3.4 \pm 0.3) \times 10^{-4}$	$0.64^{+0.06}_{-0.06}$	$17.44^{+0.65}_{-1.20}$	$43.88^{+2.74}_{-3.49}$	7.67*	$27.95^{+5.93}_{-5.33}$
				$(2.0 \pm 0.5) \times 10^{-4}$	$0.64^{+0.06}_{-0.06}$	–	–	–	–	–
GRO J2058+42	49	3–79	CompTT	–	$0.041^{+0.132}_{-0.004}$	$0.40^{+0.12}_{-0.40}$	$11.12^{+0.30}_{-0.42}$	–	–	–
	50	3–79	CompTT	–	$0.043^{+0.014}_{-0.003}$	$0.41^{+0.07}_{-0.12}$	$7.99^{+0.08}_{-0.07}$	$12.83^{+0.39}_{-0.35}$	–	–
	51	3–79	NHC	$1.39^{+0.06}_{-0.07}$	$0.015^{+0.002}_{-0.002}$	–	$8.11^{+0.05}_{-0.05}$	$13.26^{+0.41}_{-0.33}$	–	–
IE 1145.1–6141	52	3–60	CPL	$0.88^{+0.06}_{-0.07}$	$0.018 \pm 0.002$	–	$14.41^{+1.28}_{-1.31}$	$27.54^{+2.85}_{-2.42}$	–	–
OAO 1657–415	53	5–70	CPL	$0.56^{+0.05}_{-0.05}$	$0.017^{+0.002}_{-0.002}$	–	–	$17.03^{+1.10}_{-0.96}$	–	–
EXO 2030+375	54	3–55	CPL	$1.20^{+0.02}_{-0.02}$	$1.11^{+0.04}_{-0.04}$	–	$18.93^{+0.25}_{-0.24}$	–	–	–
	55	3–60	NPEX	$1.02^{+0.04}_{-0.04}$	$0.018^{+0.002}_{-0.002}$	$(1.5 \pm 0.3) \times 10^{-6}$	$7.88^{+0.40}_{-0.34}$	–	–	–
	56	3–79	NPEX	$0.79^{+0.02}_{-0.03}$	$0.20^{+0.01}_{-0.01}$	$(7.5 \pm 2.1) \times 10^{-6}$	$10.80^{+0.53}_{-0.43}$	–	–	–
IGR J19294+1816	57	3–25	NPEX	$1.35^{+0.41}_{-0.34}$	$0.001^{+0.002}_{-0.001}$	–	$5.57^{+1.93}_{-0.85}$	–	–	–
	58	3–50	FDC	$1.14^{+0.03}_{-0.03}$	$(8.2 \pm 0.6) \times 10^{-3}$	–	$28.23^{+0.46}_{-0.49}$	$4.80^{+0.23}_{-0.23}$	–	–

Notes. <sup>†</sup> Normalization of cutoffpl model with power-law index -2 in NPEX continuum model.

<sup>‡</sup> Parameters for the CompTT continuum model.

<sup>§</sup> Optical depth is related to strength (line depth) by  $\tau_{\text{cyc}} = \frac{\text{Strength}_{\text{cyc}}}{\sqrt{2\pi\sigma_{\text{cyc}}}}$ .

\* Frozen parameter.

**Table A2.** The best-fitting parameters of the absorption ( $\tau_{\text{babs}}$ ,  $\tau_{\text{bpcf}}$ ), blackbody ( $\text{bbody}$ ), iron fluorescence lines (Gaussian), and  $\text{TKF}$  ( $\text{gabs}$ ) models, along with the fit statistic and AIC score used for model selection. Details of Obs. Sn.1 to 58 are given in this table.

Obs. Sn.	$\tau_{\text{babs}}$ $n_{\text{H1}}$	$f$	$\tau_{\text{bpcf}}$ $n_{\text{H2}}$	$kT_{\text{BB}}$	$\text{bbody}$ $\text{norm}_{\text{BB}}$	$E$ (Fe $K\alpha$ )	$\sigma$ (Fe $K\alpha$ )	Atomic line $\sigma$ (Fe $K\alpha$ )	nom.	$F_{\text{gabs}}$	$\sigma_{\text{gabs}}$	Strength $_{\text{gabs}}$	$C_{\text{FPMB}}$	Fit $\chi^2/\text{dof}$	AIC Score $\chi^2 + 2\ln \text{par}$
1 (ta)	0.015*	$0.45^{+0.03}_{-0.04}$	$44.45^{+5.84}_{-5.70}$	-	-	$6.41^{+0.02}_{-0.02}$	$0.15^{+0.04}_{-0.04}$	$(1 \pm 0.1) \times 10^{-3}$	-	-	-	-	$1.035 \pm 0.002$	$615.5/455$	655.5
1 (oe)	0.015*	-	-	-	-	$6.41^{+0.02}_{-0.02}$	$1.58^{+0.13}_{-0.14}$	$(6 \pm 0.1) \times 10^{-3}$	-	-	-	-	$1.033 \pm 0.003$	$500.9/433$	536.9
2	0.015*	$0.26^{+0.07}_{-0.09}$	$512.63^{+47.06}_{-63.56}$	$0.34^{+0.09}_{-0.08}$	$0.01^{+0.04}_{-0.01}$	$6.52^{+0.01}_{-0.01}$	$0.22^{+0.04}_{-0.05}$	$(3 \pm 1) \times 10^{-3}$	-	$11.05^{+0.23}_{-0.22}$	$0.88^{+0.22}_{-0.22}$	$0.05^{+0.03}_{-0.02}$	$1.033 \pm 0.001$	$538.3/474$	595.3
3	0.015*	$0.42^{+0.03}_{-0.03}$	$590.47^{+19.10}_{-18.52}$	$0.32^{+0.07}_{-0.05}$	$0.02^{+0.04}_{-0.01}$	$6.52^{+0.01}_{-0.01}$	$0.67^{+0.14}_{-0.14}$	$(4 \pm 0.8) \times 10^{-3}$	-	$10.21^{+0.12}_{-0.12}$	$0.23^{+0.13}_{-0.10}$	$0.012 \pm 0.004$	$1.016 \pm 0.001$	$696.9/488$	742.9
4	0.37*	$0.87^{+0.01}_{-0.01}$	$33.20^{+1.63}_{-1.40}$	-	-	$6.49^{+0.01}_{-0.01}$	$0.18^{+0.03}_{-0.03}$	$(3 \pm 0.6) \times 10^{-3}$	-	$10.39^{+0.24}_{-0.21}$	$1.34^{+0.36}_{-0.30}$	$0.10^{+0.04}_{-0.03}$	$1.044 \pm 0.002$	$552.4/23$	598.4
5	0.37*	$0.84^{+0.02}_{-0.02}$	$23.49^{+1.97}_{-2.06}$	-	-	$6.40^{+0.01}_{-0.01}$	$0.06^{+0.06}_{-0.06}$	$(4 \pm 0.3) \times 10^{-3}$	-	$10.39^{+0.24}_{-0.21}$	$1.34^{+0.36}_{-0.30}$	$0.10^{+0.04}_{-0.03}$	$1.027 \pm 0.004$	$531.9/435$	565.9
6	0.37*	$0.71^{+0.02}_{-0.02}$	$26.10^{+1.86}_{-1.96}$	-	-	$6.37^{+0.03}_{-0.03}$	$0.09^{+0.06}_{-0.09}$	$(1.3 \pm 0.2) \times 10^{-3}$	-	-	-	-	$1.013 \pm 0.002$	$503.9/465$	543.9
"	0.37*	$0.86^{+0.01}_{-0.01}$	$25.59^{+1.17}_{-0.63}$	-	-	$6.37^{+0.02}_{-0.02}$	$0.05^{+0.06}_{-0.05}$	$(7.6 \pm 0.8) \times 10^{-4}$	-	$11.97^{+0.32}_{-0.31}$	$1.96^{+0.39}_{-0.37}$	$0.20^{+0.10}_{-0.07}$	$1.013 \pm 0.002$	$540.9/463$	586.9
7 (f)	0.37*	$0.88^{+0.05}_{-0.05}$	$23.45^{+3.63}_{-4.53}$	-	-	$6.35^{+0.05}_{-0.06}$	$0.22^{+0.10}_{-0.08}$	$(2.7 \pm 0.8) \times 10^{-3}$	-	-	-	-	$1.02 \pm 0.01$	$454.1/398$	496.1
8	$0.10^{+0.21}_{-0.10}$	$0.21^{+0.04}_{-0.05}$	$79.11^{+21.83}_{-23.90}$	$2.09^{+0.10}_{-0.07}$	$(3.8 \pm 0.9) \times 10^{-3}$	$6.45^{+0.03}_{-0.03}$	$0.20^{+0.08}_{-0.08}$	$(5.2 \pm 0.1) \times 10^{-3}$	-	$10.25^{+0.26}_{-0.26}$	$1.11^{+0.40}_{-0.29}$	$0.07^{+0.05}_{-0.03}$	$0.998 \pm 0.002$	$506.8/23$	552.8
9	$1.50^{+2.65}_{-1.50}$	$0.15^{+0.03}_{-0.05}$	$463.43^{+83.43}_{-88.47}$	$0.59^{+0.17}_{-0.08}$	$(5.4^{+7.6}_{-2.7}) \times 10^{-3}$	$6.56^{+0.03}_{-0.03}$	$0.25^{+0.06}_{-0.06}$	$(1.5 \pm 0.3) \times 10^{-3}$	-	-	-	-	$1.017 \pm 0.002$	$546.8/486$	580.8
10	$3.39^{+1.40}_{-1.48}$	$0.26^{+0.02}_{-0.02}$	$511.99^{+52.01}_{-51.09}$	$0.53^{+0.05}_{-0.03}$	$0.02^{+0.01}_{-0.01}$	$6.51^{+0.03}_{-0.03}$	$0.23^{+0.05}_{-0.05}$	$(1.68 \pm 0.3) \times 10^{-3}$	-	-	-	-	$1.015 \pm 0.002$	$527.4/493$	559.4
11	$4.00^{+1.27}_{-1.38}$	$0.12^{+0.02}_{-0.05}$	$564.48^{+123.68}_{-110.40}$	$0.55^{+0.04}_{-0.05}$	$0.014 \pm 0.002$	$6.49^{+0.03}_{-0.03}$	$0.19^{+0.05}_{-0.05}$	$(9 \pm 1) \times 10^{-4}$	-	$7.96^{+0.12}_{-0.14}$	$1.44^{+0.21}_{-0.17}$	$0.40^{+0.11}_{-0.07}$	$1.021 \pm 0.002$	$583.8/503$	615.8
12	$6.27^{+0.49}_{-0.47}$	-	-	-	-	$6.38^{+0.03}_{-0.04}$	$0.22^{+0.06}_{-0.07}$	$(2.31^{+0.49}_{-0.44}) \times 10^{-4}$	-	-	-	-	$1.014 \pm 0.003$	$416.5/299$	456.5
13 (ta)	0.7*	$0.87^{+0.02}_{-0.02}$	$41.77^{+5.17}_{-5.17}$	-	-	$6.43^{+0.05}_{-0.05}$	$0.16^{+0.08}_{-0.08}$	$(2.0 \pm 0.4) \times 10^{-4}$	-	-	-	-	$1.02^{+0.01}_{-0.01}$	$363.0/306$	397.0
13 (oe)	0.7*	$0.86^{+0.03}_{-0.03}$	$29.75^{+4.80}_{-4.80}$	-	-	$6.42^{+0.07}_{-0.07}$	$0.08^{+0.15}_{-0.15}$	$(1.8 \pm 0.7) \times 10^{-4}$	-	-	-	-	$1.01^{+0.01}_{-0.01}$	$274.3/292$	308.3
14	$1.52^{+0.24}_{-0.24}$	$0.33^{+0.04}_{-0.02}$	$281.64^{+40.12}_{-30.67}$	-	-	$6.45^{+0.03}_{-0.03}$	$0.17^{+0.04}_{-0.04}$	$(8.1 \pm 1.3) \times 10^{-4}$	-	-	-	-	$1.034 \pm 0.002$	$530.7/458$	570.7
15	$0.10^{+0.25}_{-0.10}$	-	-	$1.41^{+0.08}_{-0.03}$	$(2.0 \pm 0.6) \times 10^{-3}$	$6.39^{+0.05}_{-0.05}$	$0.23^{+0.08}_{-0.08}$	$(1.9 \pm 0.5) \times 10^{-4}$	-	-	-	-	$1.021 \pm 0.004$	$440.8/421$	478.8
16	$0.05^{+0.41}_{-0.05}$	$0.32^{+0.05}_{-0.06}$	$620.03^{+70.62}_{-71.85}$	$0.49^{+0.03}_{-0.03}$	$(2.07 \pm 0.27) \times 10^{-3}$	$6.74^{+0.05}_{-0.05}$	$0.12^{+0.07}_{-0.08}$	$(1.6 \pm 0.5) \times 10^{-4}$	-	-	-	-	$1.002^{+0.003}_{-0.003}$	$691.4/444$	725.4
17	$0.65^{+0.96}_{-0.65}$	-	-	$2.19^{+0.55}_{-0.28}$	$(2.1 \pm 0.3) \times 10^{-3}$	$6.33^{+0.10}_{-0.11}$	$0.62^{+0.19}_{-0.15}$	$(6.8 \pm 2.0) \times 10^{-4}$	-	-	-	-	$1.014 \pm 0.004$	$304.5/317$	336.5
18	$0.85^{+0.97}_{-0.85}$	-	-	-	-	$6.30^{+0.08}_{-0.08}$	$0.34^{+0.11}_{-0.09}$	$(2.4 \pm 0.6) \times 10^{-4}$	-	-	-	-	$1.03^{+0.01}_{-0.01}$	$249.4/304$	277.4
19	$1.86^{+1.27}_{-1.25}$	-	-	-	-	$6.31^{+0.09}_{-0.10}$	$0.28^{+0.19}_{-0.15}$	$(11.6^{+5.2}_{-3.8}) \times 10^{-5}$	-	-	-	-	$1.03^{+0.01}_{-0.01}$	$324.3/300$	352.3
20	$16.36^{+3.95}_{-3.71}$	-	-	-	-	-	-	-	-	-	-	-	$1.09^{+0.03}_{-0.03}$	$236.1/200$	256.1
21	2.15*	$0.97^{+0.02}_{-0.02}$	$51.65^{+6.17}_{-6.29}$	-	-	-	-	-	-	$11.76^{+0.41}_{-0.45}$	$1.46^{+0.30}_{-0.47}$	$0.41^{+0.30}_{-0.16}$	$0.99^{+0.02}_{-0.02}$	$371.4/267$	405.4
22	$3.77^{+0.50}_{-0.84}$	$0.16^{+0.05}_{-0.05}$	$83.94^{+58.43}_{-58.63}$	-	-	$6.43^{+0.09}_{-0.09}$	$0.12^{+0.12}_{-0.12}$	$(1.4 \pm 0.7) \times 10^{-4}$	-	-	-	-	$1.012 \pm 0.003$	$268.6/314$	298.6
23	0.2*	$0.26^{+0.03}_{-0.03}$	$266.55^{+38.67}_{-62.83}$	-	-	$6.54^{+0.05}_{-0.05}$	$0.14^{+0.07}_{-0.08}$	$(3.7 \pm 0.9) \times 10^{-4}$	-	$9.87^{+0.39}_{-0.24}$	$0.39^{+0.58}_{-0.38}$	$0.03^{+0.04}_{-0.02}$	$1.043 \pm 0.004$	$332.8/312$	366.8
24	0.2*	-	-	-	-	$6.59^{+0.05}_{-0.05}$	$0.40^{+0.08}_{-0.08}$	$(23.3 \pm 0.1) \times 10^{-3}$	-	$11.69^{+0.27}_{-0.27}$	$0.37^{+0.39}_{-0.36}$	$0.02^{+0.02}_{-0.02}$	$1.022 \pm 0.003$	$381.8/339$	415.8
25	$5.27^{+0.58}_{-0.63}$	$0.52^{+0.02}_{-0.02}$	$72.38^{+5.75}_{-5.75}$	-	-	$6.36^{+0.02}_{-0.02}$	$0.10^{+0.04}_{-0.04}$	$(2.03 \pm 0.23) \times 10^{-3}$	-	$11.22^{+0.22}_{-0.23}$	$2.52^{+0.18}_{-0.16}$	$0.98^{+0.14}_{-0.16}$	$1.027 \pm 0.002$	$422.9/381$	464.9
26	$1.62^{+1.46}_{-1.46}$	$0.90^{+0.10}_{-0.10}$	$39.30^{+5.97}_{-5.97}$	-	-	$6.36^{+0.01}_{-0.01}$	$0.01^*$	$(10.0 \pm 0.6) \times 10^{-4}$	-	-	-	-	$1.054^{+0.004}_{-0.004}$	$479.5/387$	519.5
27 (ta)	$5.41^{+5.56}_{-5.41}$	$0.68^{+0.14}_{-0.14}$	$31.88^{+5.63}_{-5.63}$	-	-	$6.35^{+0.01}_{-0.01}$	$0.01^*$	$(1.76^{+0.26}_{-0.07}) \times 10^{-3}$	-	-	-	-	$1.065 \pm 0.003$	$486.8/395$	526.8
27 (f)	$0.10^{+0.10}_{-0.10}$	$0.82^{+0.01}_{-0.01}$	$31.62^{+2.16}_{-2.64}$	-	-	$6.35^{+0.02}_{-0.02}$	$0.01^*$	$(3.04 \pm 0.15) \times 10^{-4}$	-	-	-	-	$1.065 \pm 0.005$	$561.1/368$	601.1
27 (q)	$5.12 \pm 5.12$	$0.71^{+0.11}_{-0.18}$	$30.65^{+6.45}_{-2.79}$	-	-	$6.47^{+0.04}_{-0.04}$	$0.32^{+0.05}_{-0.04}$	$(1.27 \pm 0.07) \times 10^{-3}$	-	-	-	-	$1.067 \pm 0.004$	$363.9/378$	403.9
28	$3.58^{+0.73}_{-0.74}$	-	-	-	-	$6.36^{+0.01}_{-0.01}$	$0.01^*$	$(4.2 \pm 0.5) \times 10^{-4}$	-	-	-	-	$1.00^{+0.01}_{-0.01}$	$242.7/252$	268.7
29	$0.52^{+0.38}_{-0.39}$	$0.23^{+0.04}_{-0.03}$	$266.05^{+59.25}_{-63.26}$	-	-	$6.36^{+0.06}_{-0.06}$	$0.23^{+0.10}_{-0.09}$	$(6.2 \pm 2) \times 10^{-4}$	-	-	-	-	$1.015^{+0.003}_{-0.003}$	$420.4/340$	460.4
30	$0.89^{+0.43}_{-0.88}$	$0.12^{+0.03}_{-0.03}$	$189.37^{+152.24}_{-64.02}$	-	-	$6.30^{+0.05}_{-0.05}$	$0.01^*$	$(2.3 \pm 0.5) \times 10^{-4}$	-	-	-	-	$1.014^{+0.004}_{-0.004}$	$394.1/333$	430.1
"	$1.98^{+0.43}_{-0.43}$	-	-	-	-	$6.31^{+0.04}_{-0.04}$	$0.01^*$	$(2.1 \pm 0.4) \times 10^{-4}$	-	$9.73^{+0.28}_{-0.31}$	$2.14^{+0.51}_{-0.45}$	$0.33^{+0.22}_{-0.14}$	$1.014^{+0.004}_{-0.004}$	$416.4/331$	454.4
31	$5.30^{+2.21}_{-2.40}$	$0.23^{+0.06}_{-0.11}$	$158.95^{+40.23}_{-72.73}$	-	-	$6.28^{+0.07}_{-0.07}$	$0.01^*$	$(1.03 \pm 0.5) \times 10^{-4}$	-	-	-	-	$1.024^{+0.004}_{-0.004}$	$399.1/330$	433.1
"	$0.04^{+0.03}_{-0.02}$	-	-	-	-	$6.27^{+0.07}_{-0.07}$	$0.01^*$	$(9.37 \pm 3.7) \times 10^{-5}$	-	$11.52^{+0.35}_{-0.31}$	$0.59^{+0.43}_{-0.32}$	$0.04^{+0.03}_{-0.02}$	$1.024 \pm 0.004$	$434.5/328$	478.5
32	$3.35^{+3.12}_{-3.35}$	-	-	-	$5.1^{+5.4}_{-2.6} \times 10^{-4}$	$6.35^{+0.06}_{-0.07}$	$0.01^*$	$(9.6 \pm 2.7) \times 10^{-5}$	-	-	-	-	$1.04^{+0.01}_{-0.01}$	$370.4/325$	404.4

**Table A2** – *continued*

pt	tbabs nH <sub>1</sub>	tbpcf nH <sub>2</sub>	bbody kT <sub>BB</sub>	E (Fe K $\alpha$ )	Atomic line $\sigma$ (Fe K $\alpha$ )	$E_{\text{gabs}}$	$\sigma_{\text{gabs}}$	Strength <sub>gabs</sub>	C <sub>FWB</sub>	Fit $\chi^2/\text{dof}$	AIC Score $\chi^2 + 2\mu_{\text{par}}$
33	8.45 <sup>+2.43</sup> <sub>-2.46</sub>	–	–	6.48 <sup>+0.03</sup> <sub>-0.03</sub>	0.25 <sup>+0.06</sup> <sub>-0.06</sub>	–	–	–	1.017 <sup>+0.003</sup> <sub>-0.003</sub>	412.4/337	440.4
34 (ta)	0.5*	30.22 <sup>+1.53</sup> <sub>-1.55</sub>	–	6.56 <sup>+0.01</sup> <sub>-0.01</sub>	0.01*	10.61 <sup>+0.50</sup> <sub>-0.42</sub>	1.66 <sup>+0.77</sup> <sub>-0.65</sub>	0.10 <sup>+0.18</sup> <sub>-0.06</sub>	1.013 <sup>+0.003</sup> <sub>-0.003</sub>	481.1/467	521.1
34 (f)	0.5*	30.02 <sup>+1.64</sup> <sub>-1.63</sub>	–	6.56 <sup>+0.01</sup> <sub>-0.01</sub>	0.01*	10.54 <sup>+0.54</sup> <sub>-0.59</sub>	1.83 <sup>+0.79</sup> <sub>-0.58</sub>	0.11 <sup>+0.13</sup> <sub>-0.06</sub>	0.928 <sup>+0.002</sup> <sub>-0.002</sub>	511.6/465	551.6
34 (q)	0.5*	33.06 <sup>+3.23</sup> <sub>-3.23</sub>	–	6.52 <sup>+0.04</sup> <sub>-0.04</sub>	0.01*	11.39 <sup>+0.60</sup> <sub>-0.64</sub>	1.25 <sup>+0.69</sup> <sub>-0.51</sub>	0.15 <sup>+0.15</sup> <sub>-0.07</sub>	0.97 <sup>+0.01</sup> <sub>-0.01</sub>	434.7/388	474.7
35 (ta)	0.08*	89.37 <sup>+21.24</sup> <sub>-21.24</sub>	–	6.57 <sup>+0.05</sup> <sub>-0.06</sub>	0.32 <sup>+0.11</sup> <sub>-0.10</sub>	10.70 <sup>+0.30</sup> <sub>-0.31</sub>	2.21 <sup>+0.49</sup> <sub>-0.49</sub>	0.56 <sup>+0.35</sup> <sub>-0.20</sub>	1.021 <sup>+0.004</sup> <sub>-0.004</sub>	473.4/417	507.4
35 (f)	0.08*	52.02 <sup>+17.46</sup> <sub>-16.48</sub>	–	6.59 <sup>+0.13</sup> <sub>-0.10</sub>	0.46 <sup>+0.21</sup> <sub>-0.14</sub>	10.57 <sup>+0.33</sup> <sub>-0.33</sub>	1.56 <sup>+0.45</sup> <sub>-0.47</sub>	0.29 <sup>+0.21</sup> <sub>-0.15</sub>	1.07 <sup>+0.01</sup> <sub>-0.01</sub>	452.0/340	486.0
35 (q)	0.08*	89.46 <sup>+32.62</sup> <sub>-24.08</sub>	–	6.53 <sup>+0.06</sup> <sub>-0.07</sub>	0.25 <sup>+0.12</sup> <sub>-0.16</sub>	11.14 <sup>+0.53</sup> <sub>-0.58</sub>	2.03 <sup>+0.47</sup> <sub>-0.69</sub>	0.34 <sup>+0.34</sup> <sub>-0.18</sub>	1.00 <sup>+0.01</sup> <sub>-0.01</sub>	460.9/403	494.9
36	0.08*	414.45 <sup>+66.53</sup> <sub>-72.49</sub>	–	6.48 <sup>+0.05</sup> <sub>-0.05</sub>	0.41 <sup>+0.07</sup> <sub>-0.06</sub>	–	–	–	1.00 <sup>+0.01</sup> <sub>-0.01</sub>	479.0/406	503.0
"	0.08*	123.07 <sup>+123.56</sup> <sub>-27.86</sub>	–	6.48 <sup>+0.07</sup> <sub>-0.07</sub>	0.25 <sup>+0.13</sup> <sub>-0.14</sub>	10.88 <sup>+0.49</sup> <sub>-0.43</sub>	1.71 <sup>+0.46</sup> <sub>-0.57</sub>	0.22 <sup>+0.10</sup> <sub>-0.14</sub>	1.03 <sup>+0.01</sup> <sub>-0.01</sub>	404.9/362	434.9
"	0.08*	334.87 <sup>+51.17</sup> <sub>-54.41</sub>	–	6.51 <sup>+0.06</sup> <sub>-0.06</sub>	0.34 <sup>+0.09</sup> <sub>-0.07</sub>	–	–	–	1.03 <sup>+0.01</sup> <sub>-0.01</sub>	415.5/365	439.5
37	0.08*	89.01 <sup>+42.02</sup> <sub>-19.13</sub>	–	6.34 <sup>+0.07</sup> <sub>-0.06</sub>	0.16 <sup>+0.14</sup> <sub>-0.16</sub>	10.42 <sup>+0.59</sup> <sub>-0.70</sub>	1.89 <sup>+0.73</sup> <sub>-0.51</sub>	0.37 <sup>+0.27</sup> <sub>-0.16</sub>	1.02 <sup>+0.01</sup> <sub>-0.01</sub>	442.3/354	472.3
"	0.08*	–	(1.8 ± 0.8) × 10 <sup>-4</sup>	6.35 <sup>+0.06</sup> <sub>-0.06</sub>	0.45 <sup>+0.10</sup> <sub>-0.09</sub>	–	–	–	1.02 <sup>+0.01</sup> <sub>-0.01</sub>	446.8/357	472.8
38 (ta)	0.08*	87.59 <sup>+24.22</sup> <sub>-16.32</sub>	–	6.50 <sup>+0.09</sup> <sub>-0.10</sub>	0.21 <sup>+0.19</sup> <sub>-0.21</sub>	10.45 <sup>+0.24</sup> <sub>-0.26</sub>	1.60 <sup>+0.28</sup> <sub>-0.25</sub>	0.40 <sup>+0.12</sup> <sub>-0.10</sub>	1.02 <sup>+0.01</sup> <sub>-0.01</sub>	394.2/368	428.2
38 (f)	0.08*	–	0.003 ± 0.002	6.40 <sup>+0.14</sup> <sub>-0.13</sub>	0.71 <sup>+0.17</sup> <sub>-0.18</sub>	10.28 <sup>+0.36</sup> <sub>-0.33</sub>	1.35 <sup>+0.62</sup> <sub>-0.52</sub>	0.29 <sup>+0.25</sup> <sub>-0.17</sub>	1.02 <sup>+0.01</sup> <sub>-0.01</sub>	321.9/322	349.9
"	0.08*	–	–	6.42 <sup>+0.12</sup> <sub>-0.22</sub>	0.89 <sup>+0.26</sup> <sub>-0.17</sub>	–	–	–	1.02 <sup>+0.01</sup> <sub>-0.01</sub>	336.2/323	358.2
38 (q)	0.08*	124.03 <sup>+48.95</sup> <sub>-34.64</sub>	–	6.33 <sup>+0.06</sup> <sub>-0.06</sub>	0.01*	10.96 <sup>+0.47</sup> <sub>-0.52</sub>	1.12 <sup>+0.55</sup> <sub>-0.34</sub>	0.14 <sup>+0.08</sup> <sub>-0.05</sub>	1.03 <sup>+0.01</sup> <sub>-0.01</sub>	410.0/363	444.0
39	0.3*	56.43 <sup>+4.06</sup> <sub>-4.07</sub>	–	6.32 <sup>+0.05</sup> <sub>-0.05</sub>	0.01*	–	–	–	1.01 <sup>+0.01</sup> <sub>-0.01</sub>	372.2/318	406.2
40	0.5*	–	(4.2 ± 0.2) × 10 <sup>-3</sup>	6.39 <sup>+0.07</sup> <sub>-0.08</sub>	0.42 <sup>+0.14</sup> <sub>-0.11</sub>	–	–	–	1.021 ± 0.004	486.2/416	514.2
41	0.5*	–	0.001 <sup>+0.003</sup> <sub>-0.002</sub>	6.30 <sup>+0.07</sup> <sub>-0.07</sub>	0.45 <sup>+0.12</sup> <sub>-0.10</sub>	–	–	–	1.038 <sup>+0.004</sup> <sub>-0.004</sub>	479.2/408	501.2
42	0.5*	66.80 <sup>+8.98</sup> <sub>-10.34</sub>	–	6.34 <sup>+0.04</sup> <sub>-0.05</sub>	0.20 <sup>+0.10</sup> <sub>-0.10</sub>	–	–	–	1.02 <sup>+0.01</sup> <sub>-0.01</sub>	334.1/260	358.1
43	0.5*	–	–	6.39 <sup>+0.07</sup> <sub>-0.08</sub>	0.51 <sup>+0.14</sup> <sub>-0.15</sub>	10.87 <sup>+0.61</sup> <sub>-0.46</sub>	0.92 <sup>+0.87</sup> <sub>-0.35</sub>	0.04 <sup>+0.06</sup> <sub>-0.03</sub>	1.027 <sup>+0.004</sup> <sub>-0.003</sub>	387.6/378	415.6
"	0.5*	–	(2.23 ± 0.37) × 10 <sup>-3</sup>	6.38 <sup>+0.09</sup> <sub>-0.10</sub>	0.57 <sup>+0.19</sup> <sub>-0.18</sub>	–	–	–	1.027 ± 0.004	396.7/379	418.7
44	0.10 <sup>+0.21</sup> <sub>-0.10</sub>	101.65 <sup>+16.04</sup> <sub>-10.70</sub>	–	6.48 <sup>+0.02</sup> <sub>-0.02</sub>	0.14 <sup>+0.03</sup> <sub>-0.04</sub>	–	–	–	1.024 ± 0.001	579.4/510	619.4
45	0.10 <sup>+0.26</sup> <sub>-0.10</sub>	–	(9.23 ± 1.01) × 10 <sup>-5</sup>	6.48 <sup>+0.02</sup> <sub>-0.02</sub>	1.95 <sup>+0.10</sup> <sub>-0.09</sub>	–	–	–	0.99 <sup>+0.02</sup> <sub>-0.02</sub>	1057.3/1019	1069.3
46	0.10 <sup>+0.71</sup> <sub>-0.10</sub>	–	(1.2 ± 0.5) × 10 <sup>-3</sup>	6.37 <sup>+0.05</sup> <sub>-0.05</sub>	0.14 <sup>+0.07</sup> <sub>-0.08</sub>	–	–	–	0.971 <sup>+0.003</sup> <sub>-0.003</sub>	506.2/468	534.2
47	0.81 <sup>+0.50</sup> <sub>-0.49</sub>	–	(1.1 ± 0.1) × 10 <sup>-3</sup>	6.30 <sup>+0.18</sup> <sub>-0.15</sub>	0.17 <sup>+0.23</sup> <sub>-0.17</sub>	–	–	–	0.985 ± 0.004	345.5/331	369.5
48	0.4*	–	–	–	–	–	–	–	0.96 ± 0.01	313.0/278	NA
49	0.60*	86.70 <sup>+32.55</sup> <sub>-28.47</sub>	0.005 ± 0.001	6.39 <sup>+0.06</sup> <sub>-0.05</sub>	0.11 <sup>+0.12</sup> <sub>-0.11</sub>	10.87 <sup>+0.23</sup> <sub>-0.24</sub>	1.46 <sup>+0.37</sup> <sub>-0.36</sub>	0.20 <sup>+0.10</sup> <sub>-0.06</sub>	0.986 ± 0.003	557.8/468	595.8
50	0.60*	73.59 <sup>+24.44</sup> <sub>-25.57</sub>	0.006 ± 0.001	6.39 <sup>+0.04</sup> <sub>-0.04</sub>	0.24 <sup>+0.12</sup> <sub>-0.09</sub>	10.90 <sup>+0.21</sup> <sub>-0.22</sub>	1.71 <sup>+0.32</sup> <sub>-0.28</sub>	0.22 <sup>+0.08</sup> <sub>-0.07</sub>	0.997 ± 0.002	592.3/500	630.2
51	0.60*	–	(5.1 ± 0.5) × 10 <sup>-4</sup>	6.09 <sup>+0.32</sup> <sub>-0.31</sub>	0.49 <sup>+0.44</sup> <sub>-0.44</sub>	–	–	–	0.97 <sup>+0.01</sup> <sub>-0.01</sub>	417.8/411	441.8
52	4.51 <sup>+0.63</sup> <sub>-0.64</sub>	–	(6.1 ± 0.7) × 10 <sup>-4</sup>	6.34 <sup>+0.04</sup> <sub>-0.04</sub>	0.26 <sup>+0.06</sup> <sub>-0.06</sub>	–	–	–	0.993 <sup>+0.004</sup> <sub>-0.004</sub>	369.3/372	389.3
53	1.81*	60.99 <sup>+5.20</sup> <sub>-5.41</sub>	–	6.33 <sup>+0.01</sup> <sub>-0.01</sub>	0.01*	–	–	–	0.977 ± 0.003	559.8/424	587.8
54	0.8*	85.04 <sup>+6.29</sup> <sub>-5.02</sub>	–	6.51 <sup>+0.01</sup> <sub>-0.01</sub>	0.24 <sup>+0.02</sup> <sub>-0.02</sub>	10.86 <sup>+0.12</sup> <sub>-0.12</sub>	2.06 <sup>+0.16</sup> <sub>-0.15</sub>	0.25 <sup>+0.03</sup> <sub>-0.03</sub>	0.984 <sup>+0.001</sup> <sub>-0.001</sub>	623.1/421	651.1
55	0.8*	11.32 <sup>+7.13</sup> <sub>-7.02</sub>	–	6.35 <sup>+0.13</sup> <sub>-0.13</sub>	0.01*	–	–	–	1.01 <sup>+0.01</sup> <sub>-0.01</sub>	358.5/344	386.5
56	0.8*	59.13 <sup>+19.99</sup> <sub>-13.50</sub>	0.004 ± 0.001	6.43 <sup>+0.03</sup> <sub>-0.03</sub>	0.20 <sup>+0.05</sup> <sub>-0.05</sub>	10.57 <sup>+0.28</sup> <sub>-0.28</sub>	0.99 <sup>+0.38</sup> <sub>-0.24</sub>	0.06 <sup>+0.03</sup> <sub>-0.02</sub>	1.031 ± 0.002	535.9/483	573.9
57	12.08 <sup>+6.11</sup> <sub>-5.61</sub>	–	–	–	–	–	–	–	1.10 <sup>+0.06</sup> <sub>-0.06</sub>	107.8/128	123.8
58	6.09 <sup>+0.77</sup> <sub>-0.77</sub>	–	–	6.45 <sup>+0.07</sup> <sub>-0.07</sub>	0.18 <sup>+0.13</sup> <sub>-0.18</sub>	–	–	–	1.02 <sup>+0.01</sup> <sub>-0.01</sub>	303.4/296	321.4

Note. \* Frozen parameter.

This paper has been typeset from a  $\text{\LaTeX}$  file prepared by the author.